UCLA

UCLA Electronic Theses and Dissertations

Title

Rheology of biological macromolecules

Permalink

https://escholarship.org/uc/item/5tg6x3z6

Author

Ariyaratne, Amila Dinesh

Publication Date

2015

Peer reviewed|Thesis/dissertation

eScholarship.org Powered by the California Digital Library
University of California

University of California
Los Angeles

Rheology of biological macromolecules

A dissertation submitted in partial satisfaction
of the requirements for the degree
Doctor of Philosophy in Physics and Astronomy

by

Amila Dinesh Ariyaratne

2015

© Copyright by
Amila Dinesh Ariyaratne
2015

Abstract of the Dissertation

Rheology of biological macromolecules

by

Amila Dinesh Ariyaratne

Doctor of Philosophy in Physics and Astronomy

University of California, Los Angeles, 2015

Professor Giovanni Zocchi, Chair

Proteins have interesting mechanical properties in addition to the remarkable functionality. For example, Guanylate kinase is an enzyme that catalyzes Guanosine monophosphate (GMP) to Guanosine diphosphate (GDP) conversion and this enzyme is approximately 5 nm in size. A gold nano particle of similar size shows linear elasticity for strains up to $\sim 0.1\%$ and shows plastic deformation beyond that, whereas the enzyme Guanylate kinase can have strains up to 1 % with reversible deformation. Our experiments show many different regimes of the mechanical response before the plastic deformation of these proteins. In this dissertation, I study the materials properties of two classes of proteins, an ion channel protein and a transferase, which is a globular protein. The experimental techniques to study the materials properties of these proteins were uniquely developed at the Zocchi lab. Therefore, we were able to observe previously unknown characteristics of these folded proteins.

The mechanical properties of the voltage gated potassium channel KvAP was studied by applying AC depolarizing voltages. This technique gave new information about the system that was not seen in the previous studies. These previous experiments were based on applying DC depolarizing voltage steps across the membrane to study the ionic current. By monitoring the ionic current at different depolarizing voltage steps, the DC gating process of the channel could be understood. We probed the channel using AC depolarizing signals instead of DC pulses and the ionic current revealed new behaviors, which cannot be predicted with the DC response. We found that the conformational motion of the voltage-sensing domain of the ion channel shows internal dissipation. Further, a new non linearity in the dissipation parameter was found in which the dissipation parameter increased with the shear rate of the applied force.

Previous studies at the Zocchi lab used a nano rheology experiment on the protein Guanylate kinase to study the mechanical properties of a globular protein. The protein was subjected to a mechanical force and the deformation was measured with sub-Angstrom resolution. We found that the protein shows a linear elasticity regime for low forcing and viscoelastic behavior for high forcing. The internal viscosity of the protein is due to the internal dissipation of the protein. This dissertation takes the work on nano rheology of proteins further by studying the temperature effect on the materials properties of the protein and the contribution of the surface of the protein to the observed mechanics.

In addition to studying the materials properties of proteins, we used proteins to design new biomimetic systems. The first system covered in this dissertation is the development of a novel sensor platform for molecules. In this sensor, we detect the change in the stiffness of the substrate upon binding a target rather than the usual scheme of detecting the change in mass upon binding of a target. By combining the nano rheology setup with localized surface plasmon resonance, this sensor platform yields a very robust signal. The other biomimetic system that is discussed here is an artificial axon is constructed with ion channels and lipid bilayers.

The dissertation of Amila Dinesh Ariyaratne is approved.

Peter Narins

Dolores Bozovic

Giovanni Zocchi, Committee Chair

University of California, Los Angeles
2015

To my wife and parents

Table of Contents

1 Introduction **1**

1.1 Biomolecules as nano machines 1

1.2 Measuring of mechanical properties of proteins 2

1.2.1 Existing techniques and limitations 2

1.2.2 A rheology experiment on proteins 6

1.3 Bio-inspired systems 7

2 Rheology of ion channels **9**

2.1 Introduction 9

2.2 Structure of KvAP 10

2.3 The selectivity filter of a Kv channel 12

2.4 Voltage sensor domain of KvAP 12

2.5 Inactivation of Kv channels 14

2.6 Preparation of KvAP proteoliposomes 15

2.6.1 Expression of KvAP 15

2.6.2 Purification of KvAP 20

2.6.3 Protein purification protocol 21

2.6.4 Reconstitution of KvAP channels in lipid vesicles 25

2.7 Electrophysiology setup to measure ion channel currents 28

2.8 Response of the KvAP ion channel for DC pulses 30

2.9 Experimental setup for probing voltage gated ion channels with AC voltages 35

2.10 The response of KvAP to oscillatory voltages 40

2.10.1 Variation of the ion channel current at different membrane voltages 44
2.10.2 Frequency response of the ion channel at different membrane potentials 47
2.11 Continuum mechanics model of the ion channel KvAP 47

3 Mechanical properties of globular proteins measured via nano rheology 58

3.1 Theoretical basis of the nano rheology experiment 58
3.1.1 Evanescent wave scattering from gold nano particles 58
3.1.2 The force on gold nano particles in the experimental setup 63
3.2 Sample preparation 65
3.2.1 Preparation of the protein sample 66
3.2.2 Preparation of gold-coated glass slides 69
3.2.3 Coupling enzymes to the gold coated slide 70
3.2.4 Coupling gold nano particles to the enzyme 70
3.2.5 Functionalizing the gold nano particles with DNA 71
3.2.6 Preparation of the sample chamber 72
3.3 The experimental nano rheology setup and method 72
3.4 Mechanical response of the enzyme Guanylate Kinase 76
3.4.1 Interpretation of the results 77
3.4.2 Maxwell model of solids 79
3.5 Effect of temperature on the mechanics of the protein 81
3.5.1 Temperature control for the nano rheology setup 82

3.5.2 Effect of temperature on the materials properties of Guanylate kinase 86
3.6 Influence of the hydration shell on the mechanics of the protein . 95
3.6.1 Hydration shell of a protein 96

4 Biosensor based on nano rheology 107
4.1 Current SPR based biomolecule detection scheme 108
4.1.1 What are Surface plasmons? 108
4.1.2 Surface plasmon resonance 112
4.1.3 Detection of biomolecules with SPR 116
4.2 Combining SPR and nano rheology 118
4.2.1 Improved signal from LSPR in the nano rheology setup . . 118
4.2.2 Detection of small molecules binding to GK 122
4.2.3 Comparison with a fluorescence based detection scheme . . 124
4.3 Future work 132

5 An artificial axon 134
5.1 Basics of neural signal propagation 134
5.1.1 The Nernst potential 135
5.1.2 Propagating signals in the axon 136
5.2 Experimental approach for the artificial axon 140
5.2.1 Single well system to control Nernst potential 140
5.2.2 The two-well system 148
5.3 Micro-machined approach 148

5.3.1 Fabricating the thin silicon nitride membrane with micron scale apertures 151
5.3.2 Fabrication of electrodes 155
5.3.3 Making PDMS support layers 158
5.3.4 Bonding the device 164
5.3.5 Future work 166

References **167**

List of Figures

1.1 Using an optical tweezers to force proteins. The laser beam is brought to a fine focus and a dielectric sphere is trapped in the beam. The biomolecule is tethered to a fixed surface from one end and tethered to the dielectric sphere from the other end. The laser beam is displaced to deform the protein. 4

2.1 Top view of the crystal structure of KvAP. The image was generated from the crystal structure with PDB ID 1ORQ. The image shows that the channel is a tetramer. In addition, a K^+ ion can be seen in the central conduction pore. 10

2.2 Structure of a KvAP monomer. The cartoon representation shows the arrangement of helices in the functional channel. The voltage-sensing domain contains the helices S1 to S4. S4 is a positively charged helix due to the presence of Arginine residues. S5 and S6 form the pore domain. On the right is a crystal structure of a monomer from PDB ID 2R9R where the same color code as in the cartoon representation on the left is used. 11

2.3 The selectivity filter of the ion channel KcSA [20]. There are four binding sites for the potassium ions inside the filter and ions move in a single file motion. 13

2.4 The selectivity filter of a Kv channel upon inactivation. Structure of the selectivity filter in (a) high K^+ and (b) low K^+ environments. The blue dots represent K^+ ions in the crystal structure. Under low salt conditions, the filter is collapsed blocking the movement of ions. Adapted from Andrew Wong thesis (Manipulation of Molecular Processes with DNA Molecular Springs), structure generated from PDB ID 1K4C and 1K4D. 15

2.5 Flow chart of KvAP expression and purification. 17

2.6 Sequence of the wild type KvAP cloned in PQE60 vector. The thrombin cleavage site was added to remove the His-tag after the protein purification process. 18

2.7 Protein purification with Cobalt beads. The His-tagged protein forms a complex with the metal ions Co or Ni. The metal ion is grafted on a agarose bead with a Nitrilotriacetic acid (NTA) resin. A competing agent such as Imidazole can disrupt the His-tag metal ion complex at high enough concentrations. 22

2.8 Electrophysiology setup to measure ion channel currents. Ion channels are incorporated to a lipid bilayer spanned across a $\sim 100\ \mu$m aperture fabricated in a plastic cup. The plastic cup is inserted to the Teflon buffer chamber. A head stage amplifier is used to clamp the voltage and measure the ionic current. A data acquisition system (DAQ) records the output from the head stage amplifier. The command voltage pulse for the experiment is given by the DAQ which is controlled by custom software. 29

2.9 Setup for the formation of a lipid bilayer separating two fluid compartments. The Teflon cup holder chamber (same as Teflon buffer chamber in Fig. 2.8) has a glass slide at the bottom. The setup is mounted on an inverted microscope to observe the lipid bilayer. The bilayer is painted across the aperture with a glass spatula. . 30

2.10 Current from a single KvAP channel. The channels were kept in the closed state for an extended period before stepping the voltage to 60 mV to record the current trace. Even though the membrane potential is 60 mV throughout the interval of the trace, the channel opens only during a fraction of the time. The current due to a single channel at 60 mV is 10 pA. 31

2.11 Multi channel current trace. The current trace corresponds to about 50 KvAP channels. The channels were kept in the closed state for an extended period of time before stepping the voltage to 60 mV (stepped at 0.25 s). The initial spike is a capacitive transient. The channels open stochastically with a time scale of $\sim$ 30 ms and decay exponentially due to inactivation. 32

2.12 Multi channel current trace after correcting for the inactivation. This graph was obtained by using the data in Fig. 2.11. An exponential decay was fitted to the current trace after the peak to determine the inactivation time scale. This inactivation time scale was used to multiply the current trace with an exponential factor to correct for the inactivation. 33

2.13 The DC voltage pulse protocol used to measure the opening probability. The membrane potential is held at -120 mV for 10.8 seconds to recover channels from inactivation. Then the voltage is stepped to the desired value and sustained for 1.2 seconds. 34

2.14 The experimentally measured opening probability curve for KvAP. Each point was obtained by averaging 20 data points and all data was from channels in the same bilayer. For voltages close to $\sim$ -40 mV, the channels are almost closed and for voltages above $\sim$ 20 mV, the channels are fully open. The fit is produced from equation 2.3. 34

2.15 A two state system to model the voltage gated ion channel KvAP. The closed state has a higher energy since the channels are mostly open even with no voltage difference. E_0 is the energy difference between the two states without any voltage difference and α is a parameter. 35

2.16 The equivalent circuit of a lipid bilayer with ion channels. The bilayer acts as a capacitor while the channels are equivalent to resistors (with a time and voltage dependent resistance). 36

2.17 Electronic scheme to subtract the capacitive current from the bilayer. The command voltage is applied to the actual lipid bilayer used in the experiment. At the same time, the same command voltage is applied to a variable capacitor. Two identical I to V converters convert the resulting currents to voltage levels and a pre amplifier subtracts the voltage signal of the variable capacitor from the lipid bilayer. By matching the variable capacitor to that of the lipid bilayer, the capacitive portion can be subtracted effectively. 37

2.18 Ion channel current before performing the capacitive current cancellation procedure. The initial part of the trace is a mix of the capacitive current and the ion channel current. Ion channels inactivate towards the end of the trace ($\sim$ 0.2 s), showing only the capacitive current. 38

2.19 Ion channel current after performing the capacitive current cancellation procedure. As shown in Fig. 2.18, only the capacitive current of the bilayer results after channel inactivation. The variable capacitor is tuned to cancel the capacitive current from the lipid bilayer. The fact that the signal falls to zero implies that the capacitive portion of the current has been nulled by this technique. 39

2.20 Pulse protocol to probe the AC behavior of KvAP. 40

2.21 Ion channel current at a relatively low frequency of 5 Hz. The ionic current across the channels is plotted along with the applied sinusoidal voltage. An asymmetry between the positive and negative voltage peaks can be observed. This asymmetry is a consequence of the open probability curve. 41

2.22 Ion channel current at an intermediate frequency of 20 Hz. At this intermediate frequency, the positive and negative peaks are still asymmetric as a consequence of the open probability curve. . . . 41

2.23 Ion channel current at a relatively high frequency of 100 Hz. The envelop of the AC current trace is modulated by the DC current trace. A new feature at this relatively high frequency is the symmetry in the positive and negative current peaks. 42

2.24 Calculated ion channel current for an applied voltage at 5 Hz based on the open probability curve. The current was calculated as $I(t) = N \cdot \chi \cdot P(V(t)) \cdot V(t) \cdot exp(-t/\tau)$ with $V(t) = V_0 \sin(\omega t)$. 43

2.25 Calculated ion channel current for an applied voltage at 50 Hz based on the open probability curve. 44

2.26 The variation of the positive and negative peak currents vs. the applied AC voltage at 5 Hz. The asymmetry of the two branches is due to the opening probability curve. 45

2.27 The variation of the positive and negative peak currents vs. the applied voltage when the AC voltage is at 40 Hz. At this intermediate frequency, the positive and negative branches appear to be symmetric implying that the channels are only exploring a small region of the opening probability curve. 46

2.28 The variation of the positive and negative peak currents vs. the applied voltage when the AC voltage is at 100 Hz. A new feature is seen where the ionic current saturates and then decreases for increasing applied voltage. 47

2.29 The variation of the positive peak current with frequency at fixed amplitude of the applied voltage. Frequency response of the ion channel is different between the two voltages studied. 48

2.30 Cartoon representation of the continuum mechanical model of the ion channel KvAP to model the AC response. The voltage sensing S4 helix is assumed to move as if it is connected to a damped spring. 49

2.31 Output current of the model at a relatively low frequency of 5 Hz. The same qualitative features can be seen as in the experimental low frequency trace in Fig. 2.21. 53

2.32 Algorithm to extract the value of γ from a graph of I_{peak} vs. applied voltage. 54

2.33 Variation of the dissipation parameter γ with the shear rate. The dissipative parameter remained constant below a critical shear rate but increased linearly above this critical shear rate. 56

3.1 Evanescent wave in the buffer solution. A laser beam hits the glass-water interface at an angle θ which is higher than the critical angle θ_c for the interface. The evanescent wave in the side of water travels parallel to the interface. 60

3.2 Scattering of the evanescent wave from gold nano particles. ϵ_0 is the polarization of the incident beam travelling along the $\vec{n_0}$ direction which polarizes the gold nano particle. We are interested in calculating the radiation scattered in the direction given by vector $\vec{n}$. 62

3.3 The Helmholtz model of an electric double layer. The surface charge of the metal is neutralized with counter ions in the solution, a distance d away from the surface. 64

3.4 The Gouy diffuse layer model of an electric double layer. The ions in the solution obey a Boltzmann distribution. Electric field decreases exponentially from the metal surface within ∼1 nm. 66

3.5 Gold nano particles tethered to the substrate via the enzyme Guanylate kinase. The scale bar is 500 nm. 71

3.6 Construction of the parallel plate capacitor fluid chamber. The plastic spacer strips were glued to the slides using the epoxy Loctite 608^{TM}. 72

3.7 An image of a fluid chamber used in the nano rheology experiment. The red rectangle marked on the base glass slide is the hydrophobic barrier that holds the buffer in. The two slides combined have a transparency of about 8%. 73

3.8 Experimental setup to perform nano rheology on proteins. The fluid chamber is optically coupled to a prism with index-matched oil and a 488 nm laser is steered through the prism to produce an evanescent wave inside the fluid chamber. The fluid chamber is driven with the reference output voltage of the Lock-in amplifier. Scattered light from the GNPs is detected with a photo multiplier tube. 75

3.9 Frequency response of Guanylate kinase measured at a fixed amplitude of forcing of 125 mV. Apart from the small fluctuation, the value essentially remains fixed around 0.6 Å regardless of the frequency of the force. 76

3.10 Frequency response of Guanylate kinase measured at a fixed amplitude of forcing of 250 mV. At this relatively high applied forcing, the response is qualitatively different from the response in Fig. 3.9. The response diverges as $1/\omega$ towards the low frequency end, while the response flattens at the high frequency limit. 77

3.11 Maxwell model of a solid. The Maxwell model consists of an elastic spring in series with a dissipative dashpot. The total strain of the system is the addition of strain of each element. 79

3.12 Variation of the corner frequency ω_c with the forcing amplitude. A monotonic increase of the corner frequency can be seen. The response is elastic above the corner frequency and viscoelastic (dissipative) below the corner frequency. 81

3.13 Setup to control temperature of the nano rheology experiment. A metallic enclosure was built to cover the fluid chamber and the prism. Copper water blocks were attached to the metal box to regulate the temperature of the enclosure. The readout from a thermocouple attached to the fluid chamber was used as the working temperature. 83

3.14 Reversibility of the Mechanical response of GK at 35 °C. The response was recorded initially at 22 °C (blue data points) and the temperature was raised to 35 °C to obtain the response shown in the red data points. The temperature of the fluid chamber was lowered back to 22 °C to record the data in green points. The overlapping of blue and green data points implies that the mechanics of the protein was altered reversibly. The fits were produced by using equation 3.36. 84

3.15 Reversibility of the Mechanical response of GK at 12 °C. Initially, the response was recorded at 22 °C (shown in red points). The temperature was lowered to 12 °C to record the response shown in blue points. Raising the temperature back to 22 °C (green points) can reproduce the initial behavior. The fits were produced by using equation 3.36. 85

3.16 Mechanical response of GK at elevated temperatures. The response at different temperatures was recorded from the same sample and each point corresponds to the average of 5 recordings. A clear increase in the deformation amplitude can be seen as the temperature is elevated. The fits were produced using equation 3.36. 87

3.17 Mechanical response of GK at 12 °C. Reducing the temperature lowers the deformation amplitude for the same amplitude of forcing. The fits were produced using equation 3.36. 88

3.18 Irreversible denaturation of the protein at 55 °C. The response of the protein is feature less at the elevated temperature. Lowering the temperature back to 22 °C cannot reproduce the initial behavior. The fit for 22 °C data was produced using equation 3.36 90

3.19 Irreversible denaturation of the protein at 2 °C. The response at 2 °C is essentially feature less. The amplitude is much smaller than at 22 °C and raising the temperature back to 22 °C cannot reproduce the initial response. The fit for data at 22 °C was produced using equation 3.36. 92

3.20 Thermodynamic stability of the protein versus temperature. The y-axis is the free energy difference between the unfolded state and the folded state (ΔG). At room temperature, the free energy of the unfolded state is a maximum, implying that the folded state is stable. As the temperature approaches 2 °C or 55 °C, the stability of the folded state decreases. 93

3.21 Variation of k and γ with temperature. The plot is the relative change of the mechanical parameters with respect to that of room temperature. The values for k and γ were obtained by the fits in Figs. 3.16 and 3.17. 94

3.22 Arrhenius plot of log (ω_c) versus 1/T. The coner frequency ω_c was determined from the fits in Figs. 3.16 and 3.17. 95

3.23 Cartoon representation of the hydration shell of a protein. A 2−3 water molecule layer forms the hydration shell. The molecules in the hydration shell are in an ordered state compared with the bulk water with slow dynamics. 97

3.24 Structure of the molecule DMSO. The molecule has a trigonal pyramidal structure, with a central sulfur atom. DMSO has non polar characteristics due to the presence of the methyl groups and polar characteristics due to the highly polarized S−O bond. 97

3.25 Cartoon representation of the hydration shell of a protein with DMSO. DMSO can aggregate at the hydration shell of the protein, modifying the hydration shell. 99

3.26 Gold nano particle tethered by a single stranded DNA molecule. DNA Arm B was attached to the gold coated slide via a thiol modification. DNA Arm A was conjugated with gold nano particles separately [54]. DNA Arm A and Arm B were designed such that they have a complementary region of 12 base pairs at their ends. Thus, addition of DNA modified gold nano particles on the DNA Arm B modified slide tethers the gold nano particles on the slide. 100

3.27 Frequency response of a single stranded DNA molecule with and without DMSO. The data for the response curve was obtained with the geometry shown in Fig. 3.26. Single stranded DNA behaves as a random coil, which is an entropic spring. The fact that the response amplitude does not change with DMSO implies that the relation between the voltage applied across the fluid cell and the actual force on the gold nano particle does not change with DMSO. 101

3.28 Effect of 1% DMSO on the mechanics of the protein. Data shows the response amplitude vs. forcing frequency in the absence (squares) and presence (circles) of 1% DMSO, for the same sample. Lines are fits with the viscoelastic response 3.36. Each point is the average of 4−5 measurements and the standard deviation is usually 0.1 Å. 102

3.29 The change in mechanical response due to DMSO is reversible. The figure shows, for the same sample, the response amplitude vs. frequency before adding DMSO (squares), after adding 0.5 % DMSO (circles), and after removing DMSO (triangles). Each point is an average of 4-5 measurements and the standard deviation is ∼ 0.1 Å. Lines are fits with the viscoelastic response 3.36 103

3.30 Variation of γ (the dissipation parameter of the viscoelastic description) with DMSO concentration. Percent change in the viscoelastic dissipation parameter (measured from fitting to equation 3.36) vs. DMSO concentration. The curve is a fit produced with equation 3.37, giving the values $K_D = 0.17$ % and $\alpha = 62$ %. Each point is calculated by averaging 5 measurements and the error bars indicate uncertainty ($\sigma/\sqrt{N}$). The dissipation increases by 60 % in the presence of DMSO. 104

3.31 Variation of k with DMSO concentration. Given the large error bars, it is not clear whether k is unaffected or increases slightly with DMSO. Each point is calculated by averaging 5 measurements and the error bars indicate uncertainty ($\sigma/\sqrt{N}$). 106

4.1 The experimental setup. The enzyme is covalently coupled to the 30 nm Au layer on one side, and a 20 nm gold nano particle (GNP) on the opposite side. The negatively charged GNPs are driven by an oscillating electric field in a parallel plate capacitor arrangement in buffered saline sodium citrate (SSC). The amplitude of oscillation of the GNPs is measured by SPR enhanced scattering with phase - locked detection. There are $\sim 10^8$ GNPs in the field of view of the 60 X objective; the scattered intensity represents the ensemble averaged position of the GNPs. 109

4.2 The interface between an Au surface and a dielectric (water). The propagating EM wave is shown in both media, where the magnetic field is directed out of the plane of the image. 110

4.3 The distribution of the electric field about the interface. The field decays exponentially in either side of the boundary, the decay length in to gold being shorter than towards the dielectric side. 113

4.4 Surface plasmon resonance by prism coupled configuration. A laser beam is incident at an angle θ which is higher than the critical angle θ_c. The evanescent wave travels parallel to the gold surface with a wave vector dependent among many other things, the incident angle. At a certain incident angle, the wave vector of the evanescent wave and the surface plasmon wave vector match, giving rise to SPR. 114

4.5 Variation of the scattered light intensity (SPR mode) with the direction of polarization of the incident laser beam with respect to the gold surface. As the polarization of the incident beam approaches 90° (s-polarized: electric field parallel to the gold surface), the intensity of the scattered beam vanishes. In the measurements, zero angle (p-polarized) was offset by about 15°. The line is a fit to a cosine function. 115

4.6 Variation of the reflected intensity with the incident angle. Near complete reflection occurs when the incident angle is above the critical angle. But, as the incident angle is increased further, a sharp resonant dip occurs due to the absorbance of the excitation beam (to excite surface plasmons). The angle at which the dip occurs change with the effective refractive index of the medium above the gold layer. 117

4.7 Output voltage from the PMT detector with excitation from a He-Ne laser at 632 nm (SPR mode). The dashed line shows the voltage applied across the sample chamber. This electric field drives the negatively charged GNPs into a collective oscillation that modulates the amount of light scattered depending on the distance of the GNPs from the surface. The solid line shows the light detected by the PMT. 120

4.8 Output voltage from the PMT detector with excitation from a 488 nm laser (EWS mode). The dashed line shows the voltage applied across the sample chamber while the solid line shows the light detected by the PMT. 120

4.9 Mechanical response of the enzyme GK for an applied oscillatory force, measured in SPR and EWS modes. Plotted is the amplitude of oscillation δI of the light intensity radiated by the GNPs (normalized by the total light intensity I), which is proportional to the amplitude of the collective oscillation of the GNPs. The frequency dependence of this mechanical susceptibility is characteristic of viscoelasticity [36, 37]. For the same sample, we show measurements obtained in SPR mode (squares; $\lambda = 632\,nm$) and EWS mode (circles; $\lambda = 488\,nm$). The triangles are the same data as the circles, multiplied by the factor $\chi = 6$, showing that SPR mode has a 6× larger dynamic range compared to EWS mode. The amplitude of the applied voltage (proportional to the applied force [36]) is $175\,mV$ for sample (a) and $250\,mV$ for sample (b); the factor $\chi = 6$ is the same in both cases. 121

4.10 Binding isotherms measured by SPR enhanced nano-rheology. The signal is the amplitude of oscillation of the light intensity plotted vs. ligand concentration for a fixed forcing frequency (12 Hz). The lines are fits using the equation 4.20. (a) Binding of the substrate GMP is detected through the stiffening of the enzyme, with a dynamic range of the signal of $\sim 15\%$. The fit gives $K_d = 4.7\mu M$ for the dissociation constant. (b) CMP (not a substrate) also binds at sufficiently high concentration ($K_d \approx 2.4mM$). (c) Binding of the substrate ATP ($K_d = 1.2mM$) leads to a softening of the enzyme, in contrast to (a). 125

4.11 Titration curve for sucrose binding to Guanylate Kinase, using SPR enhanced mechanical detection. The signal is constant within experimental error up to sucrose concentrations $\sim$ 10 mM, i.e. no signature of binding is detected in this concentration range, as expected. 126

4.12 Spectroscopic detection of GMP binding to Guanylate Kinase in solution using tryptophan fluorescence. The initial increase in fluorescence is the signature of binding. The drop in fluorescence intensity beyond 10 μM GMP is due to the absorption of the UV excitation light by GMP. 127

4.13 Fluorescence measurements for ATP binding to GK. Measurements were performed in SSC/3 with 5 mM Mg^{+2} added (same buffer conditions as for the nano-rheology measurements). The decrease in the signal beyond 100 μM ATP concentration is due to the absorption of the excitation light by ATP. 127

4.14 Absorbance of 280 nm light by GMP. In the geometry of the spectrometer, the absorbance becomes significant beyond GMP concentrations of 10 μM (the absorbance scale is logarithmic). The red line is a linear regression between concentration and absorbance. 130

4.15 Absorbance of 280 nm light by ATP. The absorbance is prominent beyond $\sim$ 100 μM ATP concentration. 130

4.16 Fluorescence measurements of GMP binding to GK (same data as Fig. 4.12), corrected for absorbance of the excitation light, using the measurements of Fig. 4.14 as explained in the text. The line is a fit to the single site binding isotherm giving the value $K_d \approx 5.1\,\mu$M for the dissociation constant. 131

4.17 Fluorescence signature of ATP binding to GK (same data as Fig. 4.13), corrected for ATP absorbance using the measurements of Fig. 4.15. The line is a fit to the binding isotherm and returns the value $K_d \approx 1.6$ mM, in good agreement with the value from the nano-rheology method (1.2 mM). 131

4.18 Titration curve of CMP binding to GK. The large decrease in fluorescence is due to the absorption of UV light by CMP making it difficult to extract information about binding of CMP to GK from these fluorescence measurements. 132

5.1 A simplified axon model. The figure shows the extracellular medium and the intracellular medium separated by the lipid bilayer (containing ion channels). The equivalent electrical circuit is shown on the same diagram. c_m is the capacitance of the lipid bilayer per unit area, r_{ch} is the resistance of the ion channels per unit area and V_N is the Nernst potential across the membrane. The real axon can be considered a hollow tube, thus the area of the dx element is $dx \cdot 2\pi a$ where a is the radius of the axon. 137

5.2 The one well system to study Nernst potential. The head stage amplifier is connected to the Ag/AgCl electrode via a solid-state relay S_1. This relay is driven by the driver IC A1 (BSP 75N) and analog output channel 2 (AO 2) of the DAQ controls the relay. The voltage in the top chamber is recorded with a separate Ag/AgCl electrode using a high input impedance amplifier. The amplifier is constructed with the op-amp A2 (AD795) in the non-inverting configuration. R_1 and R_2 were set at 10 KΩ and 100 KΩ to have a gain of 11. The data acquisition system (DAQ) was connected to the computer (PC) and runs custom software to control the solid-state relays and record signals. 142

5.3 The voltage measured in the buffer using an independent electrode under voltage clamping conditions. The blue curve is the experimentally measured voltage with the high input impedance voltage amplifier shown in Fig. 5.2 while the grey curve is proportional to the current delivered to the system with the head stage amplifier. Initially the voltage is clamped at -120 mV where the channels are mostly closed. Stepping the potential to 60 mV at ~ 1.5 s opens the channels stochastically which is seen in the current trace. . . 143

5.4 The voltage measured in the buffer upon releasing the voltage clamp. The measurement was taken with the setup shown in Fig. 5.2. Initially, the membrane voltage is clamped at -120 mV and the clamping is released at 0 s. After that, the membrane voltage rises rapidly to the Nernst potential of the system (~ 35 mV). . . 144

5.5 The voltage measured in the buffer upon releasing the voltage clamp when there are no channels in the lipid bilayer. The blue curve is the experimentally measured voltage in the upper chamber using the high impedance voltage amplifier and the grey curve is the output from the head stage amplifier (proportional to the current delivered to the top chamber by the head stage amplifier). The membrane potential is initially held at the holding voltage of -120 mV and stepped to 60 mV for 1.2 s. During this time, there is almost no current (except for a capacitive transient and a very small leakage current). This shows us that there are no channels in the bilayer. At around 5.25 s, the clamping electrode is released. The membrane potential rises by a small amount and decays back to -120 mV exponentially. This is in contrast to the behavior in Fig. 5.4. 145

5.6 One-well system to study the Nernst potential with an added impedance. A capacitive load, C_m, corresponds to the lipid bilayer of the 2^{nd} well and R_A is the access resistance for the electrodes in the 2^{nd} well. S_2 is a solid-state relay to enable measurements with and without the load from the same system. The load capacitor C_m = 60 pF and R_A = 10 KΩ. R_2 and R_1 were set at 100 KΩ and 10 KΩ to have a gain of 11. 146

5.7 Influence of an external RC load to the Nernst potential spike. These curves were generated with the setup shown in Fig. 5.6 where a capacitive load was connected to represent the effect of a cascaded 2^{nd} well. The voltage clamp was released at around 0.5 s and this results in the membrane potential spiking to the Nernst potential of the system ($\sim$ 40 mV). The effect of the load is to delay the rise time of the potential. 147

5.8 A two-well system to demonstrate the propagation of the Nernst potential spike. S_1 and S_2 are two solid state relays controlled by software. They are used to float the voltage clamping when required. A is a high-impedance voltage amplifier built with an operational amplifier. S_3 is a solid-state relay to isolate well 1 and 2 initially. c_{in} represents the capacitance of the axon between the two wells and R_{in} is the resistance of the intracellular medium between the two wells. The head stage amplifiers are used initially to verify the presence of ion channels in each well. Once channels have been incorporated successfully in each well, S_2 is left open and S_3 is closed. A pulse is initiated by releasing S_1 momentarily. . . 149

5.9 Schematic diagram of the micro-machined system to realize a synthetic axon. Two fluid compartments (fluid channels) are separated by a thin silicon nitride membrane. The top channel corresponds to the interior of the axon. The thin membrane has small apertures to support a lipid bilayer. Ion channels are incorporated in these lipid bilayers to establish the Nernst potential and propagate signals. Fluid channels are fabricated with the elastomer Polydimethy siloxane and the silicon nitride membrane is fabricated on a silicon chip. 150

5.10 Process flow to fabricate a free standing silicon nitride membrane. (a) Ultra clean Si wafers must be used with no organic contaminants. Piranha clean can be utilized to remove organics from the wafer. (b) Silicon nitride is deposited on both sides of the wafer using a plasma enhanced chemical vapor deposition system. The film is about 400 nm thick and the residual stress must be a minimum to fabricate freestanding membranes. (c) E-beam deposition of Au. An adhesion layer of 20 nm Cr followed by 50 nm Au was applied. (d) Pattern the Au layer to expose the underlying silicon nitride layer. (e) Deposit Au on the other side of the wafer as a protectant (f) Etch the silicon nitride layer using Reaction Ion Etching to expose the bare Si wafer. (g) Etch the Si wafer anisotropically using hot KOH till a freestanding silicon nitride membrane is obtained. (h) Remove the protective Au and Cr layers with corresponding chemical etchants. 152

5.11 Etching of silicon nitride with Reactive Ion Etching (RIE). The patterned wafer on the left shows the appearance after removing the gold selectively. This is the process shown in Fig. 5.10 (d) The exposed silicon nitride is green in color. The wafer on the right shows a similar wafer to that on left, but after etching the silicon nitride layer with RIE. This exposes the underlying silicon wafer (similar to the process shown in Fig. 5.10 (f)) 153

5.12 Silicon chip containing the free standing membrane. The green area is the silicon nitride layer on the Si wafer while the square in the center is the freestanding silicon nitride membrane. The membrane is about 90 μm × 90 μm and 400 nm thick. Image was acquired with a microscope using the light reflected off the surface. 154

5.13 Silicon chip containing the free standing membrane with a ~ 25 μm aperture. The aperture was fabricated with photolithographic patterning followed by reactive ion etching. 155

5.14 A free standing silicon nitride membrane with an array of 10 μm holes. Separation between the holes is 10 μm. The image was acquired with an SEM by focusing the e-beam on the top surface of a chip. 156

5.15 Back side of a silicon chip containing the free standing membrane. The small square pits correspond to the locations where the KOH etched the Si wafer till it met the silicon nitride membrane on the other side of the wafer. 157

5.16 The liftoff process for the fabrication of electrodes on the silicon nitride membrane. This process is done after fabricating freestanding silicon nitride membrane with the apertures. (a) The silicon chip with the silicon nitride membrane is coated with a thin layer of photoresist AZ5214 IR. (b) An aligner is used to position the electrode pattern at the appropriate position relative to the apertures and the photoresist is patterned according to manufacturers guidelines (c) Metal deposition using an e-beam evaporator (d) a brief acetone dip dissolves the photoresist leaving only the metal directly deposited on the silicon chip. 159

5.17 Image of an electrode fabricated adjacent to a free standing silicon nitride membrane with an aperture. The gold pad connects the Ag electrode to the outside instrumentation. The gold pas was fabricated first using the liftoff technique described here. 20 nm of Cr followed by 50 nm of Au was deposited to produce the gold pad. A separate liftoff process was performed to fabricate the Ag electrode on the gold pad. The thickness of the silver electrode is 500 nm. 160

5.18 Silicon chips patterned with electrodes. A free standing membrane with an aperture exists next to each end of an electrode as shown in Fig. 5.17. The multi electrode Si chip on the right can also be used to record the voltage along the channel. 161

5.19 Fabrication of the PDMS fluid channels. (a) The initial step is to produce the mold on a Si wafer. The Si wafer must undergo a passivation with Sigmacote before applying PDMS. (b) The mold was fixed to the bottom of a petri dish and PDMS solution was poured on to the mold. PDMS was baked in a 65 °C oven after degassing to remove air bubbles. (c) Peel off the PDMS layer from the wafer. 162

5.20 An image of a PDMS mold created by pattering photoresist on a silicon wafer. The mold shown in the image corresponds to the bottom PDMS layer. 100 μm thick SU-8 2100 photoresist was used for patterning the mold. 163

5.21 The top PDMS layer with the fluid channels. The arrows indicate the intended direction of flow of buffer. The channel is 10 μm deep and the two circular inlet ports on the right side was designed to aid in pumping two different fluids. 164

5.22 PDMS microfluidic layer bonded on to a glass slide. This device was fabricated for testing the fluid flow in a 10 μm deep fluid channels. The tube pumps colored water from the left inlet and the solution comes out from the other side. 165

5.23 An assembled axon device. The image shows a multi well axon device where a 60 μm aperture is present next to each electrode. A straight fluid channel of 10 μm height and 100 μm wide runs across the apertures from the topside and a 100 μm deep channel runs underneath the apertures. 165

List of Tables

2.1 Preparation of KvAP protein purification buffers. 23

3.1 Preparation of Guanylate kinase purification buffers. 68

ACKNOWLEDGMENTS

This dissertation could not have been written without the support of many people through the past five years at UCLA. First of all, my deepest gratitude goes to my graduate advisor, Giovanni Zocchi. He is a great scientist, mentor, and friend in many ways. He is always around when I need to talk about research or life, always granted me plenty of freedom to explore and develop my research and guided me through many obstacles with his brilliant experimental intuition and passion. I am grateful for having the opportunity to work under such a good advisor.

I thank my colleagues, Yong Wang, Hao Qu, Chioa-Yu Tseng, Zahra Alavi and Hector Garcia for being my faithful companions and partners in the daily life in the lab.

I would also like to send my greatest appreciation to Andrew Wang. The initial lessons that I learned from him when I joined the lab are priceless. In addition to the experimental knowledge on the expression and reconstitution of ion channel proteins, he advised me on many issues relating to life at the lab.

The many teachers in UCLA, Dolores Bozovic, Robijn Bruinsma, Alex Levine, taught me from fundamental graduate school physics to the ongoing research in biophysics. I am honored to have the opportunities to learn from them.

I would like to thank the staff in the Department for helping me process orders, Sherin Samaan and Nancy Madrid; handle experimental materials and equipment, Ernesto Najar; work in the machine shop, Harry Lockart; maintain laboratory facilities, Craig Reaves; and for supporting in every aspects of my graduate life, Elaine Dolalas, Cecile Chang, Marisela Diaz-Vasquez, and Jenny Lee.

My deepest gratitude is given to my family: my father A.R. Ariyaratne and my mother Mal Devi Dassanayake for making me what I am now, showing me how to be a great scientist, and offering me their endless love and trust; my dearest wife Dilhara Ranasinghe for being the best friend of my life, sharing so many important moments with me, and always bringing me happiness and peacefulness in my hard times. I feel so fortunate for having them involved in my life.

VITA

2005–2009	B. Sc. (Physics), University of Peradeniya, Sri Lanka.
2009–2015	Ph. D. candidate (Physics), University of California Los Angeles.
2009–2015	Teaching Assistant, Department of Physics and Astronomy, UCLA. Taught sections of Astronomy 3 Lab, 6B and 6C labs and 4BL Lab.

PUBLICATIONS

Determination of Magnetic Properties of Cobalt Films Using Second Order Perturbed Heisenberg Hamiltonian. P. Samarasekara and **A. Ariyaratne**, STM journals: Journal of Physics, volume 1, issue 1, April 2012.

Nonlinearity of a voltage gated potassium channel revealed by the mechanical susceptibility. **A. Ariyaratne** and G. Zocchi, Phys. Rev. X 3, 011010 (2013).

Dissipative Dynamics of Enzymes. **A. Ariyaratne**, Chenhao Wu, Chiao-Yu Tseng and G. Zocchi, Phys. Rev. Lett. 113, 198101 (2014).

Plasmon resonance enhanced mechanical detection of ligand binding. **A. Ariyaratne** and G. Zocchi, Appl. Phys. Lett. 106, 013702 (2015).

Artificial phosphorylation sites modulate the activity of a voltage gated potassium channel. **A. Ariyaratne** and G. Zocchi, Phys. Rev. E, 91, 032701 (2015).

Nano-rheology measurements reveal that the hydration layer of enzymes partially controls conformational dynamics. Zahra Alavi, **A. Ariyaratne** and G. Zocchi, accepted for publication in Applied Physics Letters (2015).

CHAPTER 1

Introduction

1.1 Biomolecules as nano machines

Biomolecules such as proteins are remarkable machines at the nano scale. There are many proteins that undergo a large conformational change in order to perform crucial tasks to sustain life. For example, the protein ATP synthase is important in providing energy for a cell by converting ADP to ATP using an electrochemical gradient. This enzyme uses the electrochemical gradient of H^+ ions across a membrane to drive a rotary shaft. The motion of this rotary shaft is coupled to the binding site of ADP and a phosphate group such that the rotary movement brings ADP and the phosphate group close to each other in the right conformation to transfer the phosphate group to the ADP [1]. Another remarkable protein that undergoes a large deformations to perform its task is the kinesin motor proteins [2]. This motor protein is responsible for transporting cargo along microtubules. The two head groups of this molecule must undergo a large conformational change in order to walk along the microtubule by consuming ATP.

These mechanical motions of proteins are ubiquitous in living systems, even in a process like signal propagation in a neuron. The gradient of K, Na ions in a neuron is maintained by nano pumps (Na^+/K^+-ATPase) and the action potential is initiated from opening and closing of ion channel gates. Proteins can deform reversibly, sometimes as high as 5 % of their size, while their linear elasticity regime extends to around 1% strain. In contrast, the linear elasticity regime of a crystal is around 0.1 %.

1.2 Measuring of mechanical properties of proteins

In a physics point of view, it is interesting to study the materials properties of proteins. One of the main goals of this thesis is to characterize the materials properties of proteins and to study how they are influenced by external perturbations. There are many techniques to study the materials properties of proteins. These techniques include AFM, neutron scattering, optical tweezers etc. However, in my thesis, I present techniques that are uniquely developed at our laboratory to study proteins and these have many advantages over the well-established techniques.

1.2.1 Existing techniques and limitations

Neutron and X-ray scattering

X-ray crystallography is a widely used technique, mostly by biochemists, to elucidate the structures of proteins (or other biomolecules like DNA, vitamin etc.). The first X-ray crystallographic structure of a protein was of myoglobin by Max Perutz and John Kendrew, who won the Nobel Chemistry Prize in 1962. Ever since, there have been more than 70000 biomolecule crystal structures solved. Important information of the properties of proteins can be learned with X-ray crystallography. The main advantage is that it is possible to create a map of the spatial arrangement of the atoms from X-ray crystallography, and this gives the structure of the protein at the Angstrom level. This technique has been perfected for a long time so there are many robust tools and software to aid the process [3]. The disadvantage of this technique is the fact that the protein must be crystallized, and most of the time, the native protein by itself does not crystallize. In addition, the structure and properties of the crystallized structure can differ from the physiologically relevant form.

Neutron scattering is another useful technique for studying protein structures in crystallized form. This technique is similar to X-ray crystallography to a certain degree. In X-ray crystallography, the photons are scattered from the electron cloud of an atom while in neutron scattering, the neutrons interact with the nucleus of an atom.

In addition to the spatial information about the distribution of atoms, these techniques can provide information about the thermal motion of atoms that can be interpreted as a structural property such as flexibility. The Debye-Waller factor is such a parameter that measures the flexibility of atoms in a protein via X-ray crystallography or via neutron scattering. The intensity of Bragg scattering decreases due to the thermal motion of atoms about their equilibrium positions and this is given by the Debye-Waller factor. The elastic modulus k is given by $k \sim k_B T / < \Delta r >^2$ where k_B is the Boltzmann factor, T is the temperature and $< \Delta r >$ is the thermal fluctuations. However, if the protein has different response regimes beyond the linear elasticity, they cannot be seen with neutron scattering or x-ray diffraction experiments.

Atomic Force Microscopy (AFM)

Even though the AFM was initially used in material research, the work from many research groups led to the current biocompatible AFMs that can work immersed in water [4]. An AFM tip can deliver forces from 10^{-14} to 10^{-8} N and can image at Angstrom resolution in the z dimension and around 5 nm in lateral dimension (resolution of lateral dimension depends on tip radius). A protein can be grafted to a surface and can be probed by indenting with the AFM tip. With this technique, it is possible to study a force-strain measurement of the protein. However, the common AFM based experiments involve the study of unfolding of

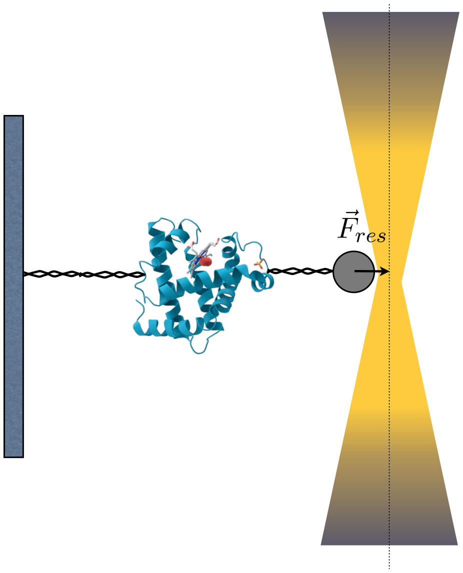

Figure 1.1: Using an optical tweezers to force proteins. The laser beam is brought to a fine focus and a dielectric sphere is trapped in the beam. The biomolecule is tethered to a fixed surface from one end and tethered to the dielectric sphere from the other end. The laser beam is displaced to deform the protein.

protein domains upon mechanical forcing [5]. AFM indentation generally unfolds the protein, which is not suitable to study mechanical properties of proteins in their native state.

Optical tweezers

Optical tweezers use biomolecules tethered from one end to a fixed surface and the other end tethered to an optically trapped bead [7, 8]. Recent research developments have opened the possibility of applying torque on biomolecules in addition to a force between two points [9]. The major limitation here is the resolution that is overwhelmed by the thermal noise.

Fig. 1.1 shows the basic setup of an optical tweezers to study the deformation of a biomolecule. In this technique, a laser beam is focused to a fine point using a high numerical aperture objective. A dielectric sphere can be trapped at the focus of the beam due to the restoring force F_{res} on the sphere, towards the center of the beam. The optical field induces a dipole moment in the sphere and this electric dipole experiences a non-zero force in the presence of a spatially non-uniform electric field. The restoring force F_{res} on the dielectric sphere is

$$F_{res} = \frac{\alpha}{2} \cdot \nabla E^2 = \frac{2\pi n_0 a^3}{c} \Big(\frac{m^2 - 1}{m^2 + 2} \Big) \nabla I \tag{1.1}$$

where α is the polarizability of a dielectric sphere, c is the speed of light, n_0 is the refractive index of the medium, m is the relative refractive index of the material of the dielectric sphere, a is the radius of the dielectric sphere and I is the intensity of the beam. For small displacements (below about 150 nm), the restoring force can be assumed to be linear in displacement, similar to a spring. The spring constant generally varies from 5×10^{-3} to 1 pN/nm while a force of 0.1 pN to 100 pN can be applied on biomolecules [6].

Försters Resonance Energy Transfer (FRET)

FRET is a fluorescence-based technique in which two chromophores can be used to gauge the distance between them (distance range 1 to 10nm). The donor chromophore absorbs light from the excitation laser and goes to an excited state and a nearby acceptor chromophore can absorb energy from the excited donor via a non-radiative process and emit fluorescence light.

The efficiency of the non-radiative energy transfer mechanism mainly depends on three parameters. They are, the donor−acceptor distance (r), the degree of spectral overlap of the donor emission spectrum and the acceptor absorption spectrum (J) and the relative orientation of the donor emission dipole moment and the acceptor absorption dipole moment (k).

$$E = \frac{1}{1 + (r/R_0)^6} \tag{1.2}$$

where R_0 is the Förster distance for the donor−acceptor pair given by

$$R_0^6 = \frac{9000 Q_0 (\ln 10) k^2 J}{128 \pi^5 n^4 N_A} \tag{1.3}$$

In the expression for R_0, Q_0 is the fluorescence quantum yield of the donor in the absence of the acceptor, n is the refractive index of the medium and N_A is the Avogadro's number. FRET can be used to determine the conformational change in proteins and there has been a great deal of work done in this field [10, 11].

The basic idea is to label the protein at two appropriate sites with the donor and the acceptor. A conformational change of the protein due to a binding event (or in response to a perturbation) can result in a change of the donor-acceptor distance, which in turn change the fluorescence efficiency. Even though FRET can be effectively used to observe conformational changes in proteins, it is not suitable to study the materials properties of them. The main reason is the limited resolution of ~ 1 nm.

1.2.2 A rheology experiment on proteins

To elucidate new properties of proteins beyond the linear elasticity regime, I used a setup developed at the Zocchi lab to perturb proteins in their native state. In these experiments, an AC force is applied on proteins and their mechanical response is measured. These forces are in the pico Newton range, and the protein under interrogation is in the native state. This experimental setup can measure the response of the protein at different frequencies or at different amplitudes of forcing. These show the different mechanical regimes under which the protein is operating.

In chapter 2, a rheology experiment on a voltage gated ion channel is discussed, in which the deformation of the protein was gauged by measuring the channel current. Chapter 3 gives details of a rheology experiment on a globular protein, in which the deformation amplitude was measured with an optical method.

In addition, chapter 3 discusses the effect of temperature on the mechanical properties of the folded state of a protein. Previous studies have shown that proteins become softer with increasing temperature, but exactly which parameters become softer was not clear. Another aspect that I address is the influence of the surface of the protein on its mechanical properties. Many proteins have a large fraction of its amino acids exposed to the solvent and these residues form hydrogen bonds with water molecules. Therefore, it is a valid question to ask how much influence can the surface of the protein have to its dynamics.

1.3 Bio-inspired systems

In addition to the measurements on the materials properties of proteins, I conducted experiments that used the properties of these proteins for new applications. One such instance that is discussed in chapter 4 is a sensor platform for biomolecules. This sensor operates by detecting a change in materials properties of a protein when a substrate molecule binds on it. Previous studies have found that proteins show a stiffening upon binding of its substrate [59, 60, 61]. Using localized surface plasmon resonance in combination with the nano rheology method, this technique can detect the change in stiffness of the protein accurately with a very robust signal.

Another bio inspired system that will be discussed is an artificial axon system. There are both previous and on going research on artificial axons, based on electronic circuits [12] in which the electrical behavior of a neuron is reproduced by an electronic circuit. Usually, using Very Large Scale Integration (VLSI) technology, chips with thousands of such neurons are fabricated to produce complicated networks similar to the brain [13]. I took a different approach, where the artificial axon is constructed with the basic elements that are found in the real system, i.e. using ion channels, phospho lipids etc. With further experimentation, this system has the potential to be realized in the same scale corresponding to an actual neuron. By borrowing techniques from micro fabrication, these neurons can be constructed on scaffolds patterned on silicon wafers, opening the possibility to realize complex neuron networks.

CHAPTER 2

Rheology of ion channels

2.1 Introduction

Ion channels are essential membrane proteins responsible for maintaining the none-equilibrium state of life of an individual cell or of a whole organism. Some functionalities of ion channels include gating of ions with high specificity, gating due to external stimuli molecules, pH dependent gating, mechanical force dependent gating, temperature dependent gating etc. Voltage gated ion channels in particular respond to the trans membrane electric field and these channels are the workhorses of the action potentials in neurotransmission.

The voltage gated ion channel used in this study, KvAP, is from an Archaea bacteria (Archaea Aeropyrum pernix). The Archaea bacterium was discovered in a deep-sea volcanic vent where the bacterium was living at temperatures $\sim 90\,^{\circ}\mathrm{C}$. In our experiments, KvAP was studied at a much lower temperature of $\sim 20\,^{\circ}\mathrm{C}$. The ion channel KvAP is a tetramer with a central pore of approximately 8 Å (from crystal structure PDB ID 1ORQ) and with a typical K^{+} ion flux of about 10^{8} ions/sec. The MacKinnon lab did a functional characterization of the KvAP channel [15] and found that the channel has a conductivity of 170 pS, the channel undergoes inactivation similar to other Kv channels and pore blocking toxins bind to block KvAP in a similar manner to other Kv channels etc.

There has been a tremendous amount of research on these channels since the days of Hodgkin and Huxley. But the typical electrophysiological measurements

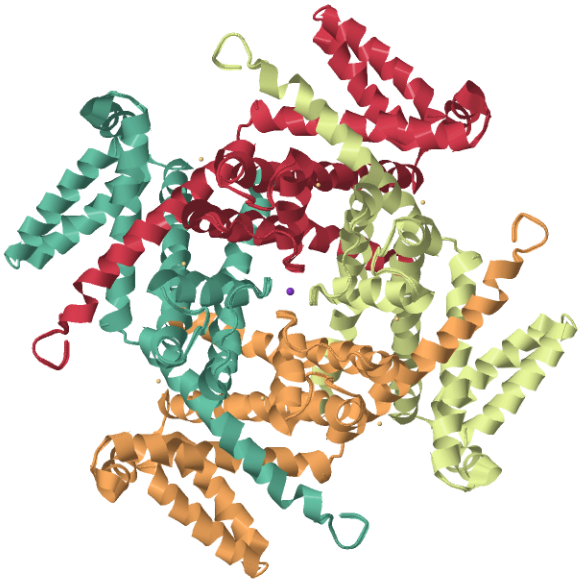

Figure 2.1: Top view of the crystal structure of KvAP. The image was generated from the crystal structure with PDB ID 1ORQ. The image shows that the channel is a tetramer. In addition, a K^+ ion can be seen in the central conduction pore.

done with voltage gated ion channels remained essentially the same; apply a DC voltage to hyperpolarize (closed state) channels for a prolonged period and then apply a depolarizing step to open channels for a brief period. We are interested in the dynamics of the voltage sensing unit which is responsible for gating of the channel and our approach was to apply a force $f(\omega)$ on the voltage sensing domain and study its motion, using a rheology experiment.

2.2 Structure of KvAP

KvAP was the first voltage gated potassium channel to have its crystallographic structure solved, which was done by the McKinnon group in 2003 [14]. Fig 2.1 shows a 3D rendering of a top view of the solved crystal structure of KvAP in which the four monomer units with the central conduction pore can be seen.

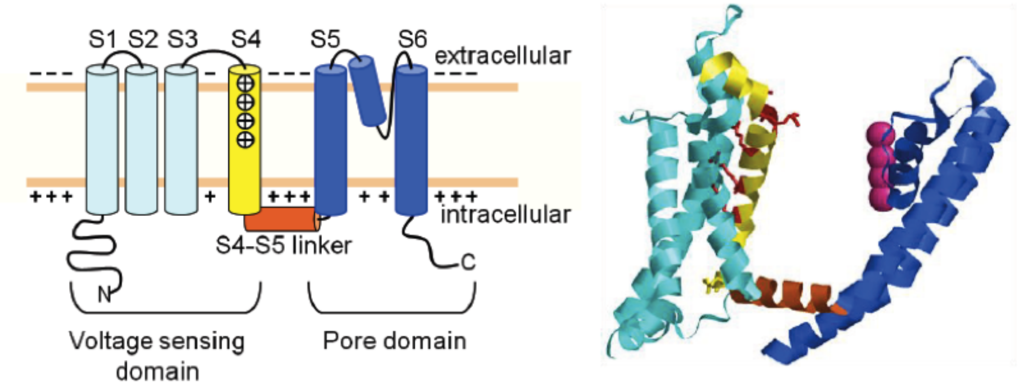

Figure 2.2: Structure of a KvAP monomer. The cartoon representation shows the arrangement of helices in the functional channel. The voltage-sensing domain contains the helices S1 to S4. S4 is a positively charged helix due to the presence of Arginine residues. S5 and S6 form the pore domain. On the right is a crystal structure of a monomer from PDB ID 2R9R where the same color code as in the cartoon representation on the left is used.

Fig 2.2 shows the crystallographic structure of a monomer as well as a cartoon representation of each alpha helix. The six transmembrane helices of the Kv channel monomer are organized as shown in the cartoon in Fig 2.2. Helices S1, S2 and S3 support the positively charged helix S4 and these four helices together form the voltage-sensing domain (VSD). The pore is made by the two helixes, S5 and S6. This pore is connected to the motion of the VSD via a crosslinking helix, termed the S4-S5 linker. Pink spheres on the crystal structure of the monomer in Fig 2.2 represent potassium ions moving in a single file motion inside the selectivity filter.

2.3 The selectivity filter of a Kv channel

All potassium ion channels have a conserved sequence of amino acids that form the selectivity filter (TVGYG) [16]. The selectivity filter of Kv channels have the ability to selectively pass K^+ ions with a high specificity while blocking ions such as Na^+. In fact, this selectivity is found to be around 1 Na^+ ion for every 150 K^+ ions [17]. The underlying principle behind this remarkable selectivity is the hydration shell of these ions. In order to enter the pore of the channel, the ions must shed the hydration layer and this comes at an energy cost. The 150-fold selectivity for K^+ over Na^+ arises due to this higher energy cost of Na^+ to shed its hydration shell. This was revealed in the crystal structure of a Kv channel with bound K^+ ions [18], the K^+ ions were nearly dehydrated and the interactions with water molecules were replaced by carbonyl oxygen on the backbone of the selectivity filter. The free energy difference of shedding the hydration shell for Na^+ is about 10 k_BT higher than that of K^+ [19].

The ions move in the pore in a single file motion such that entering of an ion from one side of the pore causes another ion at the opposite end to leave. Studies show that there are a few binding sites for the K^+ ions in the pore. For example the KvAP channel has four sites for K^+ ions in its selectivity filter [14]. Fig 2.3 shows the selectivity filter of the proton gated KcSA channel [20]. The potassium ions have four binding locations inside the selectivity filter.

2.4 Voltage sensor domain of KvAP

The Kv channels have an interesting mechanism by which they sense the electric field. These channels have a charged alpha helix that responds to the electric field and this charged helix was found to be composed of a conserved sequence of amino acids among the Kv channel group. Fig 2.2 shows this charged helix as

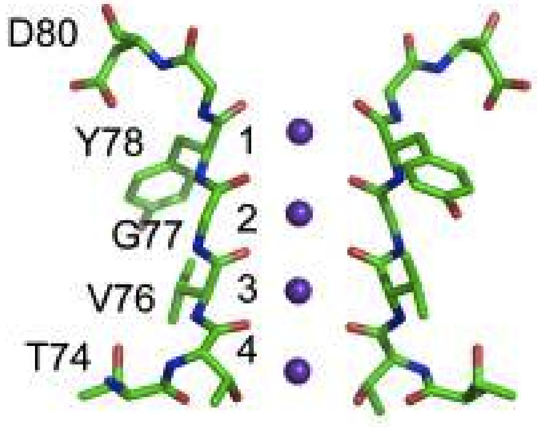
D80
Y78
G77
V76
T74
1
2
3
4

Figure 2.3: The selectivity filter of the ion channel KcSA [20]. There are four binding sites for the potassium ions inside the filter and ions move in a single file motion.

S4 and the charge in the S4 helix comes about mainly from the Arginine amino acids.

Even before the availability of a crystal structure of Kv channels, researchers had an idea that these Arginine groups are responsible for sensing the electric field. For example, there are studies in which the mutation of Arginine residues to other uncharged amino acids results in the loss of the voltage sensitivity [21]. The motion of these "gating charges" was measured by many techniques such as detecting the "gating currents" [22, 23], by FRET [24, 25] or by Biotin-Avidin accessibility [26]. After the availability of the high-resolution crystal structure of Kv channels in 2003, there have been a growing number of studies deploying MD simulations to understand the gating process [27, 28, 29]. The motion of the voltage-sensing domain is coupled to the pore via S4-S5 linker. Each channel has four VSDs as the channel is a tetramer. It is believed that all four VSDs undergo a concerted motion to open (or close) the channel.

2.5 Inactivation of Kv channels

With prolonged opening, Kv channels become non conductive and enter a state called the inactive state. While the opening and closing of the channels are in the millisecond time scales, inactivation happens at a much slower time scale of about half a second. The crystal structure of a Kv channel under low salt conditions showed that the selectivity filter was constricted under these conditions (Fig. 2.4) [18]. The inactivation process was thought to depend on the occupancy of K^+ ions inside the filter domain as a selectivity filter bound to ions is less likely to collapse and inactivate the channel.

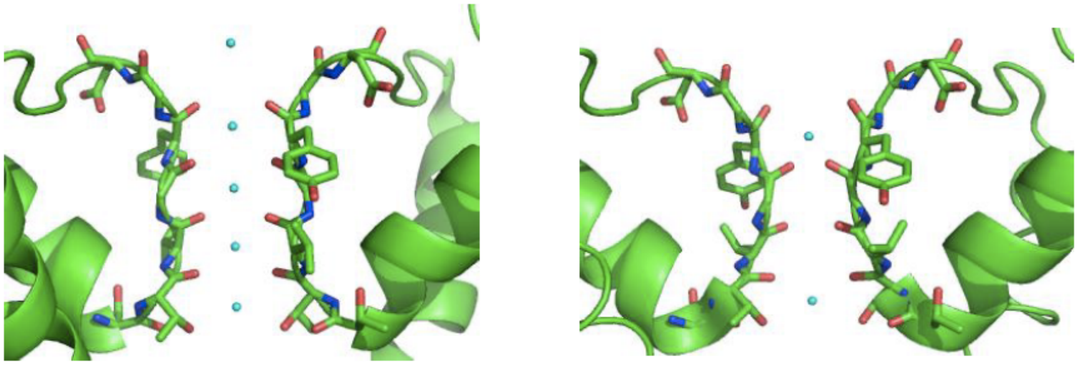

Figure 2.4: The selectivity filter of a Kv channel upon inactivation. Structure of the selectivity filter in (a) high K$^+$ and (b) low K$^+$ environments. The blue dots represent K$^+$ ions in the crystal structure. Under low salt conditions, the filter is collapsed blocking the movement of ions. Adapted from Andrew Wong thesis (Manipulation of Molecular Processes with DNA Molecular Springs), structure generated from PDB ID 1K4C and 1K4D.

2.6 Preparation of KvAP proteoliposomes

In this section I will give details of the protocol used to express KvAP channels and reconstitute them in lipid vesicles.

2.6.1 Expression of KvAP

Wild type KvAP was obtained as a gift from Prof. Rod McKinnon group at Rockefeller. The wild type KvAP (wtKvAP) cloned in the vector pQE60 has an internal cysteine at site 247 and the mutant used in these experiments had this internal cysteine mutated to a Serine. Site directed mutagenesis was performed with the QuickChange Site-Directed Mutagenesis kit from Agilent using the DNA primer gcctgagcctagctgcagccccgccaagc. The resulting KvAP gene was verified to have the proper mutation by performing gene sequencing at the UCLA GenoSeq Laboratory. After obtaining the cysteine-removed version of KvAP, it was expressed in E. coli. Cells. The following section gives an outline of the expression process of KvAP.

All procedures of protein expression and purification unless otherwise mentioned was performed at room temperature. The cell line used to express the KvAP protein was Agilent XL1-Blue cells and this protocol was adapted from [15].

Expression day 1:

- A 25 μL aliquot of frozen cells was taken from the $-80\,^{\circ}$C freezer and was allowed to though on ice for about 15 minutes. These aliquots were stored in 1.5 mL microcentrifuge tubes.
- After complete thawing of the cells, 0.45 μL of β-Mercaptoethanol was added to the cells and the mixture was gently swirled. The cells were kept in ice for an additional 10 minutes, swirling gently every 2 minutes.
- At the end of the 10-minute interval, 2 μL of the plasmid DNA was added to the cells. The KvAP plasmid used for this step is a 200 times diluted version from the Plasmid Miniprep elution.
- The cells were kept in ice for an additional 30 minutes. In the mean time, a water bath was turned on and set to 42 °C and the SOC medium was allowed to pre warm to 42 °C in the water bath.
- After the 30-minute incubation of cells, they were heat shocked for exactly 45 seconds at 42 °C and immediately transferred to ice for another 2 minutes.
- 350 μL of pre warmed SOC medium was added to the cells and incubated for 1 hour in an orbital shaker at 37 °C and 250 rpm.
- While the cells were incubating, the LB agar plates having the antibiotic Ampicillin was taken out from the 4 °C fridge and they were kept in the

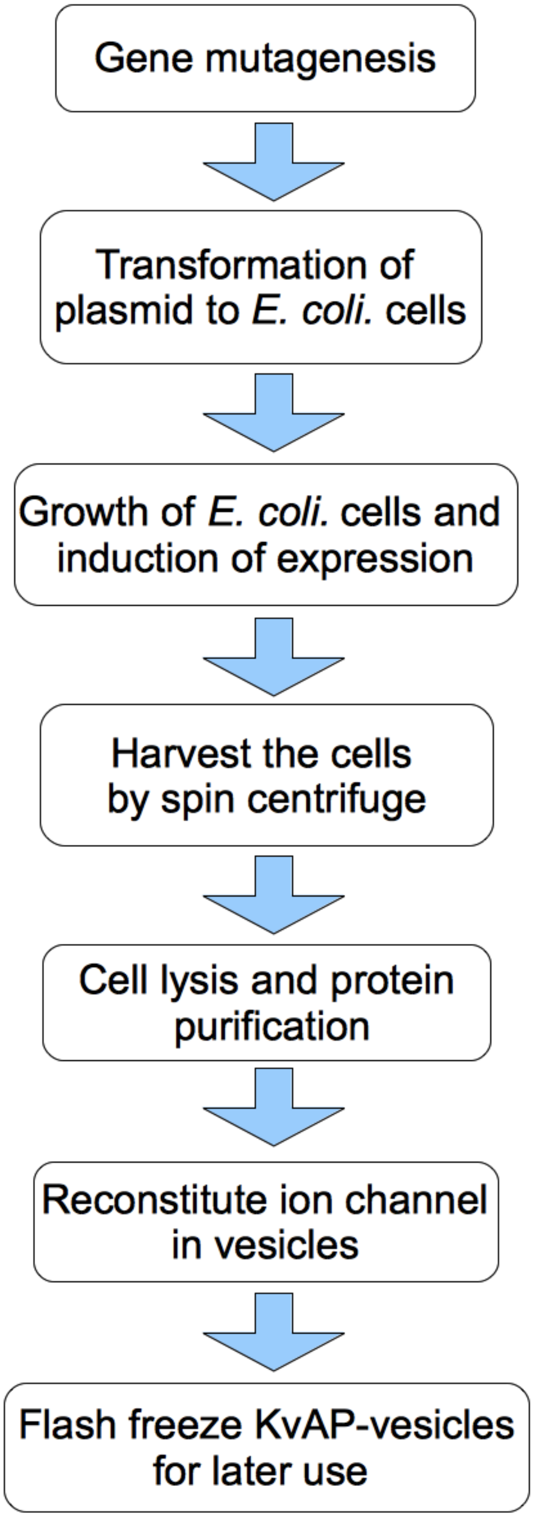
Gene mutagenesis
Transformation of plasmid to *E. coli.* cells
Growth of *E. coli.* cells and induction of expression
Harvest the cells by spin centrifuge
Cell lysis and protein purification
Reconstitute ion channel in vesicles
Flash freeze KvAP-vesicles for later use

Figure 2.5: Flow chart of KvAP expression and purification.

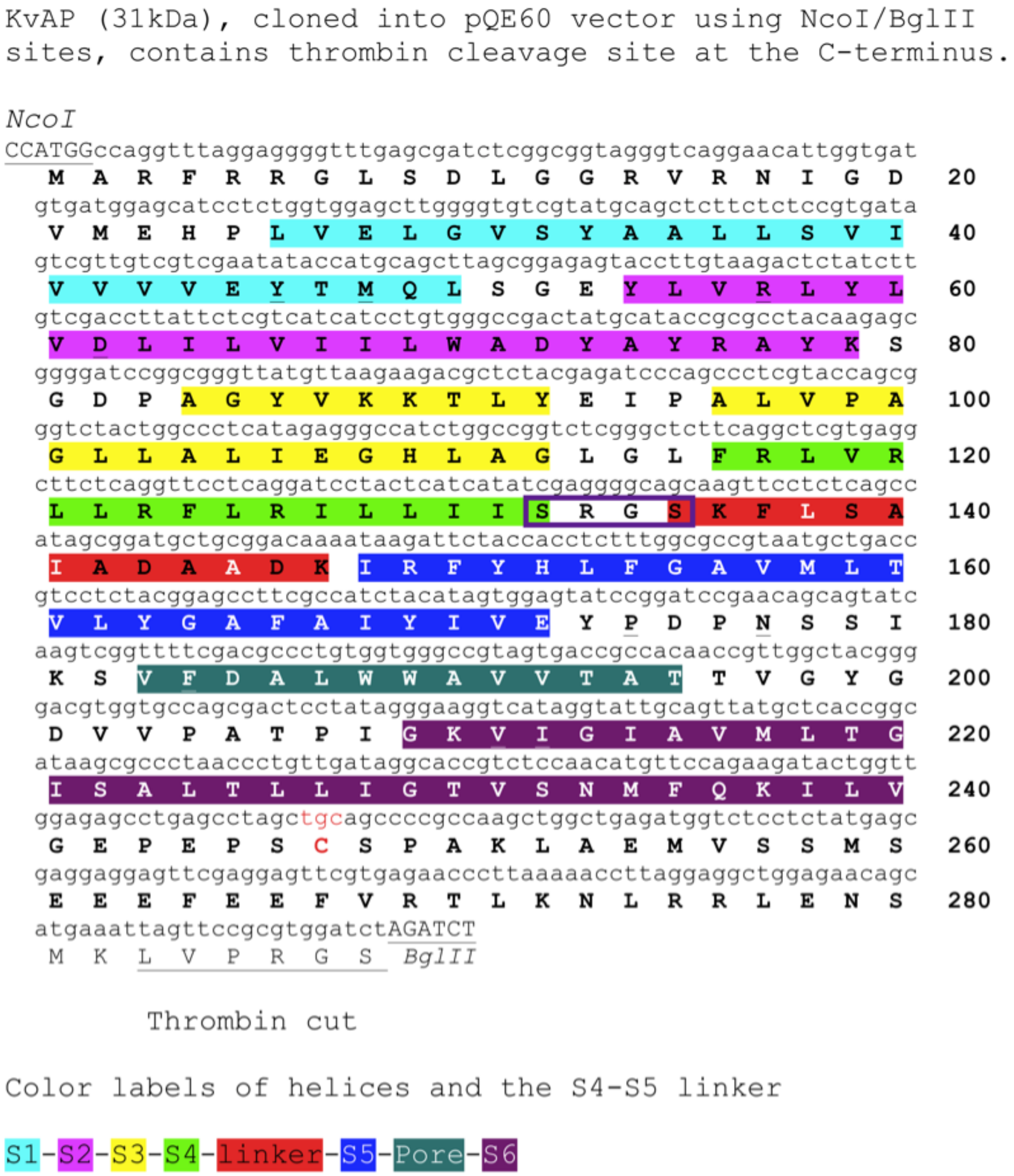

KvAP (31kDa), cloned into pQE60 vector using NcoI/BglII sites, contains thrombin cleavage site at the C-terminus.

```
NcoI
CCATGGccaggtttaggaggggtttgagcgatctcggcggtagggtcaggaacattggtgat
   M  A  R  F  R  R  G  L  S  D  L  G  G  R  V  R  N  I  G  D   20
  gtgatggagcatcctctggtggagcttggggtgtcgtatgcagctcttctctccgtgata
   V  M  E  H  P  L  V  E  L  G  V  S  Y  A  A  L  L  S  V  I   40
  gtcgttgtcgtcgaatataccatgcagcttagcggagagtaccttgtaagactctatctt
   V  V  V  V  E  Y  T  M  Q  L  S  G  E  Y  L  V  R  L  Y  L   60
  gtcgaccttattctcgtcatcatcctgtgggccgactatgcataccgcgcctacaagagc
   V  D  L  I  L  V  I  I  L  W  A  D  Y  A  Y  R  A  Y  K  S   80
  ggggatccggcgggttatgttaagaagacgctctacgagatcccagccctcgtaccagcg
   G  D  P  A  G  Y  V  K  K  T  L  Y  E  I  P  A  L  V  P  A  100
  ggtctactggccctcatagagggccatctggccggtctcgggctcttcaggctcgtgagg
   G  L  L  A  L  I  E  G  H  L  A  G  L  G  L  F  R  L  V  R  120
  cttctcaggttcctcaggatcctactcatcatatcgagggcagcaagttcctctcagcc
   L  L  R  F  L  R  I  L  L  I  I  S  R  G  S  K  F  L  S  A  140
  atagcggatgctgcggacaaaataagattctaccacctctttggcgccgtaatgctgacc
   I  A  D  A  A  D  K  I  R  F  Y  H  L  F  G  A  V  M  L  T  160
  gtcctctacggagccttcgccatctacatagtggagtatccggatccgaacagcagtatc
   V  L  Y  G  A  F  A  I  Y  I  V  E  Y  P  D  P  N  S  S  I  180
  aagtcggttttcgacgccctgtggtgggccgtagtgaccgccacaaccgttggctacggg
   K  S  V  F  D  A  L  W  W  A  V  V  T  A  T  T  V  G  Y  G  200
  gacgtggtgccagcgactcctatagggaaggtcataggtattgcagttatgctcaccggc
   D  V  V  P  A  T  P  I  G  K  V  I  G  I  A  V  M  L  T  G  220
  ataagcgccctaaccctgttgataggcaccgtctccaacatgttccagaagatactggtt
   I  S  A  L  T  L  L  I  G  T  V  S  N  M  F  Q  K  I  L  V  240
  ggagagcctgagcctagctgcagccccgccaagctggctgagatggtctcctctatgagc
   G  E  P  E  P  S  C  S  P  A  K  L  A  E  M  V  S  S  M  S  260
  gaggaggagttcgaggagttcgtgagaacccttaaaaaccttaggaggctggagaacagc
   E  E  E  F  E  E  F  V  R  T  L  K  N  L  R  R  L  E  N  S  280
  atgaaattagttccgcgtggatctAGATCT
   M  K  L  V  P  R  G  S  BglII

         Thrombin cut
```

Color labels of helices and the S4-S5 linker

S1-S2-S3-S4-linker-S5-Pore-S6

Figure 2.6: Sequence of the wild type KvAP cloned in PQE60 vector. The thrombin cleavage site was added to remove the His-tag after the protein purification process.

incubator oven at 37 °C.

- At the end of the 1-hour incubation of the cells, they were spread evenly on LB agar plates and kept overnight at 37 °C. The volumes of cells used in the plates were 5 μL, 25 μL and 100 μL. In all three cases, a 100 μL pool of SOC medium was added to the plate initially and the cells were added on to this SOC pool.

Expression day 2:

After about 16 hours of incubation, the cells grow to form distinct colonies. The following steps must be performed near a flame to have a sterile environment.

- 5 mL of autoclaved LB buffer was added to 3 sterile glass test tubes. Then 5 μL of Ampicillin stock solution (100 mg/mL in DI water) was added to each tube.
- Colonies from the overnight incubation were selected at random and they were inoculated into the LB-Amp test tubes using a sterile 200 μL pipette tip.
- The test tubes were then incubated at 37 °C and 225 rpm for 5 hours. A successful inoculation results in a cloudy LB solution in a few hours.
- In the mean time, four flasks of 1 L LB buffer and one flask of 500 mL LB buffer were prepared. They were autoclaved at 120 °C in steam for 1 hour. Ampicillin from the stock solution was added in a thousand-fold dilution to the LB flasks after they reached room temperature.
- At the end of the 5-hour incubation, a test tube that shows normal cell growth was chosen and was added to the 500 mL LB culture.
- The 500 mL culture was grown overnight at 37 °C, 255 rpm for about 16 hours.

Expression day 3:

- Added the cell culture from the overnight 500 mL growth medium to the 1 L LB flasks such that the initial optical density (OD) in the 1 L medium was at 0.1. Optical density was measured in a 1 cm path length, clear plastic cuvette at 600 nm wavelength.
- The 1 L cultures were then allowed to grow at 37 °C, 225 rpm. The OD was measured every 30 minutes. After about 5 hours, the OD reached ~ 1.
- Protein expression was induced with 0.4 mM IPTG when the OD reached 1. $BaCl_2$ was also added to the LB media to a final concentration of 10 mM. Thereafter, the cell cultures were left to incubate for 4 hours before harvesting the cells.
- After the 4-hour incubation, the cells were spun at 4000 rpm for 20 minutes to form a pellet and the supernatant was discarded. The cell pellet was frozen at -20 °C for later use.

2.6.2 Purification of KvAP

A homogenizer is used to break down the cells, which subject the cells to a high-pressure difference. As KvAP is a membrane protein, it migrates to the cell wall when expressed in E. coli. cells. Since the ion channel protein is embedded in the cell wall debris, the lysis of the cells does not transfer the ion channel to the buffer solution upon lysis. In order to transfer the ion channels from the cell wall debris to the solution phase, the mild detergent Decylmaltoside is used. The detergent due to its hydrophobic chain will shield the hydrophobic lipid exposed regions of the ion channel and transfer the channel to the solution phase.

Once the ion channel protein is transferred to the solution phase, it must be separated from native bacterial protein and this is achieved via Immobilized

Metal Affinity Chromatography (IMAC) [30]. The ion channel KvAP is expressed with a genetically added C terminus His tag (6 Histidine residues) which binds to Cobalt ions forming a complex [31]. Since native proteins of the E. coli. cell does not carry the His-tag, they will not to bind to Cobalt ions. Fig 2.7 shows a cartoon diagram of a Cobalt ion forming a complex with a His-tagged protein. The standard practice in molecular biology is to use Agarose beads that have Cobalt ions grafted on them. These beads have macroscopic dimensions which helps to trap them in a filter. Once the protein is bound to the Cobalt beads, a competing binding agent to Cobalt ions must be used to elute the protein. In our experiments, we use high concentration Imidazole buffer as the competing binding agent to elute the protein.

2.6.3 Protein purification protocol

The following buffers were used for cell lysis and protein purification steps. Stock solutions of 1.0 M KCl, 500 mM Tris-HCl pH 8.0, 1.0 M Imidazole pH 8.0 and 500 mM Decylmaltoside (in DI water) were used in preparing the buffers. The volumes of stock solutions required to make 50 mL of the corresponding buffers are given in Table 2.1. All buffers were filtered with 0.2 μm filters before usage.

The cell pellet, which was stored at $-20\,^{\circ}$C after protein expression was removed from the freezer and was thawed in ice for about 30 minutes. In order to prepare the lysis buffer, the components Lysozyme, Protease inhibitor cocktail, DNase and β-Mercaptoethanol were added freshly to the buffer. The detergent Decylmaltoside must be added to the cell lysate after the lysis step.

After thawing the cells, 50 mL of lysis buffer was added to the cells and the cell-lysis buffer mixture was swirled thoroughly to dissolve any solid coagulates. Cell lysis was performed using an Avestin EmulsiFlex-C3 homogenizer. The cell mixture was passed through the homogenizer for a total of 3 times at an operating

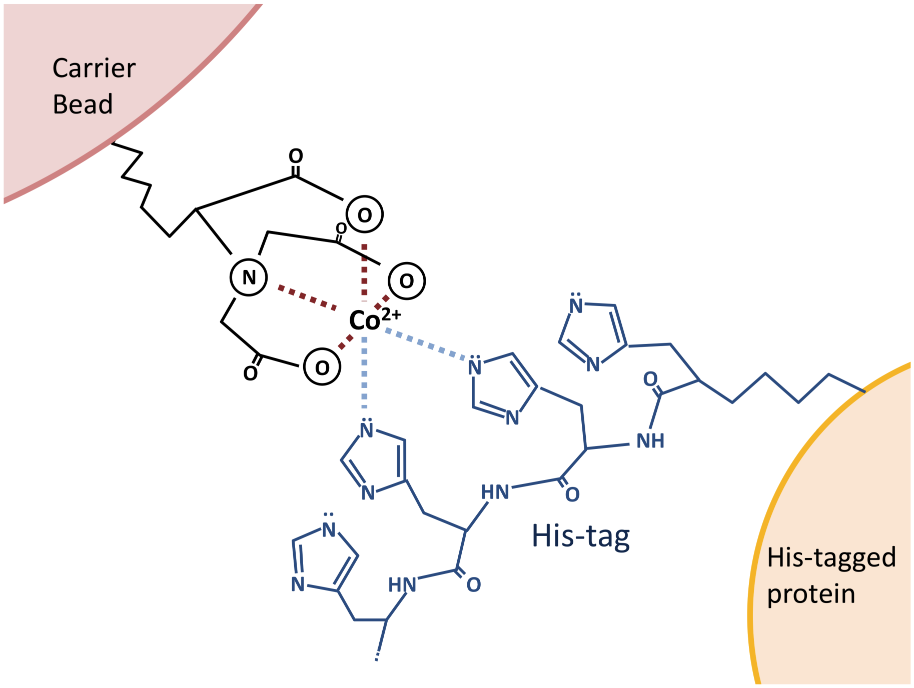
Carrier Bead
O
O
O
N
O
O
O
Co2+
N
N
N
N
O
NH
N
N
HN
O
His-tag
N
N
HN
O
His-tagged protein

Figure 2.7: Protein purification with Cobalt beads. The His-tagged protein forms a complex with the metal ions Co or Ni. The metal ion is grafted on a agarose bead with a Nitrilotriacetic acid (NTA) resin. A competing agent such as Imidazole can disrupt the His-tag metal ion complex at high enough concentrations.

	Stock solution	Amount	Final Concentration
Wash buffer	1 M KCl	5.0 mL	100 mM
	0.5 M Tris-HCl pH 8.0	2.0 mL	20 mM
	1.0 M Imidazole pH 8.0	1.0 mL	20 mM
	0.5 M Decymaltoside	0.5 mL	5 mM
	DI water	41.5 mL	
Lysis buffer	1 M KCl	5.0 mL	100 mM
	0.5 M Tris-HCl pH 8.0	5.0 mL	50 mM
	DI water	35 mL	
	Lysozyme powder	10 mg	0.2 mg/mL
	Protease inhibitor cocktail	1 tablet	
	DNase 10 mg/mL	10 μL	2 μg/mL
	14 M β-Mercaptoethanol	7.4 μL	2.0 mM
	0.5 M Decymaltoside	4.0 mL	40 mM
Elution buffer	1 M KCl	5.0 mL	100 mM
	0.5 M Tris-HCl pH 8.0	2.0 mL	20 mM
	1.0 M Imidazole pH 8.0	20 mL	400 mM
	0.5 M Decymaltoside	0.5 mL	5 mM
	DI water	22.5 mL	

Table 2.1: Preparation of KvAP protein purification buffers.

pressure of 10000 psi. After lysing the cells, Decylmaltoside was added to a final concentration of 40 mM to the cell lysate solution and was left to nutate for 3 hours at room temperature.

After the 3-hour incubation of the cell lysate with 40 mM detergent, the cell lysate was centrifuged at 15000 rpm for 30 minutes to sediment the cell debris. After centrifuging, the supernatant was collected and was mixed with pre washed Cobalt beads (Clonetech) and the solution was gently rotated for 1 hour. Cobalt beads were washed with 20 mL Wash buffer by using a gravity flow column with a filter (to retain beads). Typically, about 2 mL of Cobalt beads were used for a 4 L expression. After the 1-hour incubation, the mixture was passed through a gravity flow column four times (with a filter) to collect all the Cobalt beads.

Next, the beads were washed with 30 mL of Wash buffer to remove any non-specifically bound proteins. A small volume from the wash step was collected for later SDS PAGE analysis. Finally, the protein was eluted with Elution buffer, adding 1 mL of Elution buffer at a time up to a total volume of 10 mL.

The yield of protein purification was measured by the Bradford assay and Thrombin (Sigma Aldrich, bovine Thrombin) was added to the KvAP elution to cleave the His-tag overnight at 16 °C. The added Thrombin concentration was 1.5 units of thrombin per each milligram of KvAP. Before adding the Thrombin, about 20 μL from the eluted protein was separated for SDS PAGE analysis.

On the following day, the ion channels were further purified with size exclusion chromatography via an HPLC (BioRad). The size exclusion column used was a Superdex-200 column (GE Healthcare) and KvAP HPLC buffer (100 mM KCl, 20 mM Tris-HCl at pH 7.5 and 5 mM Decylmaltoside) was used as the working buffer for the HPLC purification step. Fractions corresponding to the ion channel were collected to one tube and the protein concentration was determined via Bradford assay.

2.6.4 Reconstitution of KvAP channels in lipid vesicles

The purified KvAP channel must be incorporated in to small lipid vesicles. Lipid vesicles are produced by sonication of a solution of lipids dissolved in an aqueous buffer. Sonication produces small lipid vesicle with an average size of around 20 nm. These small vesicles are first dissolved in detergent and then mixed with the purified ion channel solution. The slow removal of detergent from this solution results in the migration of ion channels to the small lipid vesicles as exposing the hydrophobic regions of the protein to the buffer solution is energetically unfavorable.

Preparation of the lipid

The lipid DPHPC (Avanti Polar lipids) was purchased as a solution in chloroform at a concentration of 25 mg/mL. Upon arrival, the lipid was aliquoted in glass vials with volumes of 10 μL and 100 μL. These can be stored at $-80\,^{\circ}$C for about 1 year. The smaller 10 μL lipid aliquot was used to paint lipid bilayers while the 100 μL aliquot was used to reconstitute KvAP channels in to vesicles.

The drying of the lipid was performed inside a fume hood. The lipid vial was first dried with a gentle stream of pure N_2 for 10 minutes. Then about 250 μL of pentene was added to the dried lipid vial and the vial was vortexed gently to dissolve the lipid. After an additional 10 minute drying under pure N_2, the vial was kept under vacuum for about 4 hours. The dried lipid can then be used either to prepare lipid bilayers or for ion channel reconstitution.

Producing small unilamellar vesicles

In order to produce small lipid vesicles, the dried lipid was first dissolved in RC buffer (450 mM KCl, 10 mM HEPES, pH 7.4, filtered at 0.2um) at a concentration of 20 mg/mL. The solution was vortexed for about 30 minutes to produce a cloudy suspension of lipids dissolved in RC buffer. After the 30 minute vortex period, the vial was sonicated in a bath sonicator till the opaque solution turned clear. In order to minimize the time required for this process, the sonication must be performed with a high sonication power. Raising the temperature of the bath to $\sim 40\,^{\circ}$C improves the sonication process.

Next, the detergent concentration of the vesicle solution was raised to 10 mM. This was achieved with a stock solution of 400 mM detergent dissolved in RC buffer. After increasing the detergent concentration, the detergent stabilized vesicle solution was vortexed for 30 minutes and was kept at $4\,^{\circ}$C till the ion channel was ready.

Concentrating the ion channel sample

Usually, after the HPLC purification of the ion channel sample, the total volume of the sample could be around 4 mL. This must be concentrated to a volume of around 200 μL before adding to the lipid vesicle solution. The ion channels must be at a concentration of $\sim$ 10 mg/mL after concentrating.

Ion channels were concentrated with spin concentrators (Amicon Ultra 15) with a molecular weight cutoff of 10 KDa. Usually, spinning at 7000 rpm for 10 minutes was adequate to bring down the volume from around 4 mL to around 200 μL. This step was performed at $4\,^{\circ}$C. After the concentration step, the protein solution was collected to a 1.5 mL microcentrifuge tube.

Addition of lipid vesicles to ion channels

The ratio of ion channels to lipid vesicles must be adjusted depending on whether the goal is to perform single channel recordings or multichannel recordings. For multichannel recordings, a ratio of lipid mass to protein mass of around 3:1 produced good results consistently. If the aim is single channel recordings, the ratio of lipid mass to protein mass is around 1000:1. Depending on the amount of ion channel protein available after the concentration step, the lipid vesicle solution is added to the concentrated ion channel solution in the desired ratio. After adding the lipid vesicle solution and the protein solution, the concentration of detergent in the mixture is raised to 17 mM by using the stock solution of 400 mM detergent in RC buffer. This solution of lipid vesicles and ion channel proteins is incubated at room temperature for 2 hours with gentle vortexing every 20 minutes.

Detergent removal

The next step is to remove detergent from the solution and this is performed in two stages. In the first stage, the protein-lipid vesicle solution is passed through spin desalting columns (Zeba spin desalting columns, Thermo Pierce, 7500 MWCO). The majority of detergent from the bulk solution can be removed by using these spin desalting columns. The next stage is to use Bio-Beads SM2 (BIORAD) adsorbents over a period of 48 hours to remove the residual detergent in the solution. The spin desalting is performed in three columns consecutively to improve the detergent removal.

First, the residual buffer in the spin columns was removed by spinning at 1000 rcf for 2 minutes. Then the columns were washed 4 times with 2 mL of RC buffer. The RC buffer was removed by spinning the columns at 1000 rcf for 2 minutes. After the preparation of the columns, the protein-lipid vesicle sample was passed though each column at 1000 rcf for 2 minutes.

Bio beads must be pre cleaned before usage. They were washed with copious amounts of ethanol, DI water and finally with RC buffer. The pre cleaned bio beads were divided in to four 1.5 mL microcentrifuge tubes and the desalted protein-lipid vesicle solution was added to one of the bio bead tubes. These bio bead tubes were stored in 4 °C for 48 hours and the protein solution was transferred to a new bio bead tube every 12 hours. At the end of the 48-hour period, the proteoliposome solution was separated from the bio beads. The resulting proteoliposome solution was aliquoted to 10 μL samples in PCR tubes and was flash frozen using an ethanol-dry ice bath. The frozen ion channel samples were stored at $-80\,^{\circ}$C for later usage.

2.7 Electrophysiology setup to measure ion channel currents

Since KvAP is an ion channel, its activity can only be studied by incorporating KvAP channels to a lipid bilayer. KvAP can be transferred to a lipid bilayer via fusing proteoliposomes containing KvAP with the lipid bilayer. A lipid bilayer without any ion channels forms a giga ohm seal between two buffer compartments. Thus, only a very small leakage current results when a dc voltage difference is applied across the ion channel free lipid bilayer. In the case where there are functional ion channels present on the lipid bilayer, the application of a voltage difference across the bilayer results in a measurable ionic current. The resulting ionic current from KvAP channels was measured by a home built I to V converter.

Fig 2.8 shows an outline of the scheme used to measure ion channel currents. The ion channels are in a lipid bilayer which is stretched across a ~ 100 μm aperture fabricated in a plastic cup. The Teflon buffer chamber holds the plastic cup, foaming two chambers, cis chamber and trans chamber. Ag/AgCl electrodes are connected to the two buffer chambers and these electrodes are fed to a homebuilt head stage amplifier (head stage amplifier is an I to V converter). The Teflon chamber is mounted on an inverted microscope to observe the lipid bilayer formation. Output voltage from the head stage amplifier is fed to a low noise amplifier and then its digitized by a DAQ and recorded with the aid of custom software. The software also generates the command voltage pulse, which is converted to an

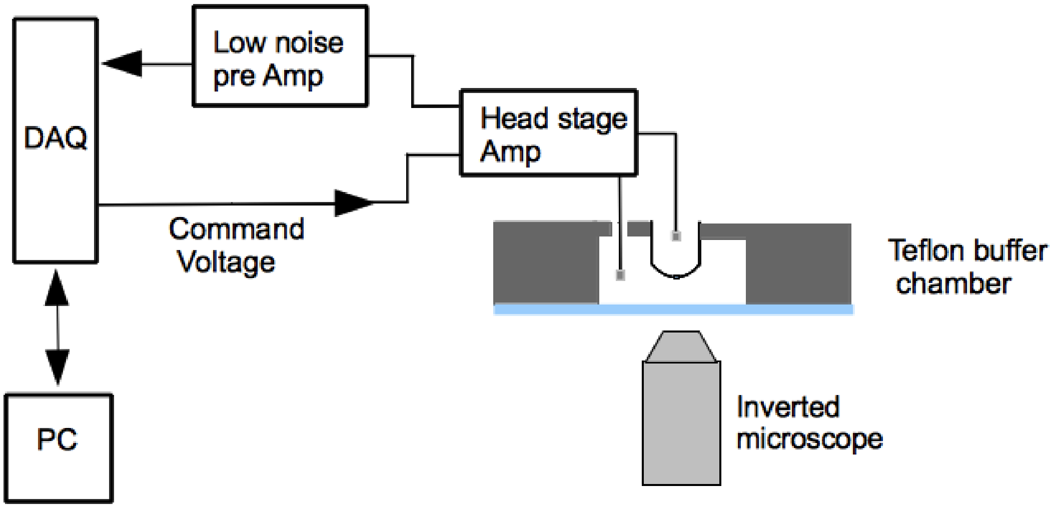

Figure 2.8: Electrophysiology setup to measure ion channel currents. Ion channels are incorporated to a lipid bilayer spanned across a $\sim$ 100 μm aperture fabricated in a plastic cup. The plastic cup is inserted to the Teflon buffer chamber. A head stage amplifier is used to clamp the voltage and measure the ionic current. A data acquisition system (DAQ) records the output from the head stage amplifier. The command voltage pulse for the experiment is given by the DAQ which is controlled by custom software.

analog level by the DAQ and fed to the head stage amplifier.

Figure 2.9 shows a detailed view of the Teflon buffer chamber. Ag/AgCl electrodes (Warner instruments) are used as the working electrodes. The plastic cup has an aperture of around 100 μm in diameter and a lipid bilayer is painted across this aperture by using a glass spatula. The procedure for producing the 100 μm aperture in the plastic cup was adapted from Wanderlin et al [32]. After the formation of the lipid bilayer, a small amount of the ion channel vesicle solution ($\sim$ 1 μL) is added to the cis chamber with a pipette. The ion channels are added closer to the lipid membrane as this helps to reduce the time for a vesicle to fuse

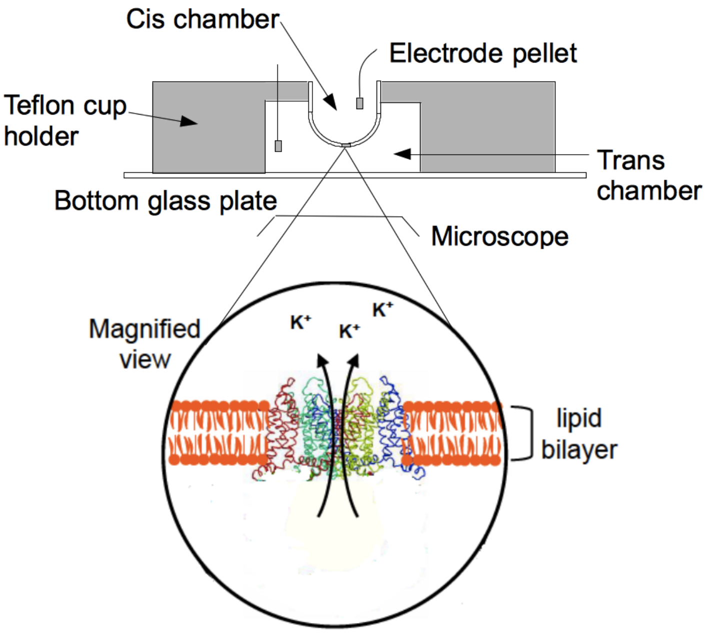
Cis chamber
Electrode pellet
Teflon cup holder
Trans chamber
Bottom glass plate
Microscope
Magnified view
K+
K+
K+
lipid bilayer

Figure 2.9: Setup for the formation of a lipid bilayer separating two fluid compartments. The Teflon cup holder chamber (same as Teflon buffer chamber in Fig. 2.8) has a glass slide at the bottom. The setup is mounted on an inverted microscope to observe the lipid bilayer. The bilayer is painted across the aperture with a glass spatula.

to the lipid bilayer. Stirring the cis chamber with a glass rod improves the fusion efficiency.

2.8 Response of the KvAP ion channel for DC pulses

The current trace shown in Fig. 2.10 is from a single KvAP channel while the potential difference across the membrane is kept at 60 mV. The channel remains open for a fraction of the time as evident from the trace. The fraction of time the channel spends in this open state is called the open probability and it is a function of the applied voltage difference across the membrane. The current produced by the opening of a single channel can be estimated to be around 10 pA from this

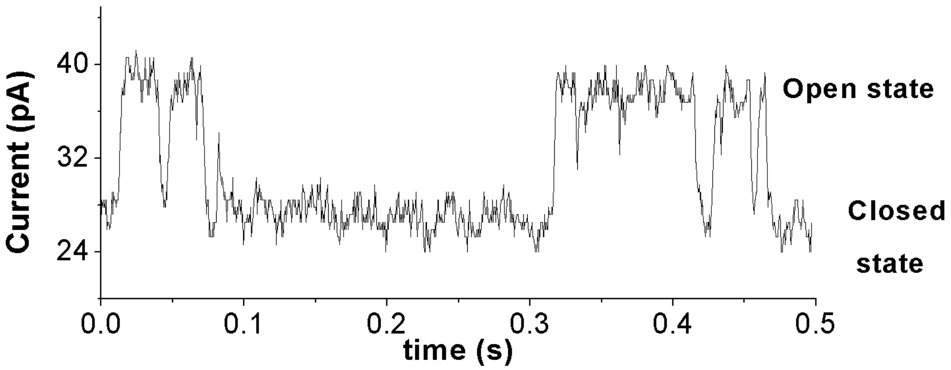

Figure 2.10: Current from a single KvAP channel. The channels were kept in the closed state for an extended period before stepping the voltage to 60 mV to record the current trace. Even though the membrane potential is 60 mV throughout the interval of the trace, the channel opens only during a fraction of the time. The current due to a single channel at 60 mV is 10 pA.

current trace and this value agrees with the known single channel conductance of 170 pS.

The current trace shown in Fig. 2.11 is from a multi channel sample. Initially the membrane potential is held at -120 mV for which the channels remain closed. Next the membrane voltage is stepped to 60 mV before bringing the potential back to -120 mV after a period of 1.2 s. The initial spike represents the capacitive transient that decays in about a millisecond. The ion channels open stochastically, the current plateaus in about 50 ms and then it decreases exponentially due to an independent process termed inactivation.

It is possible to produce an opening probability curve by obtaining multi channel current traces at different applied voltages. In order to produce an opening probability curve, the inactivation time constant must be measured from a current trace. Fitting an exponential decay to the decaying portion of the current trace gives the inactivation time scale. Suppose the inactivation time constant is τ and $I(t)$ is the measured current trace as a function of time. Thus $I(t) \times e^{(t/\tau)}$

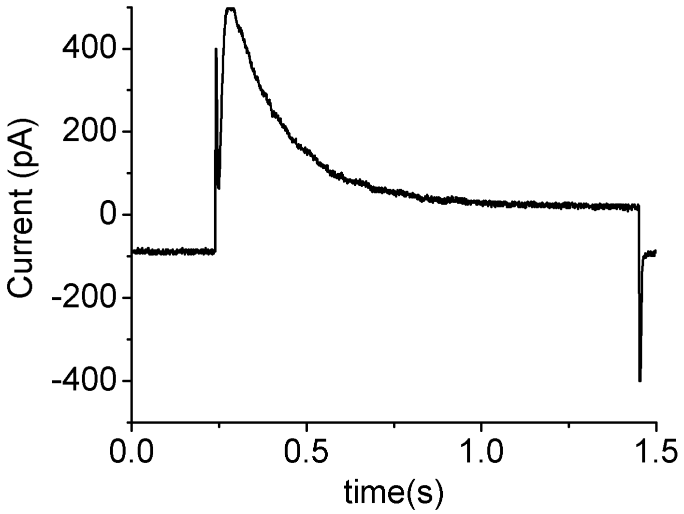

Figure 2.11: Multi channel current trace. The current trace corresponds to about 50 KvAP channels. The channels were kept in the closed state for an extended period of time before stepping the voltage to 60 mV (stepped at 0.25 s). The initial spike is a capacitive transient. The channels open stochastically with a time scale of $\sim$ 30 ms and decay exponentially due to inactivation.

gives the current from channels after correcting for the inactivation process. The graph shown in Fig. 2.12 shows the current trace obtained after correcting for the inactivation process.

As evident from the current trace shown in the Fig. 2.12, the current saturates to a peak value I_{peak} ($\sim$ 650 pA in this case). This current, I_{peak}, is proportional to the membrane potential V, the single channel conductance χ, the number of channels in the bilayer N and the open probability at that voltage $P(V)$.

$$I_{peak} = N \cdot \chi \cdot V \cdot P(V) \tag{2.1}$$

Thus, the opening probability function is measured by obtaining current traces at different potentials and by plotting the normalized $I_{peak}/(N\chi V)$ vs. the membrane potential V. The membrane potential is varied as shown in Fig. 2.13,

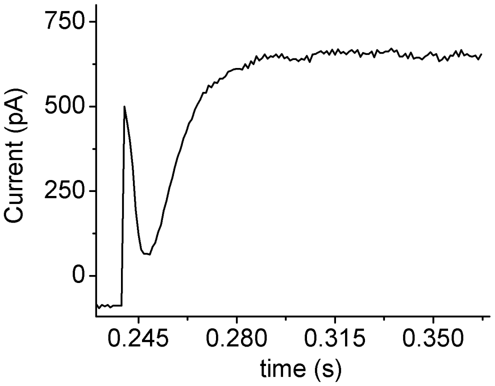

Figure 2.12: Multi channel current trace after correcting for the inactivation. This graph was obtained by using the data in Fig. 2.11. An exponential decay was fitted to the current trace after the peak to determine the inactivation time scale. This inactivation time scale was used to multiply the current trace with an exponential factor to correct for the inactivation.

where the potential is held at -120 mV for 10.8 seconds for the channels to recover fully from inactivation and a 1.2 second pulse at a voltage V to measure the current at that voltage.

An experimentally measured opening probability curve for the KvAP ion channels is shown in Fig. 2.14. It can be inferred from the data that for voltages above 20 mV, the channels are open with probability one whereas for voltages below -40 mV the channels are almost closed. The error bars represent the uncertainty in the measurement that is obtained by recording 20 current traces for each point.

The variation of opening probability with voltage can be modeled as a two states system with the energy difference between the two states being proportional to the membrane voltage difference.

Let the energy difference between the two states be $E_0 + \alpha V$ where E_0 is the energy difference between the two states when the voltage difference is zero and α is a proportionality constant. The fraction of channels in the open state is given

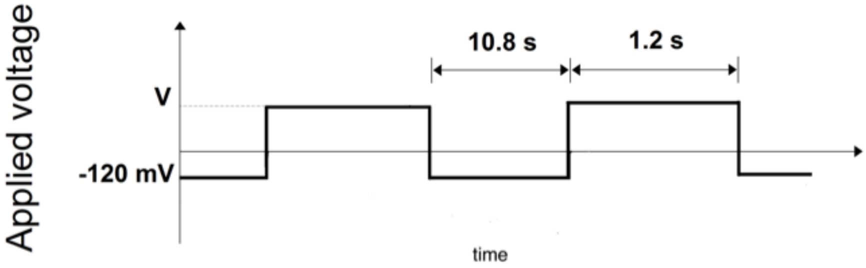

Figure 2.13: The DC voltage pulse protocol used to measure the opening probability. The membrane potential is held at -120 mV for 10.8 seconds to recover channels from inactivation. Then the voltage is stepped to the desired value and sustained for 1.2 seconds.

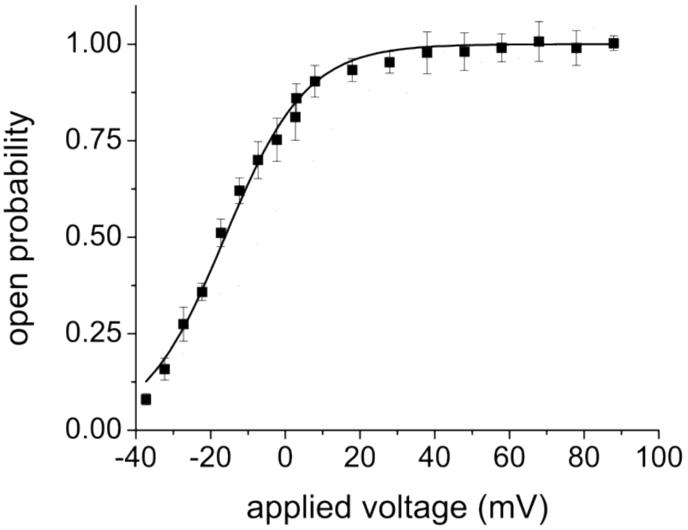

Figure 2.14: The experimentally measured opening probability curve for KvAP. Each point was obtained by averaging 20 data points and all data was from channels in the same bilayer. For voltages close to $\sim$ -40 mV, the channels are almost closed and for voltages above $\sim$ 20 mV, the channels are fully open. The fit is produced from equation 2.3.

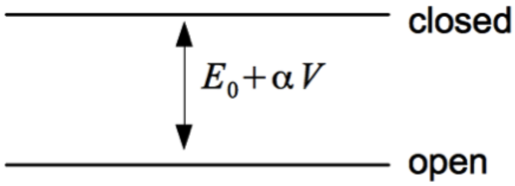

Figure 2.15: A two state system to model the voltage gated ion channel KvAP. The closed state has a higher energy since the channels are mostly open even with no voltage difference. E_0 is the energy difference between the two states without any voltage difference and α is a parameter.

by the Boltzmann factor,

$$P_{open} = \frac{e^{-\text{Energy of open state}/k_BT}}{e^{-\text{Energy of open state}/k_BT} + e^{-\text{Energy of closed state}/k_BT}} \tag{2.2}$$

This expression can be simplified to the form below by plugging for the energy difference between the two states.

$$P_{open} = \frac{1}{1 + e^{-(E_0+\alpha V)/k_BT}} \tag{2.3}$$

This equation for the open probability is used to fit the data in the experimental open probability curve shown in Fig. 2.14 and a good agreement between the model and the experiment can be observed for DC experimental observations.

2.9 Experimental setup for probing voltage gated ion channels with AC voltages

The equivalent circuit model of the lipid bilayer system with the ion channels can be depicted as in Fig. 2.16. The bilayer acts as a capacitor while the ion channels behave as variable resistors. The capacitance of the bilayer is about 50 pF to 100 pF for the lipid bilayers in our experiments. Applying an AC voltage

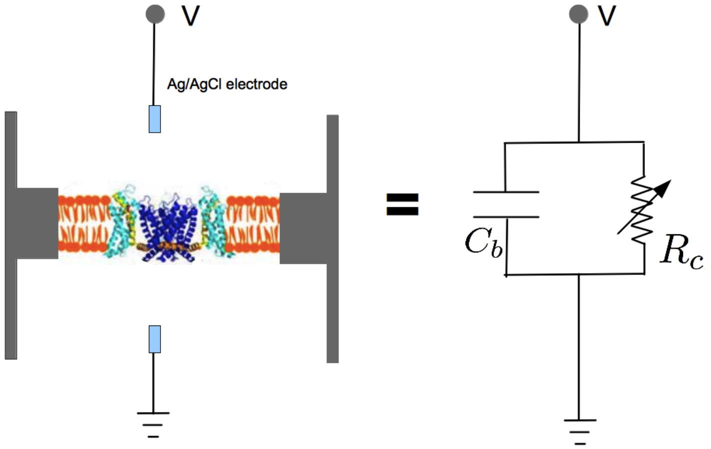

Figure 2.16: The equivalent circuit of a lipid bilayer with ion channels. The bilayer acts as a capacitor while the channels are equivalent to resistors (with a time and voltage dependent resistance).

across these lipid bilayers result in a capacitive current. The magnitude of this current is proportional to the amplitude of the voltage, the frequency of the AC signal and the capacitance of the bilayer.

If the applied voltage is of the form $V(t) = V_0 e^{i\omega t}$ then the capacitive current across the circuit is $I(t) = V_0 \omega C e^{i(\omega t + \pi/2)}$. Thus an applied voltage of 100 mV at 100 Hz across a typical bilayer capacitance of 100 pF results in a capacitive current of about 1 nA. When compared to the single channel conductance of about 10 pA, the capacitive current is much higher. Thus we need to subtract the capacitive contribution from the measured signal before we can analyze the behavior of the channel under oscillatory voltages.

In our experiments, the capacitive current is electronically subtracted by using a matched network. The schematic of the setup is shown in the Fig. 2.17.

In this setup, there are two identical voltage clamp amplifiers (VCAs), both of them are fed with the same command voltage. One of the voltage clamp amplifiers is connected to the actual bilayer setup while the other is connected to a variable

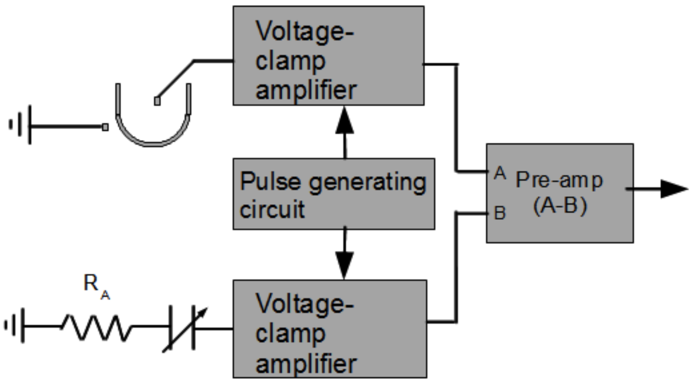
Voltage-clamp amplifier
Pulse generating circuit
Voltage-clamp amplifier
R_A
A
B
Pre-amp (A-B)

Figure 2.17: Electronic scheme to subtract the capacitive current from the bilayer. The command voltage is applied to the actual lipid bilayer used in the experiment. At the same time, the same command voltage is applied to a variable capacitor. Two identical I to V converters convert the resulting currents to voltage levels and a pre amplifier subtracts the voltage signal of the variable capacitor from the lipid bilayer. By matching the variable capacitor to that of the lipid bilayer, the capacitive portion can be subtracted effectively.

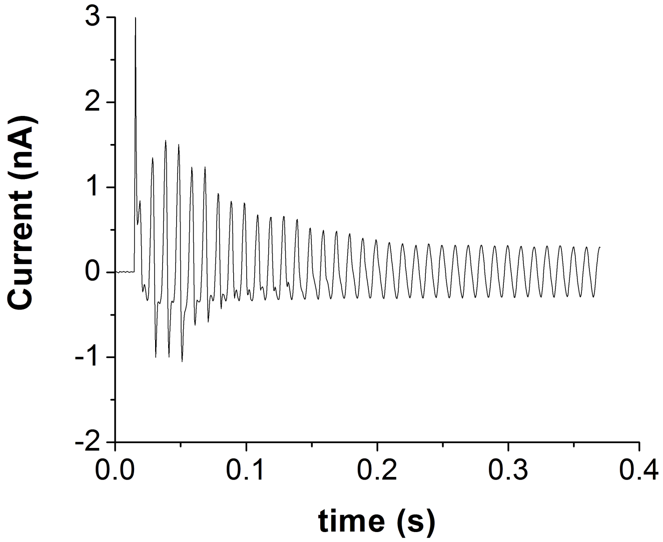

Figure 2.18: Ion channel current before performing the capacitive current cancellation procedure. The initial part of the trace is a mix of the capacitive current and the ion channel current. Ion channels inactivate towards the end of the trace (∼ 0.2 s), showing only the capacitive current.

capacitor and a resistor. The output from both VCAs are fed to a pre amplifier in the A − B mode which subtracts input B from input A.

The procedure to cancel the capacitive current

First the experiment is setup so that channel current can be observed for DC step potentials. After this, an AC signal is applied as the command voltage after hyperpolarizing the channels at −120 mV for 10 seconds. The ac signal used in this step is at an amplitude of 60 mV and frequency of 100 Hz. Fig. 2.18 shows an experimentally recorded current trace from the setup by hyperpolarizing the channels at -120mV for 10 seconds prior to applying the AC voltage.

The applied AC signal was a 60 mV signal at 100 Hz. The shape of the DC ion channel current trace modulates the envelope of the AC current trace.

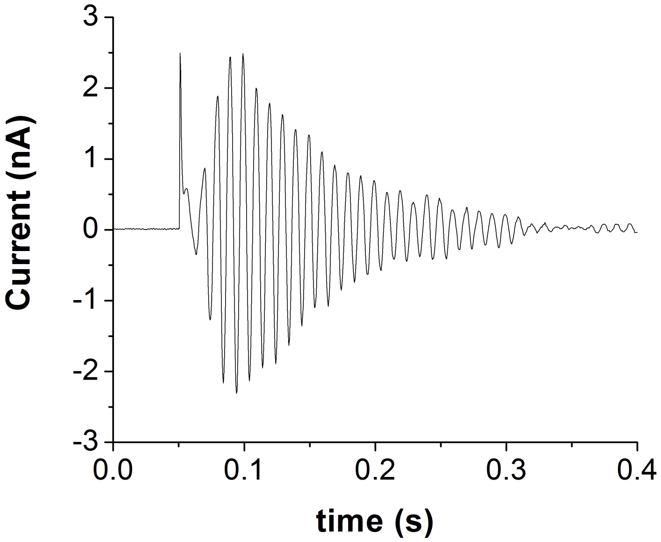

Figure 2.19: Ion channel current after performing the capacitive current cancellation procedure. As shown in Fig. 2.18, only the capacitive current of the bilayer results after channel inactivation. The variable capacitor is tuned to cancel the capacitive current from the lipid bilayer. The fact that the signal falls to zero implies that the capacitive portion of the current has been nulled by this technique.

The initial fast rise is due to activation and the decay is due to inactivation. As evident from the current trace, the final current does not approach zero even though the channels inactivate. The remaining oscillating current that we see is the capacitive current from the bilayer. Now the tunable capacitor of Fig. 2.17 is tuned to cancel out this capacitive current. A reliable capacitive current cancellation can be achieved with the above scheme. The current trace of Fig. 2.19 is obtained after the capacitive current cancellation. It can be observed that after the inactivation of the ion channels, the current falls close to zero.

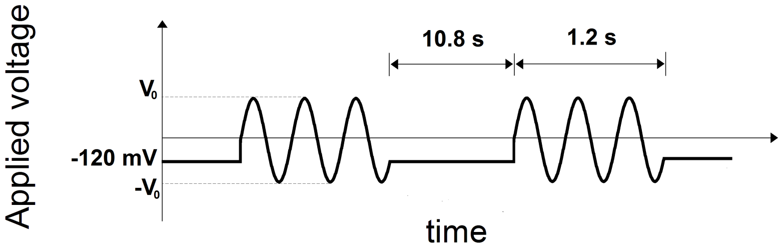

Figure 2.20: Pulse protocol to probe the AC behavior of KvAP.

2.10 The response of KvAP to oscillatory voltages

In order to probe the channels with AC signals, an applied voltage of the form shown in Fig. 2.20 is used. The channels are left in the closed state for 10.8 s after which an AC voltage is applied for 1.2 s. The AC waveform has zero offset and it starts with zero phase.

The current trace of Fig. 2.21 shows the response of KvAP at a relatively low frequency of 5 Hz. The applied sinusoidal voltage (60 mV at 5 Hz) is plotted along with the ionic current. An asymmetry in the current trace can be observed; the positive current peaks are much higher than the negative current peaks. This rectification behavior is a consequence of the opening probability curve. For positive voltages, the channels remain mostly open, producing a large current while the ion channels close for negative voltages. The current trace at an intermediate frequency of 20 Hz is shown in Fig. 2.22 while the current trace at a relatively high frequency of 100 Hz is shown in Fig. 2.23. At 100 Hz, the shape of the DC current trace modulates the envelope of the AC current trace. Channels open stochastically at the beginning and they inactivate after prolonged activation. The new feature in this current trace is that the positive and the negative currents are symmetric.

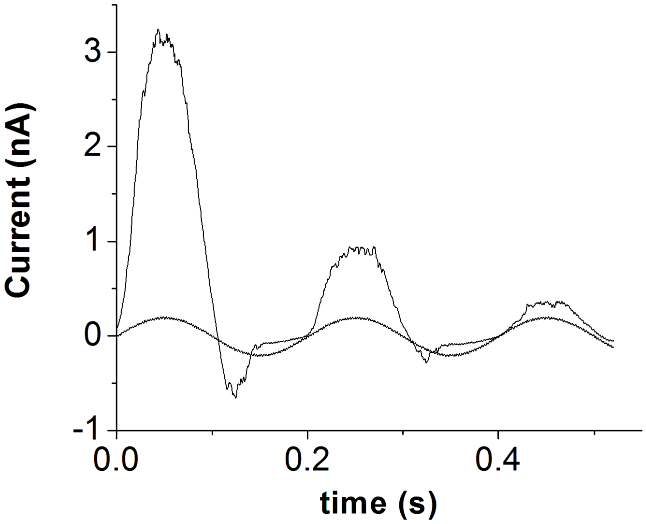

Figure 2.21: Ion channel current at a relatively low frequency of 5 Hz. The ionic current across the channels is plotted along with the applied sinusoidal voltage. An asymmetry between the positive and negative voltage peaks can be observed. This asymmetry is a consequence of the open probability curve.

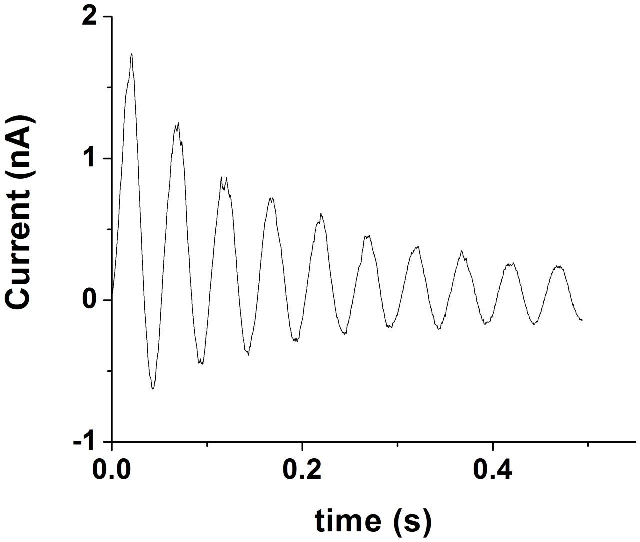

Figure 2.22: Ion channel current at an intermediate frequency of 20 Hz. At this intermediate frequency, the positive and negative peaks are still asymmetric as a consequence of the open probability curve.

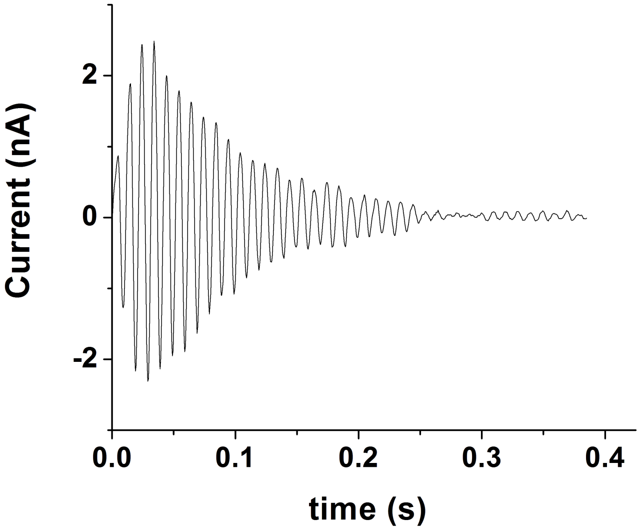

Figure 2.23: Ion channel current at a relatively high frequency of 100 Hz. The envelop of the AC current trace is modulated by the DC current trace. A new feature at this relatively high frequency is the symmetry in the positive and negative current peaks.

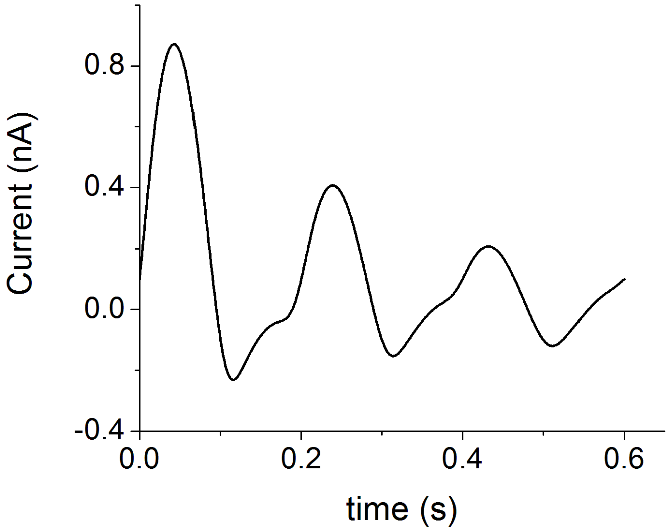

Figure 2.24: Calculated ion channel current for an applied voltage at 5 Hz based on the open probability curve. The current was calculated as $I(t) = N \cdot \chi \cdot P(V(t)) \cdot V(t) \cdot exp(-t/\tau)$ with $V(t) = V_0 \sin(\omega t)$.

We can calculate the ion channel current based on the description of the ion channel in terms of the two states model. In this model, the open probability is given by the instantaneous open probability $P[V(t)]$. The graph in Fig. 2.24 shows the current trace calculated at 5 Hz, using the open probability curve. The current is calculated as $I(t) = N \cdot \chi \cdot V(t) \cdot P[V(t)] \cdot exp(-t/\tau)$, where $N = 100$ is the number of channels, χ =170 pS is the single channel conductance, $V(t)$ is the voltage applied at time t (of the from $V_0 sin(\omega t)$) and τ is the inactivation time scale.

As evident by Fig. 2.21 and Fig. 2.24, the calculated current trace is analogous to the experimentally observed current trace at low frequencies. Fig. 2.25 shows the calculated current trace at 50 Hz. At 50 Hz, the calculated current trace shows an asymmetry between the positive and negative currents, and this asymmetry is in contrast with the experimentally observed current traces (Fig 2.23). Thus, the two states model cannot account for the experimental data at

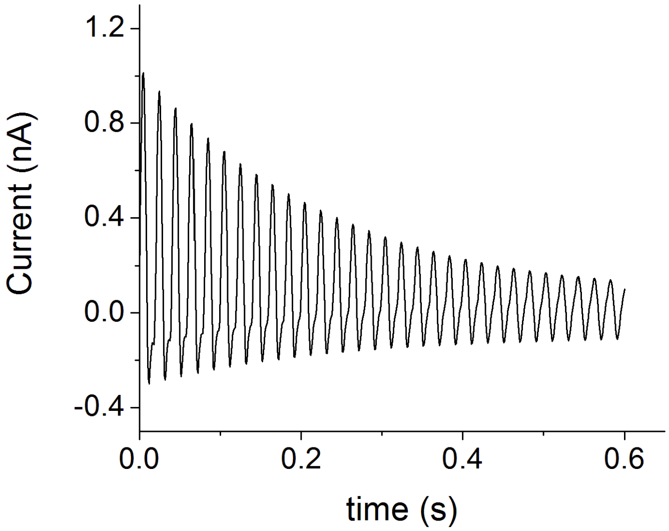

Figure 2.25: Calculated ion channel current for an applied voltage at 50 Hz based on the open probability curve.

relatively high frequencies.

2.10.1 Variation of the ion channel current at different membrane voltages

As shown in Figs. 2.21, 2.22 and 2.23 the measured current traces show a qualitative difference depending on the frequency. In order to investigate the response of the ion channel at different frequencies and voltages, the systematic approach is to measure the response of the channel by varying the applied voltage while keeping the frequency fixed or by measuring the response at fixed voltage while varying the frequency. The first case is discussed in this section while the later is discussed in the next section.

In order to organize the data, two suitable quantities to use from a particular current trace is the positive peak current and the negative peak current. Due to the inherent inactivation of the ion channels, a correction factor must be used before

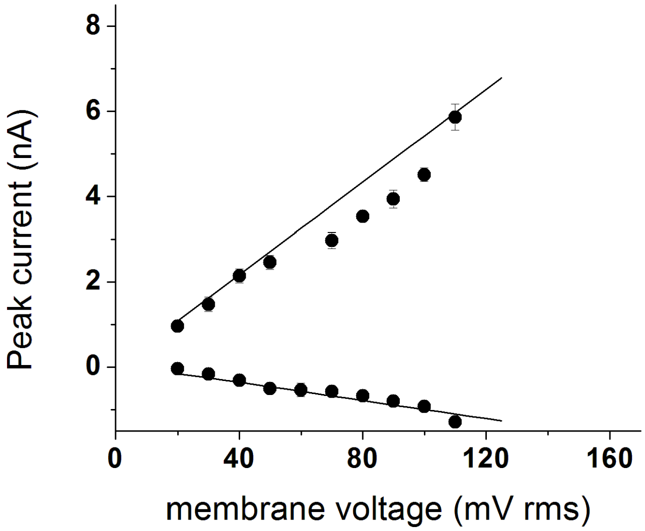

Figure 2.26: The variation of the positive and negative peak currents vs. the applied AC voltage at 5 Hz. The asymmetry of the two branches is due to the opening probability curve.

comparing the positive peak currents from different traces. For example, the peak current could be reduced by different fractions depending on the frequency. Thus, a correction factor, calculated for each current trace is used to correct for the reduction of the peak current due to the inactivation process.

Fig. 2.26 shows the variation of the positive and negative peak currents with the applied potential when the AC signal is at 5 Hz. Each point in Fig. 2.26 is obtained from a curve similar to the one shown in Fig. 2.21. The positive and negative peak currents are measured from a trace and they are multiplied by an exponential factor $e^{(t_{peak}/\tau)}$, where t_{peak} is the time at which the current peak occurs (measured with respect to the beginning of the depolarization pulse) and τ is the inactivation time scale.

The asymmetry of the positive peaks and the negative peaks results from the opening probability curve as discussed before. At an intermediate frequency of 40 Hz, the behavior of the two branches is different as shown in Fig. 2.27. At this

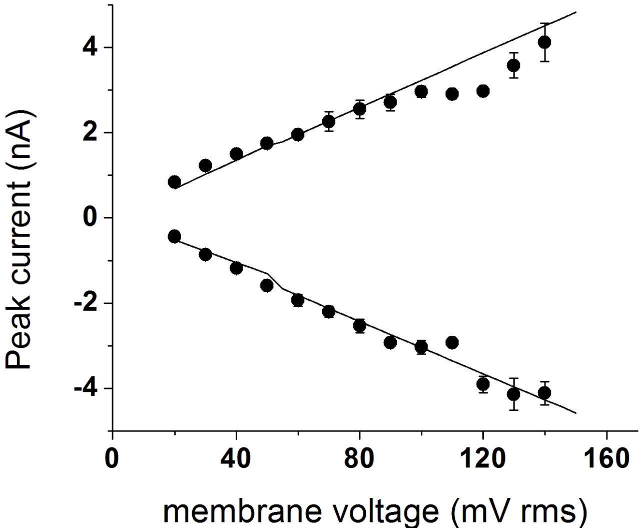

Figure 2.27: The variation of the positive and negative peak currents vs. the applied voltage when the AC voltage is at 40 Hz. At this intermediate frequency, the positive and negative branches appear to be symmetric implying that the channels are only exploring a small region of the opening probability curve.

frequency, the two branches appear to be symmetric. This response is similar to a resistor. At a higher frequency of 100 Hz, a new feature can be seen (Fig. 2.28). The two positive and negative peak currents appear to increase with the applied voltage at the beginning, but the currents saturate and then decrease with the increasing membrane voltage. This is a non-linear effect of the voltage gated ion channel KvAP that was not previously known.

For an ohmic device, an increase in the applied voltage cannot correspond to a decrease in the current. Further, it was verified that this effect was not due to a disruption of the channels. The change in the behavior at different frequencies implies that the frequency response of the channel is not a trivial problem. If the ion channels were to behave similar to a resistor, the ionic current through the channels will be independent of the frequency.

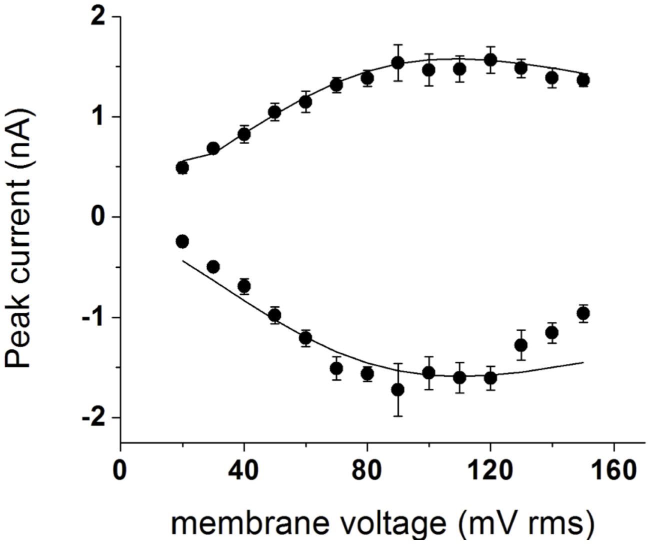

Figure 2.28: The variation of the positive and negative peak currents vs. the applied voltage when the AC voltage is at 100 Hz. A new feature is seen where the ionic current saturates and then decreases for increasing applied voltage.

2.10.2 Frequency response of the ion channel at different membrane potentials

Figure 2.29 shows the frequency response of the channel at two different applied voltages. At the lower voltage of 20 mV, the ionic current from the channels remain independent of the frequency. But, at a higher applied voltage of 70 mV, the ionic current shows a strong dependence on the frequency, where the current drops by ≈ 2.5 times in the frequency range studied. This is a consequence of the non-linearity of the ion channel.

2.11 Continuum mechanics model of the ion channel KvAP

In order to study the non-linearity of the channel that cannot be understood by simply considering the open probability curve, we modeled the channel using continuum mechanics. The trans-membrane electric field couples to the positively

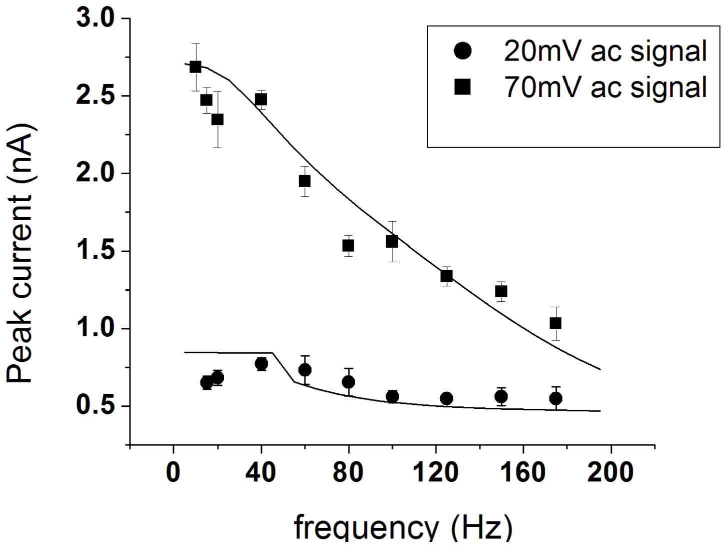

Figure 2.29: The variation of the positive peak current with frequency at fixed amplitude of the applied voltage. Frequency response of the ion channel is different between the two voltages studied.

charged Arginine residues on the S4 helix of the voltage sensing domain of the channel and moves them perpendicular to the membrane. We concentrate on the motion of the Arginine residue in this degree of freedom, i.e. we describe the position of the arginines with a coordinate z orthogonal to the bilayer and write the equation of motion for displacement z. We assume for simplicity that all four arginines move together.

We assume z is a continuous variable, whereas the usual representation of the gating motion is as a two-states system. Both representations are idealizations; the real system has many discrete states. This is seen experimentally from measurements of the charge-voltage (QV) and conductance-voltage (GV) curves [18]. For a two-states system, the two curves should superimpose, but for a real channel they do not. However, a model in terms of several discrete states introduces many parameters, which ultimately limits its predictive power. Here we take the opposite limit of the two-states system, which is infinitely many states.

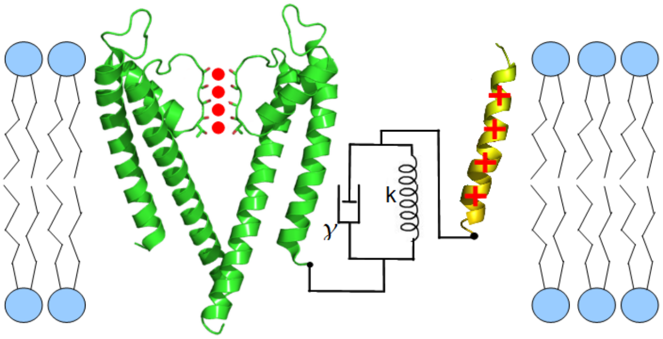

Figure 2.30: Cartoon representation of the continuum mechanical model of the ion channel KvAP to model the AC response. The voltage sensing S4 helix is assumed to move as if it is connected to a damped spring.

We replace all interactions of this voltage sensing domain with other residues of the ion channel by a simple mechanical model; an elastic element and a dissipative element in parallel, or in other words, by a damped spring. This is the simplest mechanical element that was found to agree with the experimentally observed data. This mechanical analogue is depicted in the cartoon representation of Fig. 2.30.

We assume that all four voltage sensing elements moving together. The equation of motion for the voltage sensing domain is

$$\gamma\frac{dz}{dt} + kz = \frac{qV_0}{d}sin(\omega t) \tag{2.4}$$

, where γ is the dissipation coefficient, k is the spring constant, q is the effective number of charges on the S4 helix which moves across the bilayer, d is the thickness of the bilayer, V_0 and ω are the amplitude and the angular frequency of the applied AC voltage across the bilayer, respectively.

The inertial term is dropped from the equation of motion as it is negligible when compared to the other terms and this can be justified as follows. The voltage sensing domain has an amino acid sequence of FRLVRLLRFLRILLIIS. The molar mass of this sequence is about 2.1 KDa, which means that the mass of a single S4 helix is $\approx 3.5 \times 10^{-21}$ g. If we assume that the voltage sensor moves a distance of 1 nm in 1 ms, this gives an upper bound for the acceleration of the VSD at about $5 \times 10^{-4}\mathrm{ms}^{-2}$. The estimate for the inertial term $m\frac{d^2z}{dt^2}$ of the S4 helix is about 10^{-15} pN. If we compare this value to the elastic term, kz, assuming an elastic coefficient of 5 pN/nm (which is a typical value for proteins) and a displacement of 1 nm, the force on the S4 helix is on the order of ~ 1 pN. Thus, we can safely disregard the inertial term.

Another term that we omit is a thermal noise term in the equation of motion. Since our measurement of the channel current is based on an ensemble of about 100 channels, adding a noise term will have a negligible effect. Furthermore, the thermal noise term is small compared to the driving force in the experimental regime as $qV_0 \sim 4e \times 50\mathrm{mV} = 200\mathrm{mV} \ll k_BT = 25\mathrm{mV}$.

The instantaneous ionic current of the channels is proportional to the voltage and the number of open channels (open probability). Thus, the current at time t is given by

$$I(t) = N \cdot p(t) \cdot \chi \cdot V(t) \tag{2.5}$$

, where N is the number of channels, $p(t)$ is the open probability at time t, χ is the single channel conductance and $V(t)$ is the voltage applied across the membrane at time t. We know values for all the terms of the equation 2.5, except for the open probability. In this model, we assume that $p(t)$ is controlled by the instantaneous position of the arginines (by the variable z) through the DC opening probability curve in figure 2.14.

For a DC applied voltage, the displacement z of the arginines is force divided by the spring constant:

$$z = \frac{Force}{k} \tag{2.6}$$

The force in question is the electrostatic force on a charge q (the charge on the voltage sensor domain) when a potential V is applied across the membrane.

$$z = \frac{qE}{k} = \frac{qV}{kd} \tag{2.7}$$

The opening probability function can be approximated as a sigmoidal function given by

$$p(V) = \frac{1}{2}\left[1 + \tanh\left(\frac{V - V_1}{\Delta}\right)\right] \tag{2.8}$$

The values of V_1 and Δ can be determined by fitting the above equation to the open probability curve in Figure 2.14 and we obtain the values $V_1 = -25$ mV and $\Delta = 20$ mV. From equation 2.7, we can obtain $V = \frac{kdz}{q}$. This expression for V can be substituted for V in equation 2.8 to obtain the open probability function in terms of the position of the VSD.

$$p(V) = \frac{1}{2}\left[1 + \tanh\left(\frac{\left(\frac{kd}{q}\right)(z - z_1)}{\Delta}\right)\right] \tag{2.9}$$

where $V_1 = \frac{kdz_1}{q}$. The model consists of solving equation 2.4 to find the position of the voltage sensor domain with time, $z(t)$, using it in equation 2.9 to find the opening probability as a function of time and using this opening probability in equation 2.5 to calculate the current as a function of time.

The solution of equation 2.4 can be written as

$$z(t) = \frac{qV_0}{\gamma d\sqrt{\omega^2 + \omega_0^2}} sin(\omega t - \phi) + Ce^{-\omega_0 t} \tag{2.10}$$

where $\tan(\phi) = \omega/\omega_0$, $\omega_0 = \mathrm{k}/\gamma$, and the constant C is determined by the initial conditions. For $t = 0$, the displacement z should correspond to that of the closed channel, $z = z_0$. By applying this condition to the equation 2.10, the constant C can be obtained as,

$$C = z_0 + \frac{qV_0}{\gamma d\sqrt{\omega^2 + \omega_0^2}} sin(\phi) \tag{2.11}$$

Inserting this solution for $z(t)$ in equation 2.9 for the open probability and using it in equation 2.5 for the current gives the ion channel current for AC voltages.

$$I(t) = \frac{N\chi V_0}{2} \left\{ 1 + tanh \frac{\left[(kd/q)\left(\frac{qV_0}{\gamma d\sqrt{\omega^2+\omega_0^2}} sin(\omega t - \phi) + Ce^{-\omega_0 t} - z_1\right)\right]}{\Delta} \right\} sin(\omega t) \tag{2.12}$$

The expression for $I(t)$ depends on many parameters. In the simulation to calculate channel current, most of these parameters are kept in their known values. The values of these parameters are as follows, $q = 4 \times$ electron charge $= 6.4 \times 10^{-19}$C , χ=170 pS, $N = 100$, $d = 4$ nm, Δ =20 mV and $z_0 = 0.2$ nm. The value of k was set at 20 pN/nm. This value for k was based on the fact that the arginine residues of the voltage sensor domain move by 2 Å (measured by gating charges) for a change in potential of about 50 mV (width of the opening probability curve). By using equation 2.7, $V = \frac{kdz}{q}$, and plugging in ΔV=50 mV, q=4e, d=4 nm and Δz = 1 nm gives the value of k to be 20 pN/nm. The only fitting parameter in the model is the dissipation coefficient γ.

The equation for the AC ion channel current 2.12 can now be used to simulate the current from ion channels when subjected to an AC applied voltage. Fig. 2.31 shows the current trace obtained by this equation at a frequency of 5 Hz. Equation

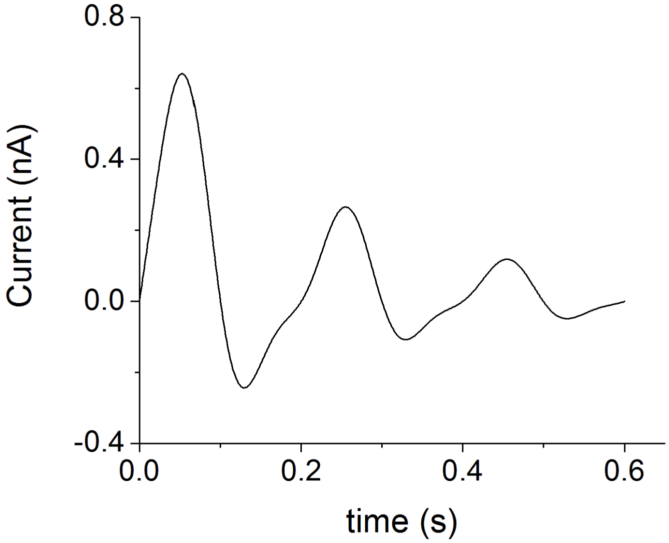

Figure 2.31: Output current of the model at a relatively low frequency of 5 Hz. The same qualitative features can be seen as in the experimental low frequency trace in Fig. 2.21.

2.12 does not account for the inherent inactivation of the ion channels. Thus, the ion channel current shown in figure 2.31 is produced by multiplying the output of equation 2.12 with an exponential decay of time constant of 400 ms. The calculated current trace agrees qualitatively at the low frequency regime.

The model for the channel current given in equation 2.12 can be used to simulate the behavior shown in Figs. 2.26, 2.27, 2.28 and 2.29, which show the ion channel current vs. applied voltage at different frequencies. A MATLAB program was used to fit the data for the experimental data. The algorithm used in this program is shown in Fig. 2.32. A least square regression was performed on the data to determine the value of γ.

This model is a linear model. The only non-linearity of the model is from the opening probability curve. The saturation of current and the eventual decrease with increasing membrane voltage shown in figure 2.28 is another non-linearity which cannot be accounted from the opening probability curve. We attribute this

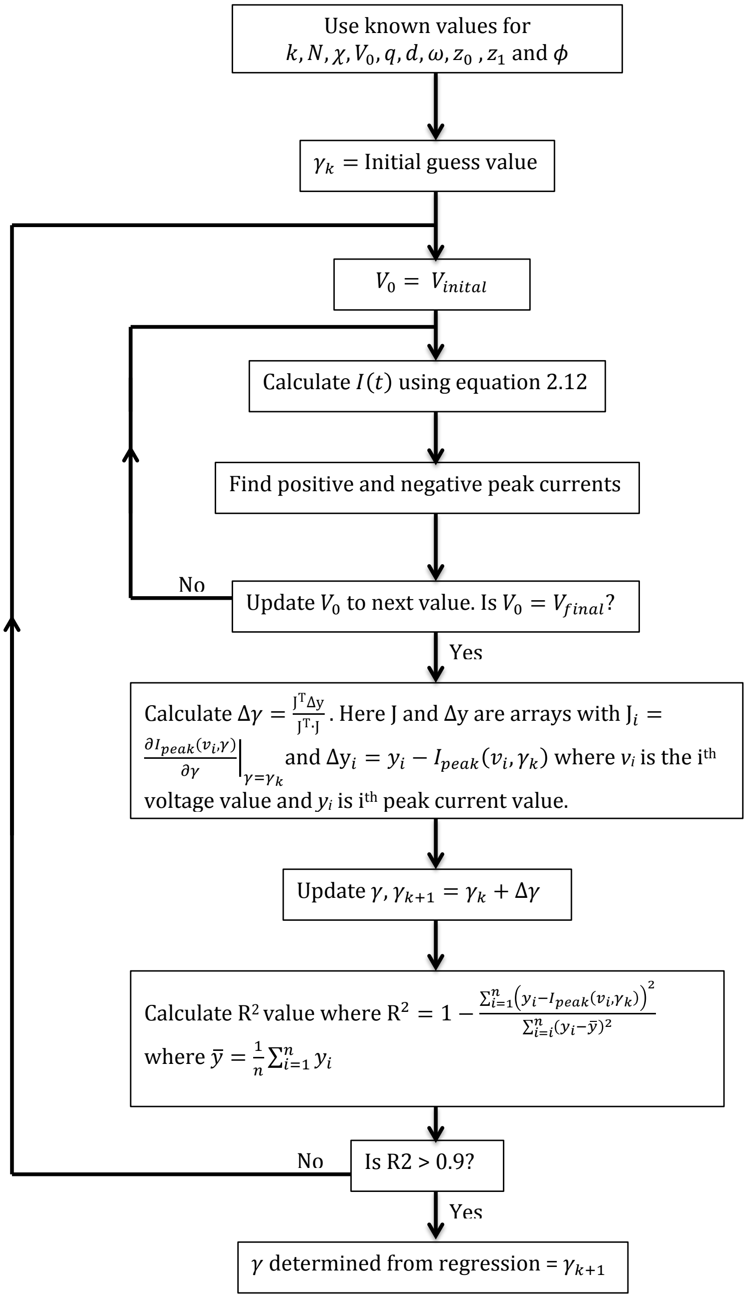
Use known values for
$k, N, \chi, V_0, q, d, \omega, z_0, z_1$ and ϕ
γ_k = Initial guess value
$V_0 = V_{inital}$
Calculate $I(t)$ using equation 2.12
Find positive and negative peak currents
No
Update V_0 to next value. Is $V_0 = V_{final}$?
Yes
Calculate $\Delta\gamma = \frac{\mathrm{J^T \Delta y}}{\mathrm{J^T \cdot J}}$. Here J and Δy are arrays with $\mathrm{J}_i = \left.\frac{\partial I_{peak}(v_i,\gamma)}{\partial\gamma}\right|_{\gamma=\gamma_k}$ and $\Delta \mathrm{y}_i = y_i - I_{peak}(v_i, \gamma_k)$ where v_i is the i^th^ voltage value and y_i is i^th^ peak current value.
Update γ, $\gamma_{k+1} = \gamma_k + \Delta\gamma$
Calculate R^2 value where $\mathrm{R}^2 = 1 - \frac{\sum_{i=1}^{n}\left(y_i - I_{peak}(v_i,\gamma_k)\right)^2}{\sum_{i=i}^{n}(y_i-\bar{y})^2}$
where $\bar{y} = \frac{1}{n}\sum_{i=1}^{n} y_i$
No
Is R2 > 0.9?
Yes
γ determined from regression = γ_{k+1}

Figure 2.32: Algorithm to extract the value of γ from a graph of I_{peak} vs. applied voltage.

effect to a phase lag between the opening of the channel and the applied voltage. For instance, if the applied voltage is at a maximum but the ion channel gate is closed, the ionic current through the channels will be a minimum. The fact that the current saturates and decreases with increasing voltage implies that this phase lag must increase with the membrane voltage.

From our model, the phase lag is given by $\tan(\phi) = \omega\gamma/k$. Thus, the phase lag ϕ increases with the frequency of the applied voltage, but not with the applied voltage itself. In order to account for the effect shown in figure 2.28, a non-linearity was introduced to the dissipation parameter γ, where γ increases with the shear rate. The shear rate in this model is the product of the amplitude of the applied voltage and the AC frequency. In order to explain the observed data, the dissipation parameter had to remain constant below a certain critical shear rate, but γ increased linearly beyond this critical shear rate. This variation of γ with the shear rate is depicted in Fig. 2.33.

The solid line fits in Figs. 2.26, 2.27, 2.28 and 2.29 were produced using the continuum mechanics model described here. The dissipation parameter γ was modeled as shown in equation 2.13, in which γ increased linearly above a critical shear rate σ_c.

$$\gamma = \begin{cases} \gamma_0 & \text{for } \sigma \leq \sigma_c \\ \gamma_0 + \frac{\gamma_1}{\sigma_0}(\sigma - \sigma_c) & \text{for } \sigma > \sigma_c \end{cases} \tag{2.13}$$

The parameters deduced from the data fitting process were γ_0 = 0.2 g/s, γ_1 = 0.54 g/s, σ_0 = 1 Vs^{-1} and σ_c = 2 Vs^{-1}. With these parameters, the value of γ varies from a minimum of $\sim$ 0.2 g/s at low frequency and low forcing amplitude to a maximum of $\sim$ 6 g/s in the opposite limit, within the regime of the experiments.

The behavior of the model can be easily understood qualitatively. At low frequency, the z coordinate is coupled to a simple spring where damping is unim-

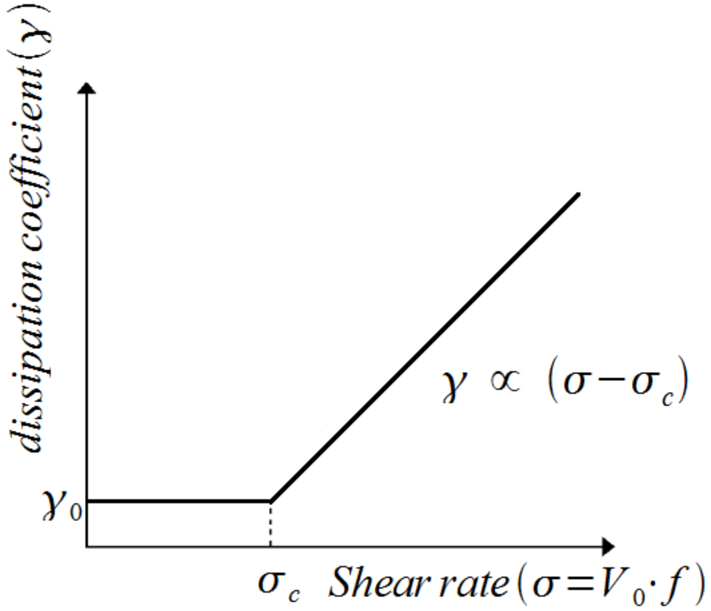

Figure 2.33: Variation of the dissipation parameter γ with the shear rate. The dissipative parameter remained constant below a critical shear rate but increased linearly above this critical shear rate.

portant, so it follows the voltage swings. For the positive voltage swings the channels are mostly open and the current is large, while for the negative swings the channels are mostly closed and the current is small. This is the origin of the asymmetry in the two branches of the graph of Fig. 2.26.

At higher frequencies (Figs. 2.27 and 2.28) damping is important (i.e. the z coordinate is coupled to a damped spring) so the amplitude of oscillations in z is small. This means that the system explores only a small region of the DC opening probability curve (Fig. 2.14) around $V = 0$. Then the number of open channels is roughly constant throughout the cycle, so the current is the same for the positive and negative voltage swings, i.e. the two branches in Fig. 2.27 are symmetric.

At high frequency (Fig. 2.28), as V_0 is increased, eventually $\sigma > \sigma_c$ (Fig. 2.33) and the dissipation coefficient γ starts to increase. This introduces a phase lag between the coordinate z and the applied voltage V which increases with the amplitude of the applied voltage V_0 . The phase lag is $\tan(\phi) = \omega/\omega_0$, where $\omega_0 = \mathrm{k}/\gamma$, so as γ increases ϕ moves from close to zero to close to $\pi/2$. If $\phi = \pi/2$, when the voltage has a peak the channels are mostly closed, and when the channels are mostly open the voltage is $\sim$ zero: so the current is always small. This effect accounts for the surprising observation (Fig. 2.28) that the current saturates and even decreases for increasing V_0 at high frequencies. In a linear system the phase does not depend on the amplitude of the forcing. The only way to obtain this effect is to have a nonlinearity in the system, which here we built on the dissipation coefficient γ (Fig. 2.33).

CHAPTER 3

Mechanical properties of globular proteins measured via nano rheology

In this chapter, a technique to probe the mechanical properties of any globular protein is discussed. The mechanical properties of globular proteins are measured with a nano rheology setup. In this technique, an AC electric field is used to "shake" proteins with an oscillatory force and measure the mechanical motion with sub Angstrom resolution using evanescent wave scattering.

The force on the protein is applied via an electrostatic force. A gold nano particle (GNP) is coupled to one end of the protein and this gold nano particle is functionalized with single stranded DNA to impart a net charge. The protein is tethered to a gold-coated surface from the diametrically opposite end. The application of an electric field forces the charged gold nano particle, which in turn stretches the protein. The resulting deformation of the protein is measured via evanescent wave scattering off the gold nano particles. The scattered light is detected with a photo multiplier tube and amplified via a Lock-in amplifier.

3.1 Theoretical basis of the nano rheology experiment

3.1.1 Evanescent wave scattering from gold nano particles

The deformation of the protein is measured via evanescent wave scattering off gold nano particles. In the experimental setup, a laser beam is steered to hit the interface of a glass prism and a buffer medium (Fig. 3.1). In this case, the laser is travelling in the high refractive index medium (glass) before hitting the lower refractive index medium (water). The critical angle θ_c for total internal reflection is given by,

$$\theta_c = \arcsin\left(\frac{n_w}{n_g}\right) \tag{3.1}$$

and for any incident angle θ greater than θ_c, total internal reflection of the beam occurs at the interface and an evanescent wave is generated at the interface. Application of Snells law to the configuration of Fig. 3.1 gives

$$n_{glass}\sin(\theta) = n_{water}\sin(\theta_r) \tag{3.2}$$

where θ_r is the refracted angle. From [33], the electric field of the refracted beam is given by,

$$E_r(\vec{r},t) = E' e^{ik'(x\sin\theta_r + z\cos\theta_r - \omega t)}. \tag{3.3}$$

where E' is the amplitude of the electric field of the refracted beam and k' is the wave vector inside the buffer medium. From equation 3.2, cos θ_r for $\theta > \theta_c$ is given by,

$$\cos\theta_r = i\sqrt{\left(\frac{\sin\theta}{\sin\theta_c}\right)^2 - 1}. \tag{3.4}$$

Substituting for cos θ_r in equation 3.3 from equation 3.4 gives

$$E_r(\vec{r},t) = E' e^{-k'z\sqrt{\left(\frac{\sin\theta}{\sin\theta_c}\right)^2 - 1}} e^{ik'(x\sin\theta_r - \omega t)} \tag{3.5}$$

The skin depth δ is defined as

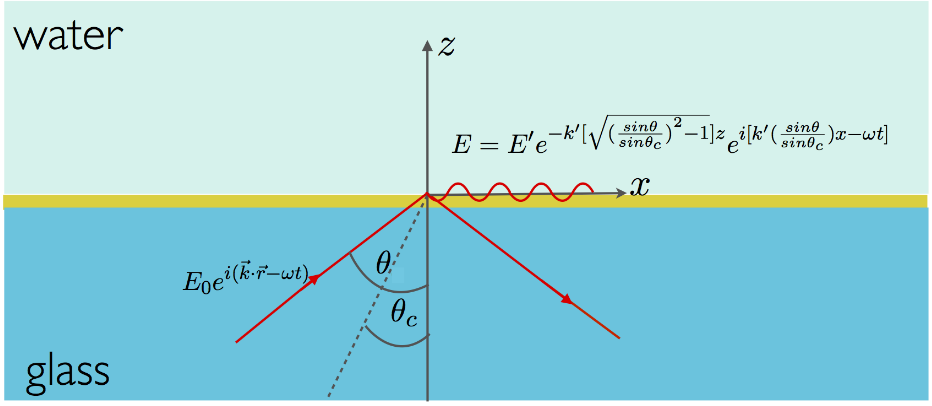
water
z
$E = E'e^{-k'[\sqrt{(\frac{sin\theta}{sin\theta_c})^2-1}]z}e^{i[k'(\frac{sin\theta}{sin\theta_c})x-\omega t]}$
x
$E_0e^{i(\vec{k}\cdot\vec{r}-\omega t)}$
θ
θ_c
glass

Figure 3.1: Evanescent wave in the buffer solution. A laser beam hits the glass-water interface at an angle θ which is higher than the critical angle θ_c for the interface. The evanescent wave in the side of water travels parallel to the interface.

$$\delta^{-1} = k'\sqrt{(\frac{\sin\theta}{\sin\theta_c})^2 - 1} = k\sqrt{\sin^2\theta - \sin^2\theta_c} \tag{3.6}$$

where k is the magnitude of the incident wave vector inside the prism. A gold nano particle in proximity to the interface will scatter the evanescent wave to the far field. The differential scattering cross section of an individual gold nano particle is [33] given by

$$\frac{d\sigma}{d\Omega} = \frac{k'^4}{|4\pi\epsilon_0 E|^2}|\vec{\epsilon^*}\cdot\vec{p} + (\vec{n}\times\vec{\epsilon^*})\cdot\vec{m}/c|^2 \tag{3.7}$$

Here $\vec{m}$ is the magnetic dipole moment of a GNP, $\vec{p}$ is the electric dipole moment of a GNP, $\vec{\epsilon}$ is the polarization of the E field and $\vec{n}$ is the unit vector in the direction of scattered radiation. We can assume that the gold nano particles are perfectly conducting spheres for the scattering process. Thus, the electric dipole moment $\vec{p}$ is given by $\vec{p} = 4\pi\epsilon_0 R^3 E_{inc}$ and the magnetic dipole moment $\vec{m}$ is given by $\vec{m} = -2\pi R^3 H_{inc}$. Substituting these dipole moments to equation 3.7

gives

$$\frac{d\sigma}{d\Omega} = k'^4 R^6 |\vec{\epsilon^*} \cdot \vec{\epsilon_0} - \frac{1}{2}(\vec{n} \times \vec{\epsilon^*}) \cdot (\vec{n_0} \times \vec{\epsilon_0})|^2 \tag{3.8}$$

The vector cross products can be evaluated based on the geometry of the experiment shown in Fig. 3.2. In the experiment, the polarization of the laser beam is along the z-axis. Equation 3.8 can now be simplified to the form

$$\frac{d\sigma}{d\Omega} = \frac{k'^4 R^6}{2}\Big(\sin\theta - \frac{1}{2}\Big)^2 \tag{3.9}$$

Here R is the radius of a GNP. The total intensity of scattered light from a gold nano particle is given by

$$\begin{aligned} I(z) &= \int \frac{d\sigma}{d\Omega} d\Omega \times |E(h)|^2 & (3.10) \\ &= |E(h)|^2 \int \frac{k'^4 R^6}{2}\Big(\sin\theta - \frac{1}{2}\Big)^2 d\Omega & (3.11) \\ &= \frac{|E(h)|^2 k'^4 R^6}{2} \int \Big(\sin\theta - \frac{1}{2}\Big)^2 d\Omega & (3.12) \\ &= 0.8248 |E'|^2 k'^4 R^6 e^{-2\frac{z}{\delta}} & (3.13) \\ &= I_0 e^{-\frac{z}{\delta_e}} & (3.14) \end{aligned}$$

where $I_0 = 0.8248|E'|^2 k'^4 R^6$ and $\delta_e = \delta/2$ is the penetration depth of the evanescent wave in the buffer medium. The penetration depth, δ_e, of the evanescent wave can be calculated using equation 3.6

$$\delta_e = \frac{1}{2k\sqrt{\sin^2\theta - \sin^2\theta_c}} = \frac{\lambda_0}{4\pi\sqrt{(n_g \sin\theta)^2 - (n_w)^2}} \tag{3.15}$$

By plugging in for the incident angle, $\theta \approx 73$, $n_g = 1.5237$, $n_w = 1.3330$ and $\lambda_0 =$ 488 nm, the penetration depth δ_e is found to be around 67 nm. In the experiment,

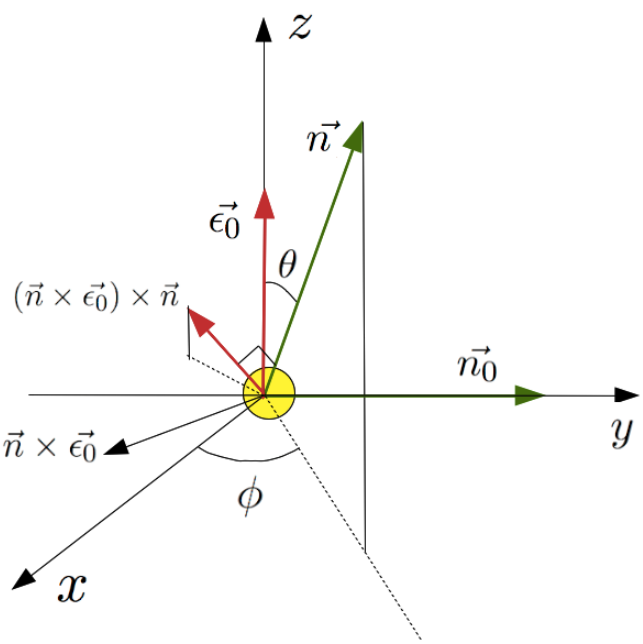

z
$\vec{n}$
$\vec{\epsilon_0}$
θ
$(\vec{n} \times \vec{\epsilon_0}) \times \vec{n}$
$\vec{n_0}$
y
$\vec{n} \times \vec{\epsilon_0}$
ϕ
x

Figure 3.2: Scattering of the evanescent wave from gold nano particles. ϵ_0 is the polarization of the incident beam travelling along the $\vec{n_0}$ direction which polarizes the gold nano particle. We are interested in calculating the radiation scattered in the direction given by vector $\vec{n}$.

the protein deforms a few angstroms in the most. Thus, when compared to the penetration depth, the oscillation is very small and this allows us to linearize the intensity fluctuations as a function of oscillation amplitude. The change in intensity ΔI corresponding to a change in height Δz of the gold nano particle is

$$\Delta I = I(z) - I(z + \Delta z) = I_0 e^{-z/\delta_e}\left(1 - e^{-\Delta z/\delta_e}\right) \approx I(z)\Delta z/\delta_e \tag{3.16}$$

Thus, the amplitude of oscillation of the gold nano particle, Δz is equal to

$$\Delta z = \frac{\Delta I}{I(z)} \cdot \delta_e \tag{3.17}$$

Here, $I(z)$ is the overall intensity of light scattered from the gold nano particles measured without applying an oscillatory force. ΔI is the fluctuation of the intensity of light measured while an oscillatory force is applied on the gold nano particle−protein system. In the experiment, the fluctuation of intensity is measured accurately via phase locked detection with a lock in amplifier. In the actual experiment, the intensity of light is measured from an ensemble of gold nano particles (estimated to be around 10^7). Thus, the theoretical resolution of the experiment is

$$\text{resolution} \sim \frac{\text{thermal motion of a single GNP}}{\sqrt{N}} \tag{3.18}$$

where N is the number of gold nano particles from which light is collected for the measurement. Thus, with $N \sim 10^7$, sub angstrom resolution can be achieved.

3.1.2 The force on gold nano particles in the experimental setup

The force on a gold nano particle in the setup is given by, $F = Q \times E$ where Q is the charge on the gold nano particle and E is the electric field. In a parallel plate capacitor with a solid-state dielectric, the electric field is simply the potential difference V across the plates divided by the plate separation d ($E = V/d$). In the experimental setup discussed here, the dielectric medium in question is a buffer solution with mobile ionic species. Due to charge screening effects and an electric double layer at the interface, the calculation of the electric field is not straightforward. The following descriptions can be used to understand the electric double layer at the interface.

Helmholtz model of double layer

This is the simplest approximation of an electric double layer in which the surface charge is neutralized by opposite sign counter ions placed at a distance of d away from the surface. The surface potential linearly decreases from the surface to the counter ions. The distance d is equal to the radius of the counter ions.

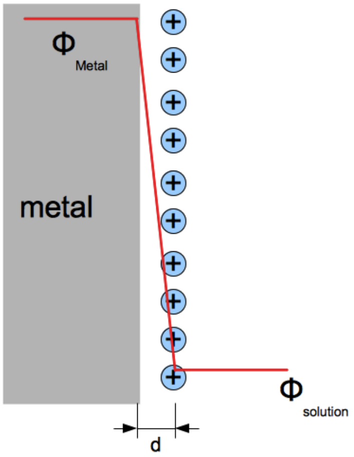

Figure 3.3: The Helmholtz model of an electric double layer. The surface charge of the metal is neutralized with counter ions in the solution, a distance d away from the surface.

Gouy diffuse layer model of double layer

In this model of the double layer, the mobile charges are distributed according to the Boltzmann distribution. Assume that there are N different species of ions in the solution with the i^{th} species having a valancy of z_i. The concentration of the i^{th} species, $c_i(x)$, is governed by the Boltzmann distribution and is given by the expression

$$c_i(x) = c_i^0 exp\Big(- \frac{z_i F \Phi(x)}{RT} \Big) \tag{3.19}$$

where F is the Faraday constant, R is the universal gas constant, T is the temperature, c_i^0 is the bulk concentration of species i and $\Phi(x)$ is the electric potential at position x. The potential at a point distance x, $\Phi(x)$, is given by Poisson's equation (Equation 3.20).

$$\frac{d^2\Phi(x)}{dx^2} = -\frac{1}{\epsilon} \sum_{i=1}^{n} z_i F c_i(x) \tag{3.20}$$

ϵ is the permittivity of the buffer solution. Combining equations 3.19 and 3.20 gives the Poisson-Boltzmann distribution of the ionic species as

$$\frac{d^2\Phi(x)}{dx^2} = -\frac{1}{\epsilon}\sum_{i=1}^{n} z_i F c_i^0 exp\Big(-\frac{z_i F\Phi(x)}{RT}\Big) \tag{3.21}$$

The buffer solution used in the experiment can be regarded as composed of two symmetric ion species. Thus, equation 3.21 reduces to

$$\frac{d^2\Phi(x)}{dx^2} = -\frac{1}{\epsilon}Fc_0\Big[exp\Big(-\frac{F\Phi(x)}{RT}\Big) - exp\Big(\frac{F\Phi(x)}{RT}\Big)\Big] \tag{3.22}$$

where c_0 is the bulk concentration of Na^+ or Cl^- ions. The solution of equation 3.22 with the appropriate boundary conditions can be written as

$$\frac{\tanh(F\Phi(x)/4RT)}{\tanh(F\Phi_M/4RT)} = exp(-x/\lambda) \tag{3.23}$$

where Φ_M is the potential of the metal surface and λ is the Debye length given by

$$\lambda = \sqrt{\Big(\frac{\epsilon RT}{2c_0F^2}\Big)} \tag{3.24}$$

Equation 3.23 can be simplified to the familiar form after linearizing tanh to give $\Phi(x) = \Phi_0 e^{-x/\lambda}$. Thus the electric field decreases exponentially away from the surface in a length scale corresponding to the Debye length. The Debye length λ in the experiment is around 1.3 nm (Equation 3.24 with $c_0 = 55$ mM).

Thus, an accurate estimation of the electric field is not simple as the field varies considerably in the working distance of 5 nm to 10 nm.

3.2 Sample preparation

The enzyme Guanylate kinase from Mycobacterium tuberculosis was used in this study [34]. It is a globular protein of molecular weight 22 KDa and catalyzes the conversion of Guanosine mono phosphate (GMP) to Guanosine diphosphate (GDP) by transferring a phosphate group from ATP. Mutagenesis was used to modify the wild type Guanylate kinase gene to substitute Cysteine residues for

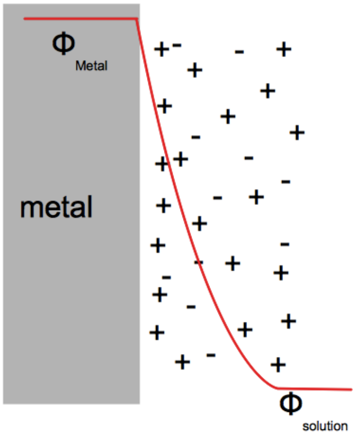

Figure 3.4: The Gouy diffuse layer model of an electric double layer. The ions in the solution obey a Boltzmann distribution. Electric field decreases exponentially from the metal surface within ∼1 nm.

the locations 75 and 171. The Cysteine substitutions were performed in order to covalently couple the enzyme to gold surfaces.

3.2.1 Preparation of the protein sample

Guanylate kinase has two internal cysteines at locations 40 and 193 and site directed mutagenesis was used to convert these cysteine residues to a serines. The coupling of the enzyme to Au surfaces was achieved via thiol groups in cysteine residues. Thus, site directed mutagenesis was used to mutate sites threonine 75 (T75) and arginine 171 (R171) to cysteine residues. All mutagenesis steps were performed with the QuickChange Multi Site Directed Mutagenesis Kit (Agilent). The primer sequences for mutagenesis was obtained from IDT DNA (Coralville, IA) and the accuracy of the mutagenesis products were verified at the UCLA GenoSeq laboratory by gene sequencing. The protocol for protein expression was the same procedure described earlier in subsection Expression of KvAP (section 2.3.4) but the protein purification was different as Guanylate kinase is a native protein (whereas KvAP is a membrane protein).

Purification of Guanylate kinase

The hexa His tag [31] was genetically added to the GK amino acid sequence to aid in the protein purification procedure. Metal affinity chromatography [30] was used similar to the case of KvAP, but Ni beads were utilized instead of Co beads. The buffers used for the purification of Guanylate kinase are listed in table 3.1.

Cell Lysis

- The Lysis buffer was prepared as shown in Table 3.1. The components Lysozyme powder, Protease inhibitor cocktail, DNase and β-Mercaptoethanol were added freshly to the buffer.

- The frozen cell pellet (at $-20\,^{\circ}\mathrm{C}$) was thawed in ice for about 15 minutes and the Lysis buffer was added to the cell pellet (50 mL of Lysis buffer for 4 L cell expression). The solution was put on an orbital shaker to form a homogeneously mixed solution free of cell aggregates.

- The mixture was passed through an Avestin homogenizer (Avestin Emulsiflex C3) to perform cell lysis. The operating pressure was at 10000 psi and the mixture was passed a total of three times through the machine.

- The lysed cell solution was centrifuged at 15000 rpm for 30 minutes to separate the cell debris and the supernatant. The supernatant was handled in an ice bucket during protein purification.

Protein Purification

- A gravity flow column was setup (with a filter) to perform protein purification. About 2 mL of Ni-NTA resin was added to the column and washed

	Stock solution	Amount	Final Concentration
Wash buffer	500 mM Sodium Phosphate pH 8.0	5.0 mL	100 mM
	1 M NaCl	2.0 mL	20 mM
	1.0 M Imidazole pH 8.0	1.0 mL	20 mM
	DI water	41.5 mL	
Lysis buffer	500 mM Sodium Phosphate pH 8.0	5.0 mL	100 mM
	1 M NaCl	5.0 mL	50 mM
	DI water	35 mL	
	Lysozyme powder	10 mg	0.2 mg/mL
	Protease inhibitor cocktail	1 tablet	
	DNase 10 mg/mL	10 μL	2 μg/mL
	14 M β-Mercaptoethanol	7.4 μL	2.0 mM
Elution wash buffer	500 mM Sodium Phosphate pH 8.0	5.0 mL	100 mM
	1 M NaCl	2.0 mL	20 mM
	1.0 M Imidazole pH 8.0	20 mL	400 mM
	DI water	22.5 mL	
Elution buffer	500 mM Sodium Phosphate pH 8.0	5.0 mL	100 mM
	1 M NaCl	2.0 mL	20 mM
	1.0 M Imidazole pH 8.0	20 mL	400 mM
	DI water	22.5 mL	

Table 3.1: Preparation of Guanylate kinase purification buffers.

with 20 mL of Wash buffer.

- The Ni-NTA beads were added to the protein supernatant and were kept at 4 °C for 1 hour with a gentle rotation to keep the beads uniformly dispersed.
- After the 1-hour incubation, the mixture was passed through the gravity flow column for a total of 4 times in order to collect all the beads in the column.
- The beads were then washed with 30 mL of Wash buffer and then with 15 mL of Elution wash buffer.
- Protein was eluted with 10 mL of Elution buffer. The Elution buffer was added 1 mL at a time to maximize the recovery of the bound protein.
- Protein concentration was determined via the Bradford assay. The purified protein was stored at 4 °C till later use.

3.2.2 Preparation of gold-coated glass slides

Glass slides were coated with gold to function as electrodes for the parallel plate capacitor arrangement and to attach the protein via thiol bonds. Proteins were attached on a gold-coated microscope slide (1 inch by 3 inch, 1 mm thick) and a gold-coated glass cover slip ($\sim$ 120 μm thickness) was used as the ground electrode.

The glass slides must be thoroughly cleaned before the metal coating. The slides were first sonicated in DI water for 15 minutes followed by sonication in acetone for another 15 minutes. Then the slides were kept in hot ($\sim$ 80 °C) piranha solution (5:1 concentrated H_2SO_4 to H_2O_2) for 30 minutes to remove all organic material from the surface of slides. After that, the slides were thoroughly washed with DI water to remove piranah followed by an acetone wash. The cleaned slides were dried using a pure nitrogen flow before the metal evaporation.

An e-beam evaporator (CHA Mark 40) at the UCLA Nano electronics Research Facility was used for the deposition of the metals. An adhesion layer of Cr was first coated on the slide followed by the Au layer. The thickness of the Cr layer was 3 nm and was coated at a rate of 0.2 Å/s. Thickness of the Au layer was 30 nm and it was coated at 0.5 Å/s. Following the evaporation process, the slides were stored in acetone for later use.

3.2.3 Coupling enzymes to the gold coated slide

The coupling of the enzyme to the gold-coated microscope slide was achieved by applying a solution of the protein directly on the slide ($\sim$ 1 mL). The protein solution in Elution buffer was first diluted to 1 μM in 1 M KH_2PO_4 at pH 7.0. Then an aqua barrier pen was used to draw a rectangular boundary on the Au coated slide to contain the protein solution in a confined region. The protein solution was then incubated overnight at room temperature. The incubation is performed in a humid environment to prevent the evaporation of the protein solution deposited on the Au slide.

3.2.4 Coupling gold nano particles to the enzyme

After coupling of the protein to the Au surface, the excess proteins were washed with DI water. The washing was performed such that the protein-tethered surface was not exposed to air at any moment. Coupling of gold nano particles to the tethered proteins was achieved by applying a solution of citrate stabilized gold nano particles (20 nm size, Nanocs) in DI water to the protein-tethered surface. The gold nano particle solution was incubated on the Au coated glass slide for about $\sim$ 80 minutes. The excess gold nano particles were removed by washing with DI water. The coupling of gold nano particles produces a visible red color on the Au coated microscope slide. An SEM image of tethered gold nano particles is

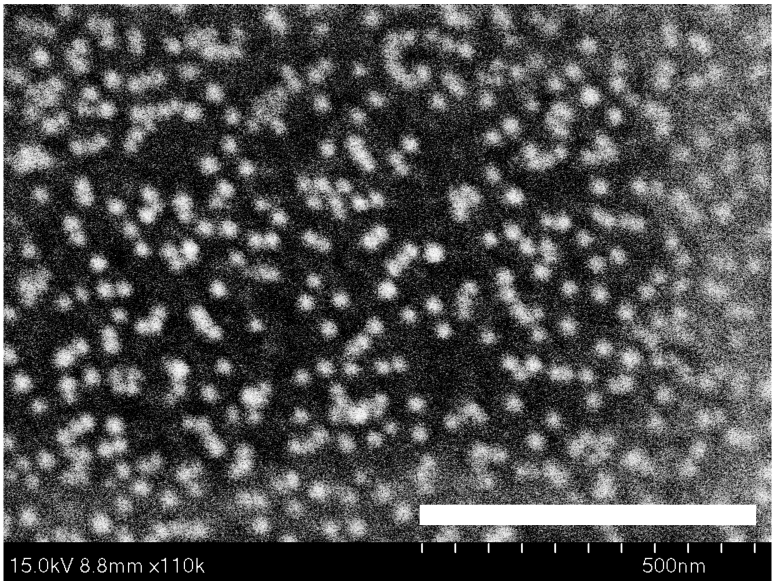

Figure 3.5: Gold nano particles tethered to the substrate via the enzyme Guanylate kinase. The scale bar is 500 nm.

shown in Fig. 3.5. The number density of gold nano particles was estimated to be around 500 particles/μm^2.

3.2.5 Functionalizing the gold nano particles with DNA

Gold nano particles were functionalized with single stranded DNA in order to impart a net charge on them. A single stranded DNA oligomer with the sequence 5' - /5ThioMC6-D/ AAA AAA AAA AAA AAA AAA AAC GCA TTC AGG T -3' was used for the functionalization and this oligomer contains a 5' thiol modification. The DNA was diluted in 1 M KH_2PO_4 at pH 4.0 to a concentration of 1 μM and was added on the protein-tethered slide. The DNA solution was incubated on the slide overnight before the removal of excess DNA with a DI water wash. After washing away excess DNA, the buffer on the protein-tethered slide was changed to SSC/3 (Saline Sodium Citrate diluted by 3 times).

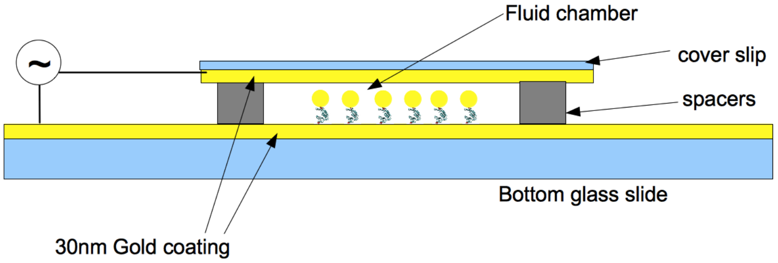

Figure 3.6: Construction of the parallel plate capacitor fluid chamber. The plastic spacer strips were glued to the slides using the epoxy Loctite 608^{TM}.

3.2.6 Preparation of the sample chamber

The nano rheology experiment was performed by applying an AC electric field on the gold nano particles and this was achieved by the electric field from a parallel plate capacitor arrangement. The parallel plate capacitor was constructed with the protein-tethered slide as one electrode and another gold-coated glass cover slip as the 2^{nd} electrode (Fig. 3.6). These slides were separated by 100 μm spacers glued on to the slides and thin wires were soldered on to the two Au coated slides to create the electrical connections. Fig. 3.7 shows picture of a constructed sample chamber used in the experiments.

3.3 The experimental nano rheology setup and method

The experimental setup to perform nano rheology on protein molecules is shown in Fig. 3.8. The fluid chamber constructed as indicated in the previous section is optically coupled to a prism as shown in Fig. 3.8 with index-matched oil. A 488 nm laser beam is steered through the prism such that the beam undergoes total internal reflection at the face coupled to the fluid chamber. A 60X microscope objective is focused on to the resulting light spot on the protein tethered slide. The focusing of the microscope on to the protein-tethered slide can be assisted by

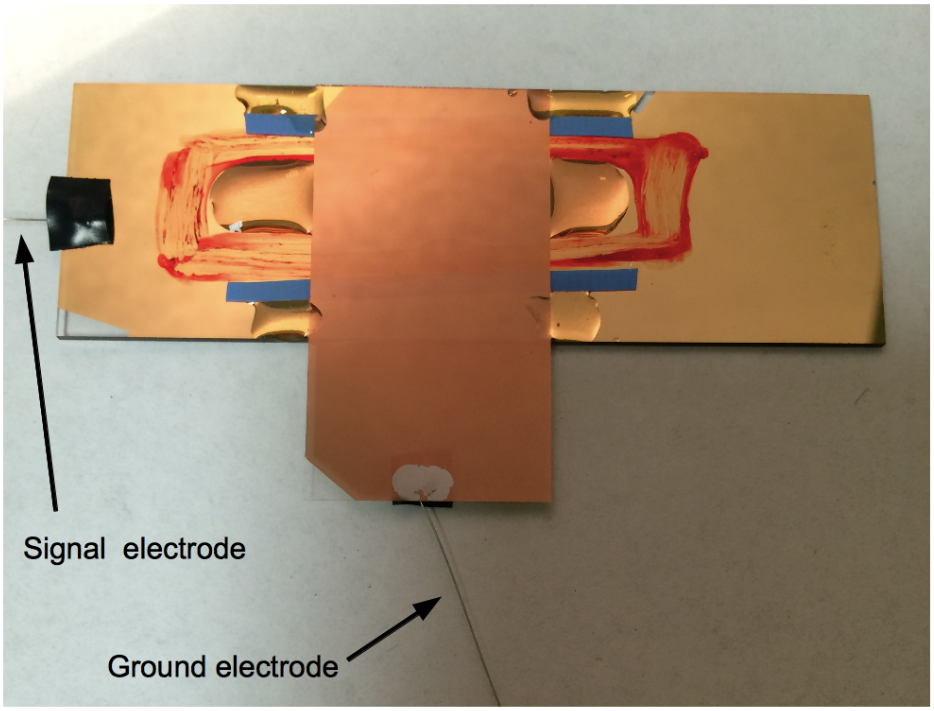
Signal electrode
Ground electrode

Figure 3.7: An image of a fluid chamber used in the nano rheology experiment. The red rectangle marked on the base glass slide is the hydrophobic barrier that holds the buffer in. The two slides combined have a transparency of about 8%.

scratch marks on the gold-coated slide.

Once focusing of the microscope is achieved, the light from the objective is diverted to a photo multiplier tube (Hamamatsu photonics) and a homebuilt current to voltage converter is used to convert the current output of the photomultiplier tube to a voltage signal. The AC voltage to apply a force on the gold nano particles is provided by the reference output of the lock-in amplifier. The reference output of the lock-in amplifier is connected to the fluid chamber via the thin wires soldered on to the Au coated slides (Fig. 3.7). The lock in amplifier is connected to the computer via a GPIB interface that provides full controllability of the lock-in amplifier functions via a custom written software to streamline data acquisition.

The impedance of the fluid chamber (which acts similar to a capacitance) decreases with increasing frequency of the AC excitation voltage and this decrease in impedance could result in a decrease of the actual voltage across the fluid chamber. In order to correct for this effect, the actual voltage difference across the fluid chamber is measured via a data acquisition unit, and the reference output voltage is corrected so that the desired voltage difference appears across the fluid chamber.

The software can either keep the force on the gold nano particles constant (fixed reference output voltage) and perform a frequency sweep or keep the frequency of the output voltage fixed and perform a voltage sweep. For each measurement point, a voltage V is applied at the frequency ω for 100 seconds and the resulting output voltage from the lock-in amplifier is averaged over this 100 seconds interval to perform the measurement. In order to measure the overall intensity of light scattered from the gold nano particles, the output voltage from the lock-in amplifier is set to zero, and a mechanical chopper is placed between the laser and the prism. The optical chopper is driven at 200 Hz and the overall intensity is measured for 10 minutes.

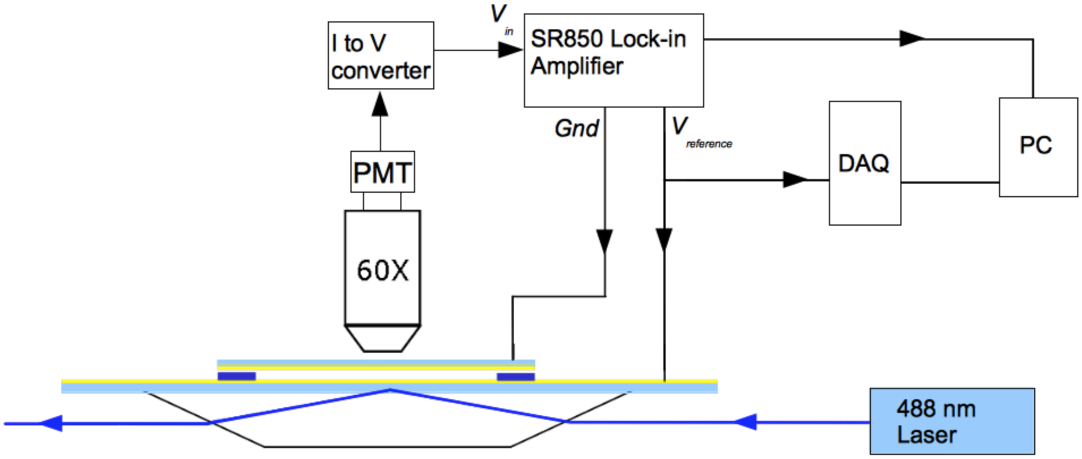
I to V converter
V_{in}
SR850 Lock-in Amplifier
Gnd
$V_{reference}$
DAQ
PC
PMT
60X
488 nm Laser

Figure 3.8: Experimental setup to perform nano rheology on proteins. The fluid chamber is optically coupled to a prism with index-matched oil and a 488 nm laser is steered through the prism to produce an evanescent wave inside the fluid chamber. The fluid chamber is driven with the reference output voltage of the Lock-in amplifier. Scattered light from the GNPs is detected with a photo multiplier tube.

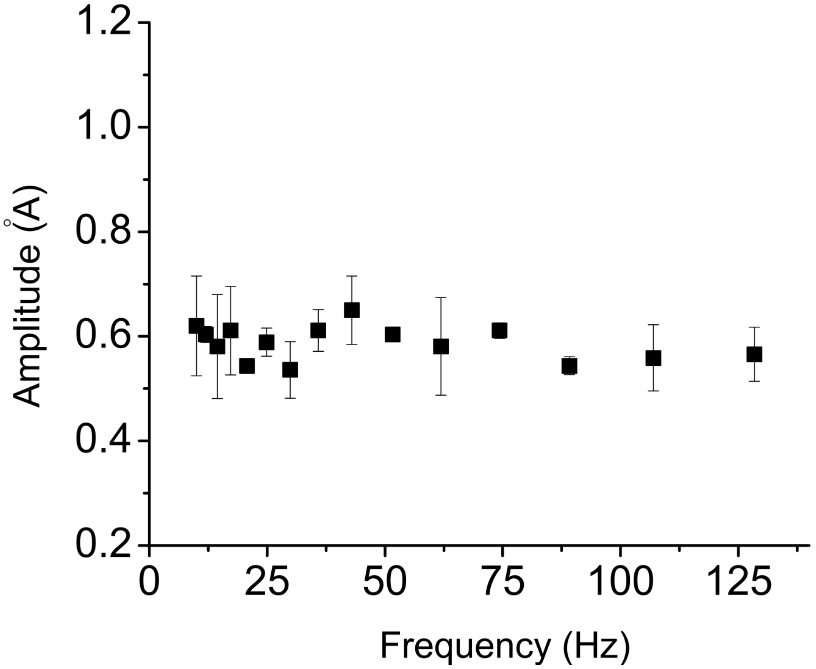

Figure 3.9: Frequency response of Guanylate kinase measured at a fixed amplitude of forcing of 125 mV. Apart from the small fluctuation, the value essentially remains fixed around 0.6 Å regardless of the frequency of the force.

3.4 Mechanical response of the enzyme Guanylate Kinase

In this section, I will outline the results of the AC mechanical deformation experiments performed on the enzyme Guanylate kinase using the nano rheology experiment described in the previous section. Fig. 3.9 shows the frequency response of the protein at a relatively low voltage of 125 mV. The amplitude of oscillation is around 0.6 Å and this value remains essentially independent of the frequency of the applied voltage.

Fig. 3.10 shows the frequency response of the protein at a relatively high voltage of 250 mV. At this forcing amplitude, the response shows a different behavior than at the lower forcing response shown in Fig. 3.9. In the response curve shown in Fig. 3.10, the amplitude of deformation of the protein scales as

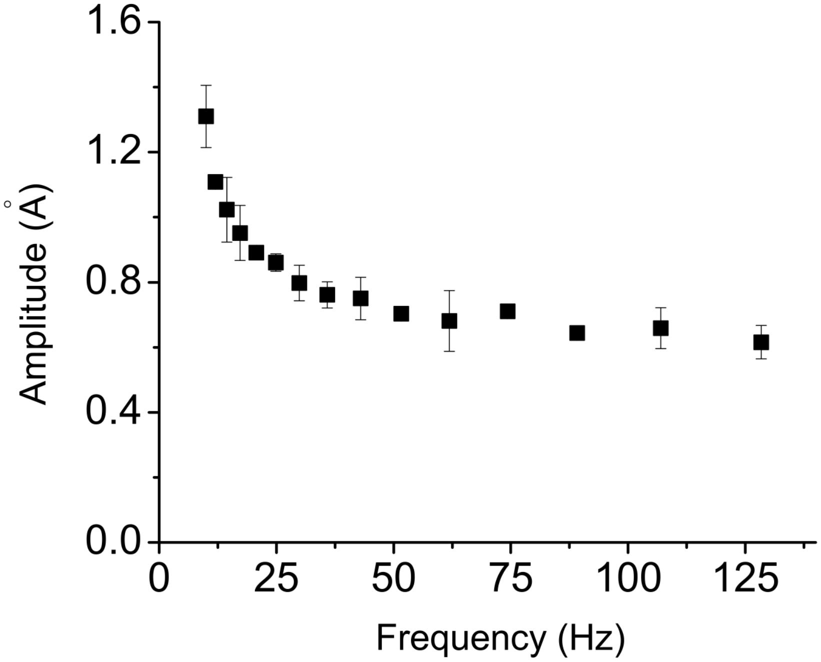

Figure 3.10: Frequency response of Guanylate kinase measured at a fixed amplitude of forcing of 250 mV. At this relatively high applied forcing, the response is qualitatively different from the response in Fig. 3.9. The response diverges as $1/\omega$ towards the low frequency end, while the response flattens at the high frequency limit.

$1/\omega$ for low frequencies while at higher frequencies, the response amplitude flattens and is independent of the frequency. This change in the frequency response curve is a reversible process, lowering the amplitude of forcing can reproduce the original flat response shown in Fig. 3.9.

3.4.1 Interpretation of the results

At low enough forcing, any soft matter system shows linear elasticity. In an elastic response, the amplitude of response is independent of the frequency of forcing. In the experiment, the force on the gold nano particles could be represented as

$f = f_0 exp(-i\omega t)$. If the protein responds elastically in this force regime, the deformation z of the protein is $z = f_0/k \cdot exp(-i\omega t)$ where k is the elastic constant of the protein. Thus, we can justify that the response we see in Fig. 3.9 is the protein behaving elastically. At higher applied voltages, the response deviates from the linear response where the deformation z scales as $1/\omega$ for low frequencies.

$$z \sim \frac{1}{\omega} \tag{3.25}$$

thus, z can be written as an oscillatory function with an ω dependent amplitude,

$$z(t) = \frac{A}{\omega} exp - (i\omega t + \phi) \tag{3.26}$$

where ϕ is a phase factor. A response of a dissipative element is given by $f = \gamma \dot{z}$ where γ is the dissipation coefficient. Thus, for a force of $f = f_0 exp(-i\omega t)$, the deformation is given by,

$$z(t) = \frac{1}{\gamma} \int f \cdot dt \tag{3.27}$$

$$z(t) = \frac{f_0}{\gamma} \int exp(-i\omega t) \cdot dt \tag{3.28}$$

which gives the relation

$$z(t) = \frac{f_0}{\gamma} exp(-i\omega t + \pi/2) \tag{3.29}$$

for the deformation of a pure dissipative element under an AC force. Comparison of the experimental behavior in equation 3.26 and the response of a pure dissipative element in equation 3.29 imply that the protein is behaving similar to a pure dissipative element at low frequencies. At the high frequency limit of Fig. 3.10,

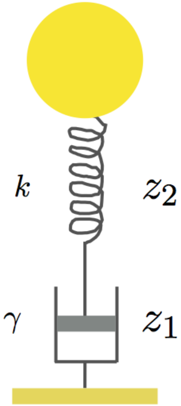

Figure 3.11: Maxwell model of a solid. The Maxwell model consists of an elastic spring in series with a dissipative dashpot. The total strain of the system is the addition of strain of each element.

the deformation amplitude is independent of the frequency, implying an elastic response.

In summary, the protein qualitatively shows two behaviors, a pure dissipative response at low frequencies and a pure elastic response at high frequencies. The response of the protein showing a dissipative behavior at low frequencies and an elastic behavior at high frequencies can be explained in terms of a unified model of an elastic element and a dissipative element in series [35, 36, 37]. This type of model was first studied by James Clerk Maxwell in the mid 18th century and a material which shows such a response is called a Maxwell material.

3.4.2 Maxwell model of solids

Fig. 3.11 shows a representation of the Maxwell model. The total strain of the system is the addition of strains of each element.

$$z = z_1 + z_2 \tag{3.30}$$

which implies that,

$$\dot{z} = \dot{z}_1 + \dot{z}_2. \tag{3.31}$$

For the elastic element,

$$z_2 = f/k \Rightarrow \dot{z}_2 = \dot{f}/k \tag{3.32}$$

For the dissipative element,

$$z_1 = f/\gamma \tag{3.33}$$

Substituting equations 3.32 and 3.33 in 3.31 gives

$$\dot{z} = f/\gamma + \dot{f}/k. \tag{3.34}$$

Equation 3.34 is the equation of motion of the gold nano particle. The inertial term can be safely neglected at these relatively low frequencies. Another force that is omitted from this equation of motion is the hydrodynamic dissipation from the gold nano particle $6\pi\eta r\dot{z}$. Again, the hydrodynamic dissipation from a gold nano particle can be neglected since we are interested in the dynamics at relatively low frequencies (100 Hz as opposed to ∼10 Khz). The solution of equation 3.34 for a force $f = f_0 exp(-i\omega t)$ can be written as

$$|z(\omega)| = \frac{f_0}{\gamma\omega}\sqrt{1 + \frac{\omega}{\omega_c}} \tag{3.35}$$

where $\omega_c = k/\gamma$ is the corner frequency at which the dissipative behavior changes to the elastic regime. At frequencies below ω_c, the internal dissipation of the protein is prominent resulting in a flow like behavior which is the reason for the $1/\omega$ divergence. At high frequencies, the dissipative element is essentially 'frozen' since it cannot respond at the fast time scale. Thus, the elastic nature of the protein is prominent at high frequencies.

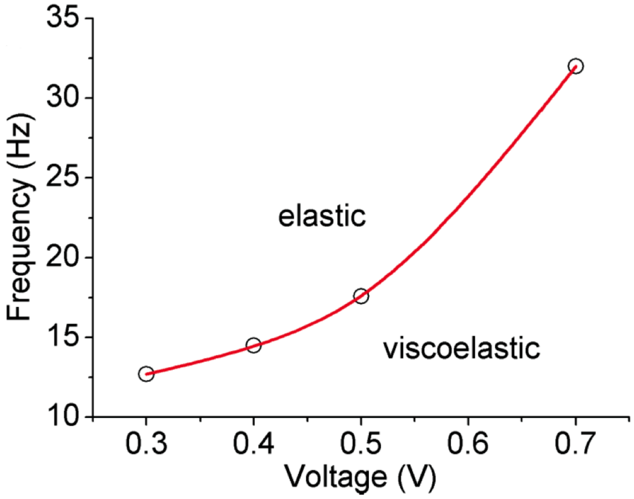

Figure 3.12: Variation of the corner frequency ω_c with the forcing amplitude. A monotonic increase of the corner frequency can be seen. The response is elastic above the corner frequency and viscoelastic (dissipative) below the corner frequency.

In the experiments with Guanylate kinase, the value of ω_c was found to be typically around 20 Hz. The corner frequency ω_c showed a dependence on the applied voltage, where ω_c increased monotonically with the amplitude of the AC forcing [38] (Fig. 3.12). Taking the corner frequency ω_c as $2\pi \times 20$ Hz and the elastic constant k to be 5 pN/nm (determined by previous experiments using the DNA spring [39]), we can estimate the internal friction coefficient to be $\approx 4.0 \times 10^{-5}$ Kg/s.

3.5 Effect of temperature on the mechanics of the protein

Using the methods described in the previous section, the mechanical properties of a globular protein Guanylate kinase were determined. It was found that this protein behaves elastically for low forcing and the protein shows dissipation for high forcing. The dissipative behavior is due to the internal viscosity of the protein

[36]. The internal dissipation coefficient for the protein was found to be around 4.0×10^{-5} Kg/s.

If we are studying materials properties of a new material, we would also want to know how these properties change with temperature. For example, scientists knew from simple experiments that the Youngs modulus of a metal does not change appreciably with temperature while the viscosity of tar decreases considerable with increasing temperature. With a similar goal in mind, we studied the influence of temperature on the mechanical properties of the folded state of the protein. The experiment described in the previous section is suitable for the particular measurement, as we can easily probe the protein in its native state while measuring the deformation of the protein at sub angstrom resolution.

3.5.1 Temperature control for the nano rheology setup

Fig. 3.13 shows the setup to perform the nano rheology experiment with temperature control. A metallic enclosure was made to house the prism, the fluid chamber (Au coated slides). The temperature of the fluid chamber was regulated by two water blocks glued (with thermal epoxy) to the metallic enclosure. Water from a temperature regulated water bath was driven through the water blocks in order to regulate the temperature inside the metallic enclosure. A thermocouple was attached to the surface of the Au coated cover slip to record the temperature inside the sample. The temperature of the fluid chamber was found to equilibrate to a value 2-3 degrees off from the temperature of the water bath in less than 30 minutes. Data for the rheology experiment was taken after the thermal equilibration of the fluid chamber.

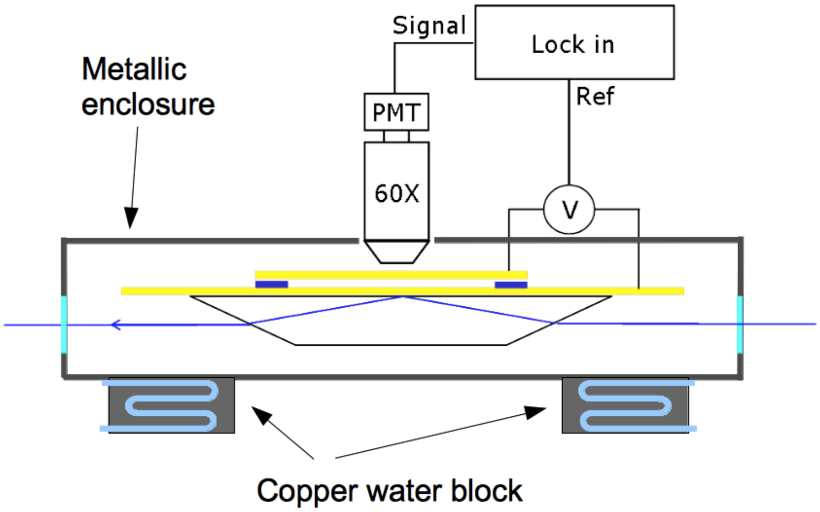
Signal
Lock in
Metallic enclosure
Ref
PMT
60X
V
Copper water block

Figure 3.13: Setup to control temperature of the nano rheology experiment. A metallic enclosure was built to cover the fluid chamber and the prism. Copper water blocks were attached to the metal box to regulate the temperature of the enclosure. The readout from a thermocouple attached to the fluid chamber was used as the working temperature.

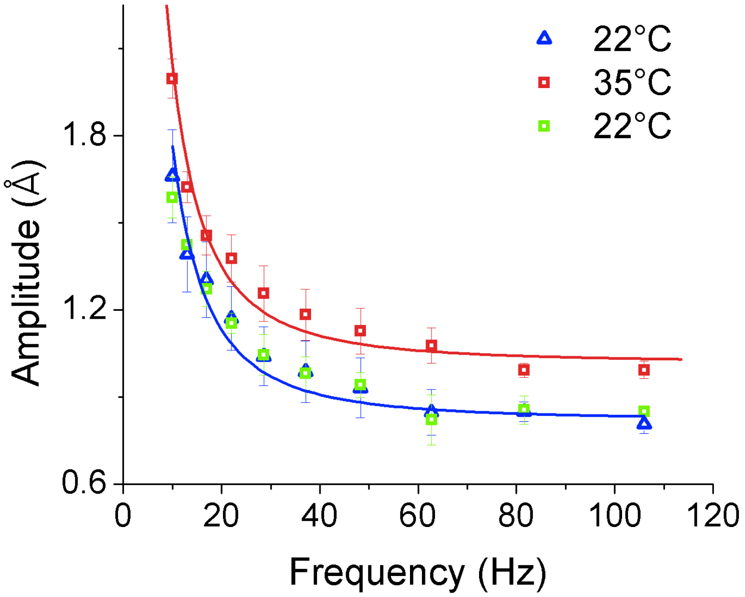

Figure 3.14: Reversibility of the Mechanical response of GK at 35 °C. The response was recorded initially at 22 °C (blue data points) and the temperature was raised to 35 °C to obtain the response shown in the red data points. The temperature of the fluid chamber was lowered back to 22 °C to record the data in green points. The overlapping of blue and green data points implies that the mechanics of the protein was altered reversibly. The fits were produced by using equation 3.36.

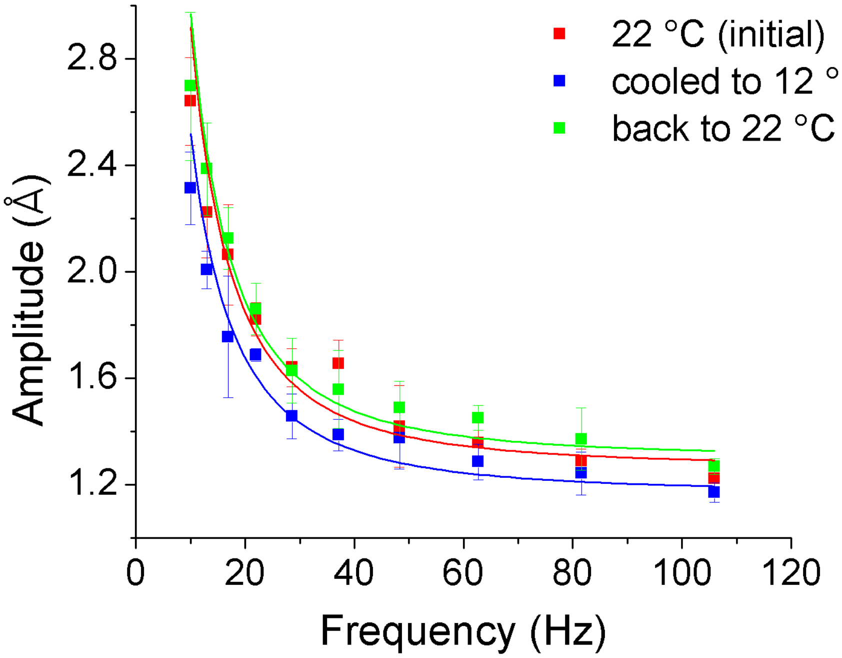

Figure 3.15: Reversibility of the Mechanical response of GK at 12 °C. Initially, the response was recorded at 22 °C (shown in red points). The temperature was lowered to 12 °C to record the response shown in blue points. Raising the temperature back to 22 °C (green points) can reproduce the initial behavior. The fits were produced by using equation 3.36.

3.5.2 Effect of temperature on the materials properties of Guanylate kinase

Fig. 3.14 shows the effect on the frequency response of the protein at two different temperatures, at 22 °C and at 35 °C. The amplitude of forcing is kept at the same level in both cases (250 mV). A clear effect on the amplitude of deformation can be observed, where the increase in temperature corresponds to an increase in oscillation amplitude. These curves were obtained from the same sample. This is important due to the fact that the relation between the actual force on the gold nano particle and the applied voltage could be different from sample to sample. Thus, for two different samples, applying a voltage of 250 mV could result in two different forces on the gold nano particle. Since the corner frequency ω_c depends on the force as shown in Fig. 3.12, it makes sense to compare data taken from the same sample. Another important aspect shown in Fig. 3.14 is the reversibility of the measurement.

The blue data points represent the data taken initially at the room temperature of 22 °C. The temperature was subsequently raised to 35 °C to obtain the red points. The green data points were taken after bringing the system back to 22 °C and as evident, the response of the protein can be reproduced.

Fig. 3.15 shows the effect of cooling the protein from 22 °C to 12 °C. A reduction in the deformation amplitude can be observed in this case. In addition, cooling the protein to 12 °C does not alter the protein irreversibly.

Fig. 3.16 shows the frequency response of the enzyme GK measured at three temperatures, 22 °C, 32 °C and 45 °C. All three curves were from the same sample and the forcing amplitude was the same. At these temperatures, the mechanics of the protein was reversible; bringing the system back to room temperature can reproduce the original curve. The important feature of this graph is the increase in the deformation amplitude of the protein with increasing frequency.

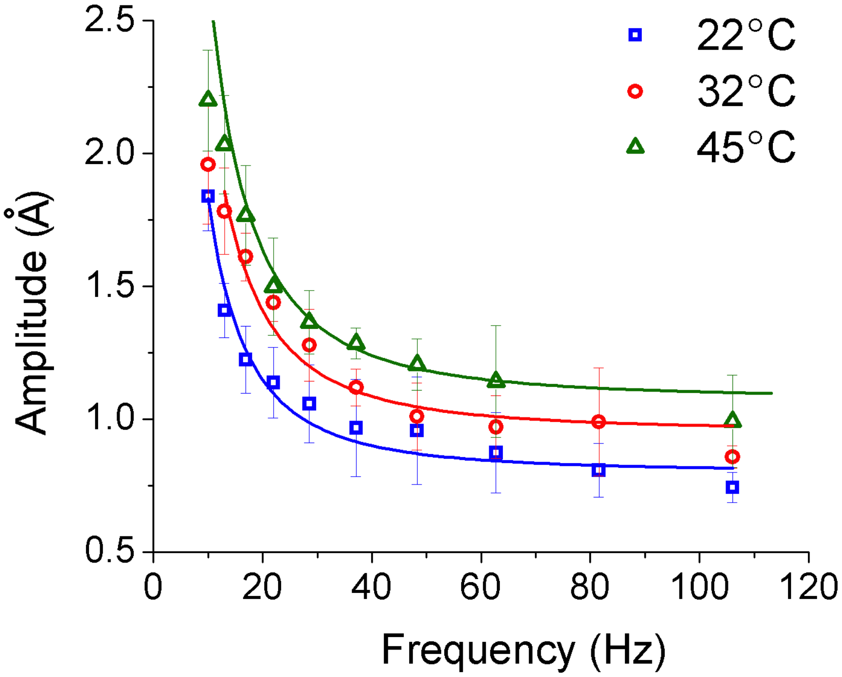

Figure 3.16: Mechanical response of GK at elevated temperatures. The response at different temperatures was recorded from the same sample and each point corresponds to the average of 5 recordings. A clear increase in the deformation amplitude can be seen as the temperature is elevated. The fits were produced using equation 3.36.

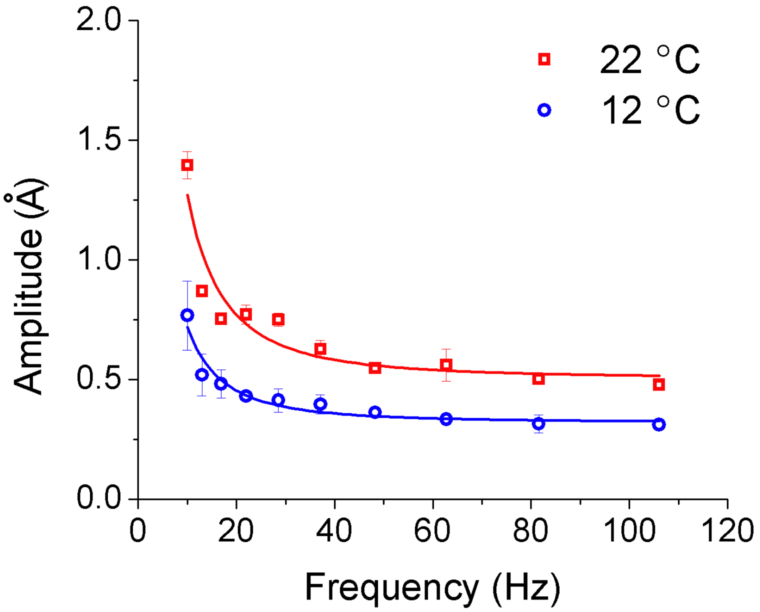

Figure 3.17: Mechanical response of GK at 12 °C. Reducing the temperature lowers the deformation amplitude for the same amplitude of forcing. The fits were produced using equation 3.36.

Fig. 3.17 shows the frequency response at a temperature lower than room temperature, 12 °C. The decrease in temperature corresponds to a decrease in deformation amplitude. In addition, the response at 12 °C is reversible.

The mechanical response of the protein is irreversible beyond a certain temperature regime. At higher temperatures it is well known that the protein will denature [40]. In addition to this denaturation at a warm temperature, there exists a cold temperature at which the protein denatures; known as the cold transition temperature [41]. Fig. 3.18 shows the denaturation of the protein at a warm temperature of 55 °C. The red points show the response at 55 °C, which is a feature less response when compared to the room temperature response. Lowering the temperature back to room temperature does not reproduce the original room temperature curve.

The cold denaturation of the protein is shown in Fig. 3.19. Here, the sample was cooled to 2 °C starting from room temperature. The frequency response of the protein is similar to the response observed at the elevated temperature of 55 °C shown in Fig. 3.18 and raising the temperature back to room temperature does not produce the original response. In both cases, the reduction of the oscillation amplitude can be interpreted as a denaturation of the protein at the surface where it partially absorbs on the surface.

The thermodynamic stability of a protein is a non-monotonic function of temperature [42, 43, 44]. It is well known that a protein has a warm and a cold unfolding transition. Fig. 3.20 shows a rough sketch of the free energy difference between the unfolded state and the folded state as a function of temperature for the enzyme GK. As the temperature approaches either 2 °C or 55 °C, the stability of the folded state reduces, possibly unfolding the protein. Thus, based on this observation, one would expect that the protein will soften mechanically as the temperature approach either of these two temperatures. In other words, the predicted shape for the mechanical stiffness will show a non-monotonic behavior

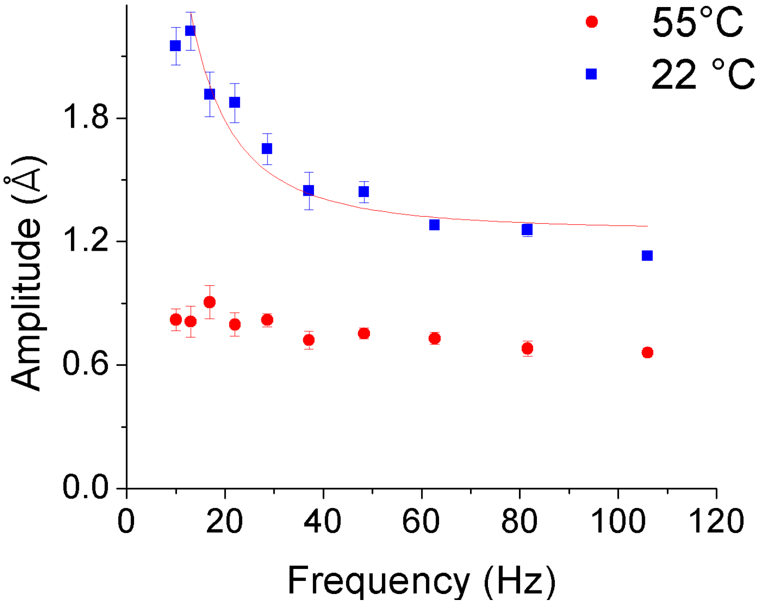

Figure 3.18: Irreversible denaturation of the protein at 55 °C. The response of the protein is feature less at the elevated temperature. Lowering the temperature back to 22 °C cannot reproduce the initial behavior. The fit for 22 °C data was produced using equation 3.36

in temperature similar to Fig. 3.20.

However, we can use the data in Figs. 3.16 and 3.17 to experimentally calculate the variation of the mechanical properties with temperature. Equation 3.35 can be used to understand the response of the enzyme in the folded state using the viscoelastic description. Since the force F_0 is not calibrated, it is impossible to measure the absolute value of k and γ at each temperature. Equation 3.35 can be written as

$$|z| = \frac{A}{\omega}\sqrt{1 + \left(\frac{\omega}{B}\right)^2} \tag{3.36}$$

where $A = F/\gamma$ and $B = \omega_c = k/\gamma$. Equation 3.36 can be used to fit data in Figs. 3.16 and 3.17 with A and B as the fitting parameters. Note that $1/A \propto \gamma$ and $B/A \propto k$. Thus, plotting $1/A$ and B/A versus temperature will show the variation of the dissipation coefficient and the elastic parameter with temperature.

Fig. 3.21 shows the experimentally measured variation of k and γ with temperature, normalized to 1 at 22 °C. It is evident that the dissipation coefficient and the elastic parameter fall monotonically with increasing temperature. This behavior is contradictory to the prediction that can be made by considering the thermodynamic stability of the protein in Fig. 3.20. The dissipation coefficient decreases by almost a factor of 2 in the temperature range of 12 °C to 45 °C while the elastic parameter follows a roughly similar trend. Schlierf and Rief [45] previously measured the shift in the unfolding transition state of a protein with raising temperature. They inferred a softening of the protein's elastic parameter by a factor 7 between 5 °C and 37 °C, a much larger effect than measured with the nano rheology experiment. Direct measurements on the folded state and previous unfolding experiments thus give different views of the mechanics.

The corner frequency ω_c can be interpreted as a rate of crossing the linear

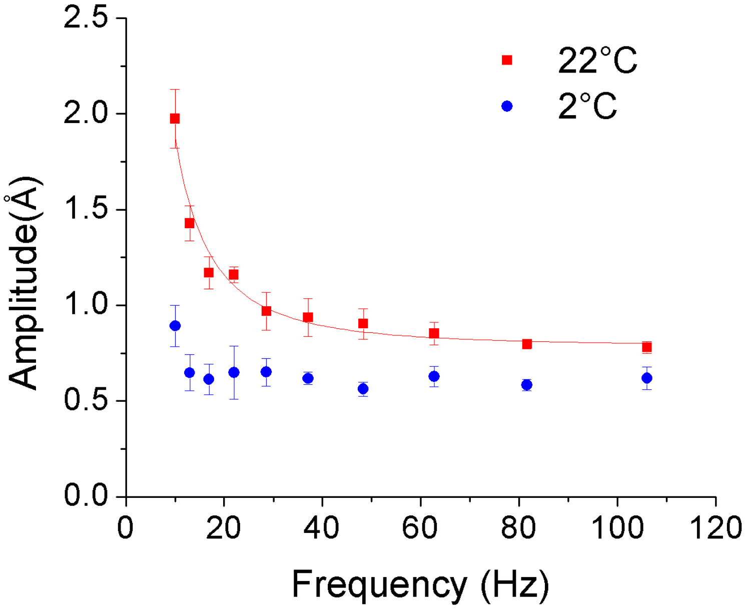

Figure 3.19: Irreversible denaturation of the protein at 2 °C. The response at 2 °C is essentially feature less. The amplitude is much smaller than at 22 °C and raising the temperature back to 22 °C cannot reproduce the initial response. The fit for data at 22 °C was produced using equation 3.36.

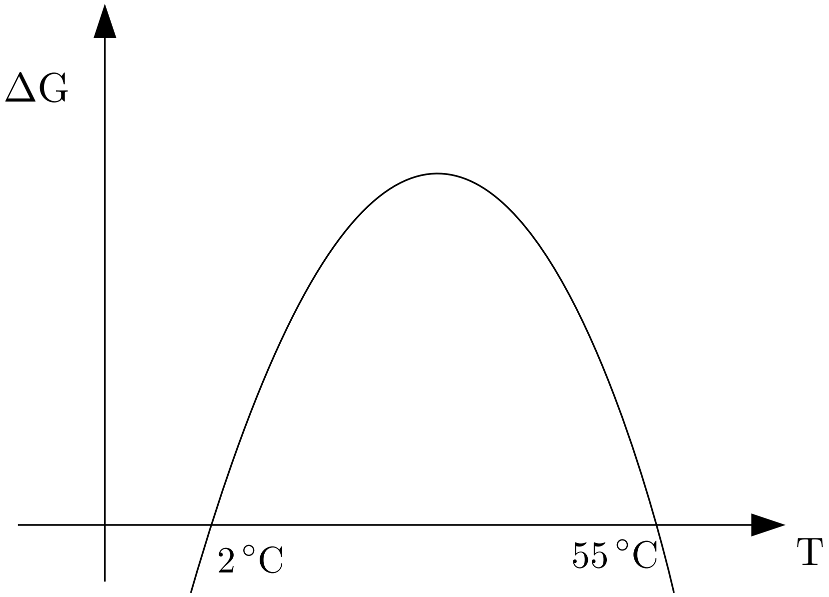

Figure 3.20: Thermodynamic stability of the protein versus temperature. The y-axis is the free energy difference between the unfolded state and the folded state (ΔG). At room temperature, the free energy of the unfolded state is a maximum, implying that the folded state is stable. As the temperature approaches 2 °C or 55 °C, the stability of the folded state decreases.

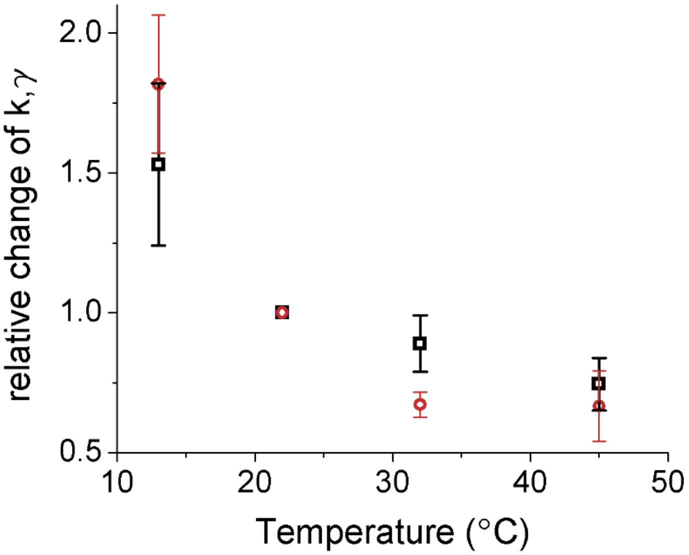

Figure 3.21: Variation of k and γ with temperature. The plot is the relative change of the mechanical parameters with respect to that of room temperature. The values for k and γ were obtained by the fits in Figs. 3.16 and 3.17.

elasticity regime to the viscous regime. Thus, an Arrhenius plot of log (ω_c) vs. $1/T$ gives the energy barrier [46] for crossing over from the linear elasticity regime to the dissipative regime. Fig. 3.22 shows the plot of log (ω_c) vs $1/T$ and from the slope of the fit, a barrier height of $\approx 1.9\ k_B T$ can be measured. This energy scale corresponds to the energy of a covalent bond. It must be mentioned that, even though Fig. 3.22 shows a straight line fit, the temperature range is too narrow to extract useful information.

The relative changes of k and γ can be compared with similar trends of other materials. For example, the viscosity of water decreases by a factor of 2 between 10 °C and 40 °C while the bulk modulus of water increases by ~ 14 % in the same temperature range. Given the nano meter size of the protein, it's not surprising to assume that both the surface and the interior of the molecule contribute to the mechanical response of the protein. The surface of the protein after all is a complex

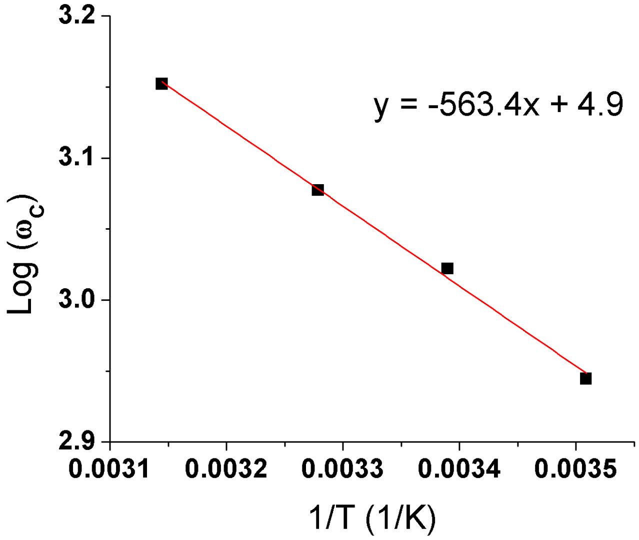

Figure 3.22: Arrhenius plot of log (ω_c) versus 1/T. The coner frequency ω_c was determined from the fits in Figs. 3.16 and 3.17.

interface with hydrogen bonding to the water molecules. In the next section, I will discuss an experiment that was performed to investigate the influence of the surface of the protein to its mechanics.

3.6 Influence of the hydration shell on the mechanics of the protein

Enzymes are soft, heterogeneous nanoparticles with specific catalytic activity in aqueous environment. All the action is at the surface of the enzyme, which often deforms considerably upon binding of the reactants. These large deformations are driven primarily by surface forces, i.e. the interaction between the substrates and the surface of the enzyme. Due to the small size of an enzyme ($\sim$ 5 nm) the surface contribution to the dynamics is not overwhelmed by the bulk contribution. The percentage of amino acids exposed to water is a considerable fraction of the total number of amino acids.

The surface of the enzyme is a complex dynamic network of hydrogen bonds between water molecules in the hydration shell of the protein and residues at the enzyme's surface. In this section, I discuss an experiment performed to probe the contribution of the hydration shell of a protein to its mechanics using the nano rheology setup discussed earlier and the results showed that this interface (protein − water) partially controls the mechanics of the enzyme. We chemically modify the hydration shell by addition of the molecule DMSO, a kosmotropic (order inducing) agent.

3.6.1 Hydration shell of a protein

The hydration shell of the protein has been probed with different experimental techniques including NMR [50], X-ray crystallography [51], Tera Hertz wave spectroscopy [52] and molecular dynamic simulations [53]. The water in the hydration shell is ordered when compared with bulk water (which lacks an ordering) and this shell is believed to be around $2-3$ water molecules thick. A cartoon representation of the hydration shell of Guanylate kinase is depicted in Fig. 3.23.

In order to probe the influence of the hydration shell on the mechanics of the protein, we must perturb the hydration shell. In this study, we use a chemical perturbation on the hydration shell by using the molecule dimethyl sulfoxide (DMSO). DMSO is used as a cryoprotectant and as an order-inducing agent. It has both polar and non-polar properties and the molecule has a large dipole moment of 3.96 Debye (dipole moment of water is 1.85 Debye). In the bimolecular context, the interesting property of DMSO is that it hydrogen bonds with water, the water − DMSO bond being somewhat stronger than the water − water bond [47]. Furthermore, the presence of DMSO strengthens the water − water bond [47]. It is a "kosmotropic" agent, believed to increase the ordering of water molecules in the first hydration shell of water-dissolved substances [48, 49].

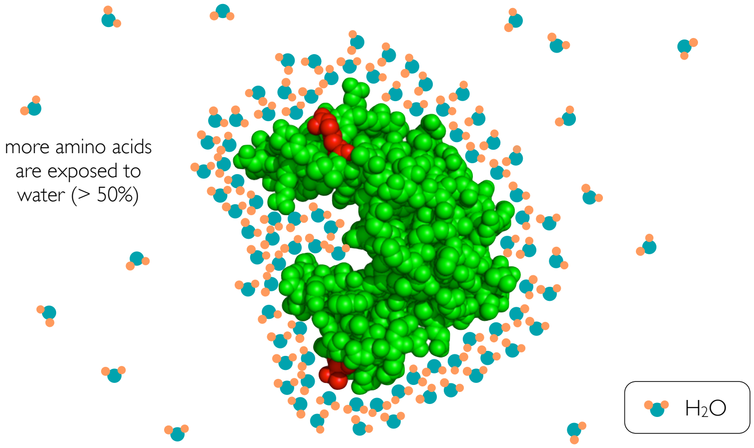

Figure 3.23: Cartoon representation of the hydration shell of a protein. A 2−3 water molecule layer forms the hydration shell. The molecules in the hydration shell are in an ordered state compared with the bulk water with slow dynamics.

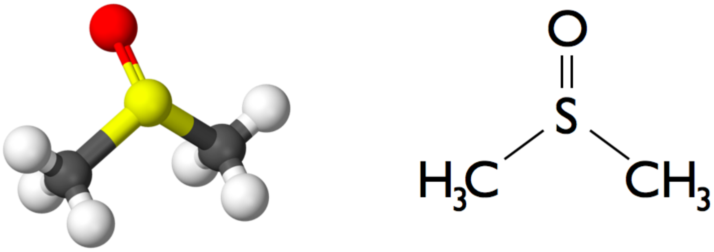

Figure 3.24: Structure of the molecule DMSO. The molecule has a trigonal pyramidal structure, with a central sulfur atom. DMSO has non polar characteristics due to the presence of the methyl groups and polar characteristics due to the highly polarized S−O bond.

The concentration of DMSO used in the experiment is at most about 1%. The viscosity of DMSO is 1.996 cP and the viscosity of water is 1 cP (at 20 °C). Thus the addition of 1% DMSO to water will increase the viscosity to 1.01 cP which is only $\approx 1\%$ change in the viscosity of bulk water. Similarly, the dielectric constant of water is around 80 while that of DMSO is 48 and addition of 1% DMSO to water modifies the dielectric constant of bulk water by $\approx 0.4\%$. Thus, if significant change in the mechanical response is observed, it must originate due to the chemical modification of the hydration shell.

Fig. 3.25 shows a cartoon representation of the hydration shell of the protein with DMSO incorporated. As mentioned earlier, various experimental techniques verified that DMSO actually translocate to the hydration shell of the protein, but it was not known how this modification of the hydration shell effect the mechanics of the protein.

One aspect that must be addressed is the question of whether the addition of DMSO alters the relation between the applied voltage across the fluid cell and the actual force F_0 on the gold nano particle. This question was addressed by investigating the effect on frequency response of a single stranded DNA with and without DMSO. Fig. 3.26 shows the construction used for this control experiment. DNA Arm B was initially tethered to the gold-coated slide employing a similar technique as used in the case of tethering GK. DNA Arm A was then separately hybridized to the gold nano particles using the technique described in [54]. DNA Arm A has a 12 base pair region at the end that is complementary to the end of Arm B. Thus, addition of DNA Arm A modified gold nano particles on the Arm B tethered gold slides results in a tethering of the gold nano particle on to the gold coated slide.

Fig. 3.27 shows the effect of DMSO on the frequency response of a single stranded DNA. In both cases, the gold nano particles were driven with the same applied voltage. The frequency response is flat (independent of frequency) as a

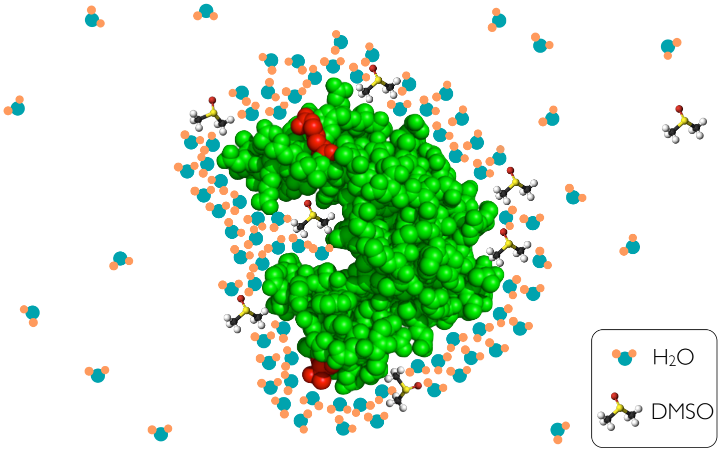

Figure 3.25: Cartoon representation of the hydration shell of a protein with DMSO. DMSO can aggregate at the hydration shell of the protein, modifying the hydration shell.

single stranded DNA is a polymer coil that behaves as an entropic spring. The relation between the displacement z and the applied force $F(\omega)$ is $z = F(\omega)/k$ where k is the spring constant. Thus, the fact that the two responses (with and without DMSO) are similar implies that the addition DMSO does not alter the relation between the force on the gold nano particle and the applied voltage across the fluid cell (the unlikely scenario where both k and F_0 change with the same ratio is ignored).

Now that we have established that adding a small concentration of DMSO to the buffer solution does not alter its physical properties or alter the applied voltage versus F_0 relation, we are in a position to gauge the mechanical effect of DMSO on a protein. Fig. 3.28 shows the effect of 1% DMSO on the mechanical response of the enzyme GK. A clear reduction in the oscillation amplitude can be seen (about a 100 % effect), much larger compared to the change in bulk properties of water with the addition of DMSO ($\sim 1\%$).

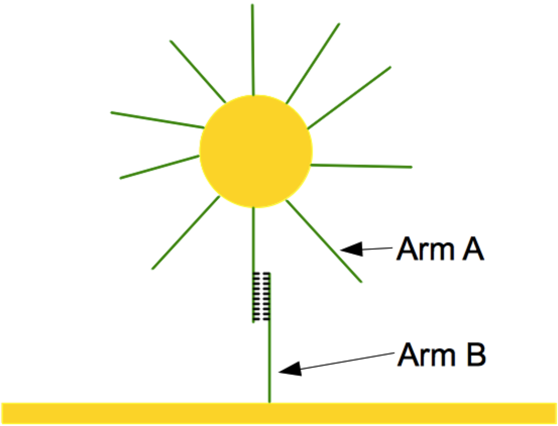

Figure 3.26: Gold nano particle tethered by a single stranded DNA molecule. DNA Arm B was attached to the gold coated slide via a thiol modification. DNA Arm A was conjugated with gold nano particles separately [54]. DNA Arm A and Arm B were designed such that they have a complementary region of 12 base pairs at their ends. Thus, addition of DNA modified gold nano particles on the DNA Arm B modified slide tethers the gold nano particles on the slide.

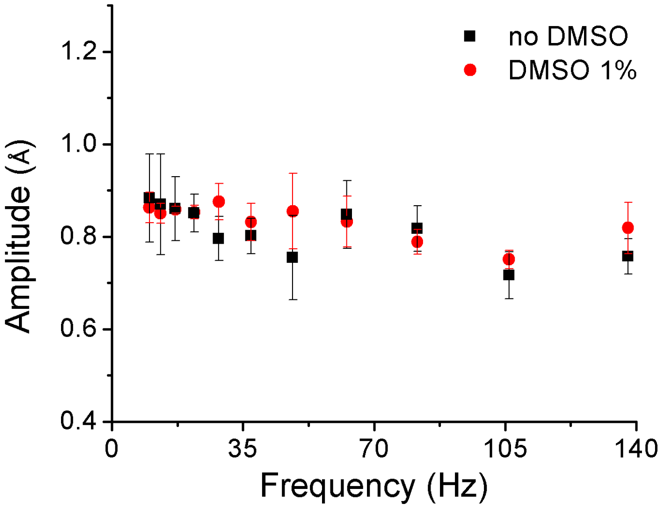

Figure 3.27: Frequency response of a single stranded DNA molecule with and without DMSO. The data for the response curve was obtained with the geometry shown in Fig. 3.26. Single stranded DNA behaves as a random coil, which is an entropic spring. The fact that the response amplitude does not change with DMSO implies that the relation between the voltage applied across the fluid cell and the actual force on the gold nano particle does not change with DMSO.

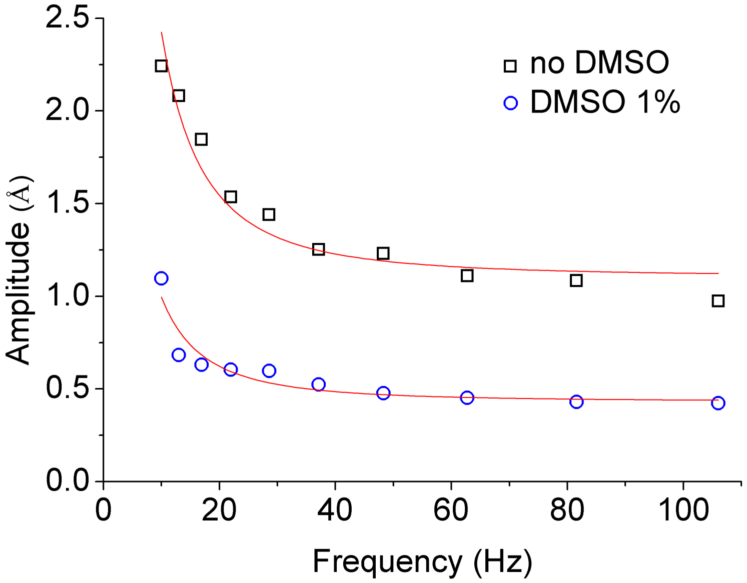

Figure 3.28: Effect of 1% DMSO on the mechanics of the protein. Data shows the response amplitude vs. forcing frequency in the absence (squares) and presence (circles) of 1% DMSO, for the same sample. Lines are fits with the viscoelastic response 3.36. Each point is the average of 4−5 measurements and the standard deviation is usually 0.1 Å.

Fig. 3.29 shows the reversibility of the effect of DMSO on the protein. The frequency response of the protein was measured without DMSO initially (shown in black squares) and then the buffer was changed to 0.5 % DMSO solution to measure the frequency response with DMSO (blue circles). Thorough washing steps were then performed to transfer the buffer back to DMSO free solution and the frequency response was measured again (green triangles). The addition of 0.5% DMSO causes a reduction in the amplitude of the mechanical response, implying that the protein is stiffer. The subsequent removal of DMSO can reproduce the initial DMSO free curve, which shows that this effect is reversible.

The fits in Figs. 3.28 and 3.29 were produced using equation 3.36. The two fitting parameters in this viscoelastic description of the protein, A and B can be used to extract information about the dissipation coefficient and the elastic

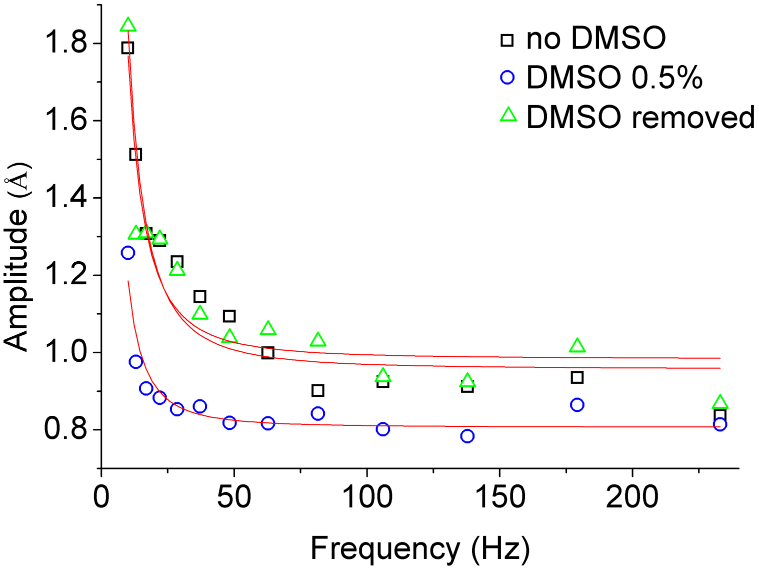

Figure 3.29: The change in mechanical response due to DMSO is reversible. The figure shows, for the same sample, the response amplitude vs. frequency before adding DMSO (squares), after adding 0.5 % DMSO (circles), and after removing DMSO (triangles). Each point is an average of 4-5 measurements and the standard deviation is ∼ 0.1 Å. Lines are fits with the viscoelastic response 3.36

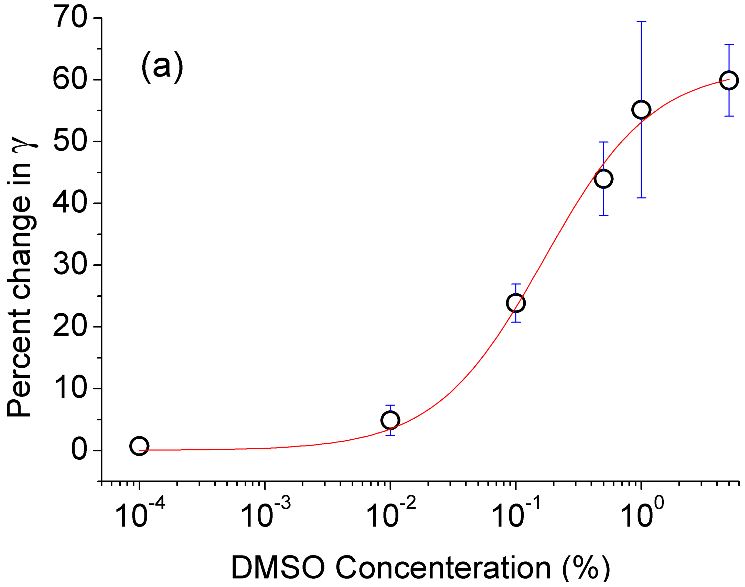

Figure 3.30: Variation of γ (the dissipation parameter of the viscoelastic description) with DMSO concentration. Percent change in the viscoelastic dissipation parameter (measured from fitting to equation 3.36) vs. DMSO concentration. The curve is a fit produced with equation 3.37, giving the values $K_D = 0.17$ % and α= 62 %. Each point is calculated by averaging 5 measurements and the error bars indicate uncertainty $(\sigma/\sqrt{N})$. The dissipation increases by 60 % in the presence of DMSO.

coefficient of the protein. As discussed in the previous section, the dissipation parameter γ is proportional to $1/A$ and the elastic coefficient is proportional to B/A. Thus, by obtaining traces similar to Fig. 3.28 at different DMSO concentrations, and fitting with equation 3.36, it is possible to determine the relationship between DMSO concentration in the bulk solution and the effect on the two mechanical parameters of the viscoelastic description.

Fig. 3.30 shows the effect of DMSO concentration on the dissipation parameter. There is almost no effect on the dissipation parameter when DMSO concentrations around $\sim 10^{-4}\%$ is used. The dissipation parameter increases with DMSO concentration, but shows a saturation effect after 1%, at which point the dissipation parameter shows a roughly 2-fold increase from the DMSO free case. The change in the dissipation parameter can be modeled well with a binding isotherm (equation 3.37). Left hand side of equation 3.37 is the relative change in the dissipation parameter γ (γ_0 is the dissipation parameter with no DMSO), [DMSO] is the DMSO concentration, K_D plays the role of a dissociation constant and α is a normalization factor. The value obtained for K_D by fitting Eq. 3.37 in data of Fig. 3.30 is $K_D = 0.17\% = 24$ mM.

$$\frac{\gamma - \gamma_0}{\gamma_0} = \frac{\alpha}{1 + K_D/[DMSO]} \tag{3.37}$$

Fig. 3.31 shows the effect of DMSO on the elastic parameter of the viscoelastic model (Equation 3.36). A sharp trend as in the case of γ cannot be seen with the elastic parameter. This result can either be interpreted simply as no effect or a ~ 20 % effect due to the noisy nature of the data. The reason for this is the poor determination of the corner frequency ω_c at higher DMSO concentrations.

Thus, it can be concluded that DMSO can make the protein more viscous by modifying the hydration shell of the protein. This simple experiment shows that the hydration shell plays an important role on the mechanics of the protein

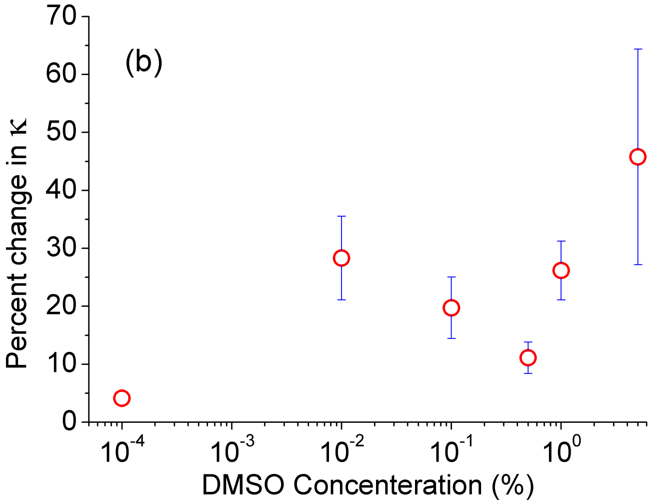

Figure 3.31: Variation of k with DMSO concentration. Given the large error bars, it is not clear whether k is unaffected or increases slightly with DMSO. Each point is calculated by averaging 5 measurements and the error bars indicate uncertainty ($\sigma/\sqrt{N}$).

GK. Since a hydration shell covers the surface of every protein, it must be a general property to all proteins. Another interesting observation is that DMSO accumulates at the surface of the protein and occupies a finite number of binding sites. This scenario is not true if the saturation seen in Fig. 3.30 is an artifact of saturation of the effect of DMSO on the dissipation parameter γ at concentrations ~ 1 %.

CHAPTER 4

Biosensor based on nano rheology

For many applications including drug development and enzymology research, it is desirable to develop label free, fast, low cost methods to detect and quantify small molecules binding to enzymes. For instance, one might be screening for inhibitors of a given enzyme or measuring hormone levels in a blood sample. For enzymology research, substrates binding affinities are a parameter of interest. Standard spectroscopic methods (such as UV absorption and fluorescence measurements) are inadequate for measuring enzyme − substrate binding affinities in a label − free context, first because a sufficient spectroscopic signature of binding may not be present intrinsically, and also because binding affinities are often in the μM range, which implies working with dilute samples. High sensitivity methods such as NMR can be used to detect binding of small bio molecules to the substrate enzyme, but they require costly, specialized equipment.

There have been many developments based on nano technological approaches to detect small molecules. For example, surface plasmon resonance (SPR) [55, 56] based schemes and mechanical resonance of nano−cantilevers [57, 58] are some of the promising techniques. SPR based techniques rely on the change of the dielectric constant upon ligand binding to detect a change in the optical signal whereas the nano - cantilever measures the total mass of the molecules attached to the cantilever through the resonance frequency of the structure. Even though both methods are sensitive to the mass of the ligand, both of these methods cannot distinguish specific binding of ligand molecule to substrate enzyme. In contrast, the technique that we propose is sensitive only to ligand binding, resulting in a change of mechanical stiffness of the enzyme. The method is sensitive only to ligand binding to the target enzyme, not the surface of the device.

The technique that we propose to detect bio molecules is via measuring the change in stiffness of the enzyme (the substrate molecule) upon binding its ligand [59, 60, 61]. The stiffness of the protein can be measured by using the nano rheology experiment discussed in Chapter 3. The nano rheology setup discussed in chapter 3 used evanescent wave scattering to detect the deformation of the enzyme. In this chapter, I will discuss a surface plasmon resonance based scheme to measure the deformation of the proteins and this technique has a much higher signal than the evanescent wave scattering based technique. The experimental setup is very similar to the one discussed in chapter 3. The new setup, shown in Fig. 4.1 uses a 632 nm laser in addition to the 488 nm laser. A mirror is used to switch between the beams.

4.1 Current SPR based biomolecule detection scheme

4.1.1 What are Surface plasmons?

Surface plasmons are a propagating mode of electromagnetic and electron oscillations confined to a thin metallic film - dielectric boundary. We know that for a metal, the electric permittivity ϵ_m at optical frequencies is given by

$$\epsilon_m = \epsilon_0\Big(1 - \frac{\omega_p^2}{\omega^2}\Big) \tag{4.1}$$

, where ω_p is the plasma frequency given by $\omega_p = ne^2/m\epsilon_0$. In the expression for ω_p, n is the free electron density, e is the electronic charge, m is the mass of an electron and ϵ_0 is the permittivity of free space. For gold, the plasma frequency is in the ultra violet regime, thus at optical frequencies, ϵ_m for gold is negative.

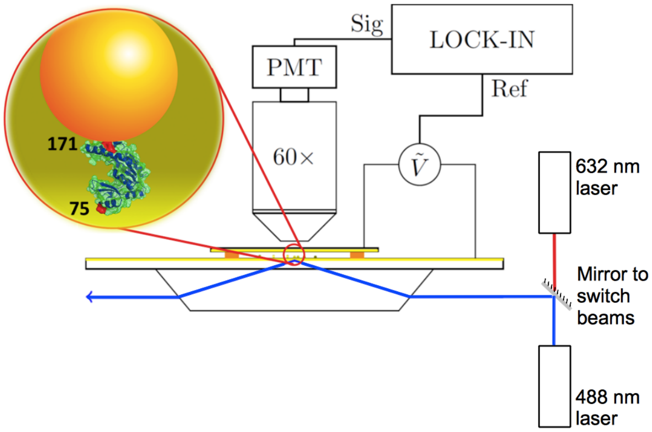
Sig
LOCK-IN
PMT
Ref
171
60×
$\tilde{V}$
632 nm laser
75
Mirror to switch beams
488 nm laser

Figure 4.1: The experimental setup. The enzyme is covalently coupled to the 30 nm Au layer on one side, and a 20 nm gold nano particle (GNP) on the opposite side. The negatively charged GNPs are driven by an oscillating electric field in a parallel plate capacitor arrangement in buffered saline sodium citrate (SSC). The amplitude of oscillation of the GNPs is measured by SPR enhanced scattering with phase - locked detection. There are $\sim 10^8$ GNPs in the field of view of the 60 X objective; the scattered intensity represents the ensemble averaged position of the GNPs.

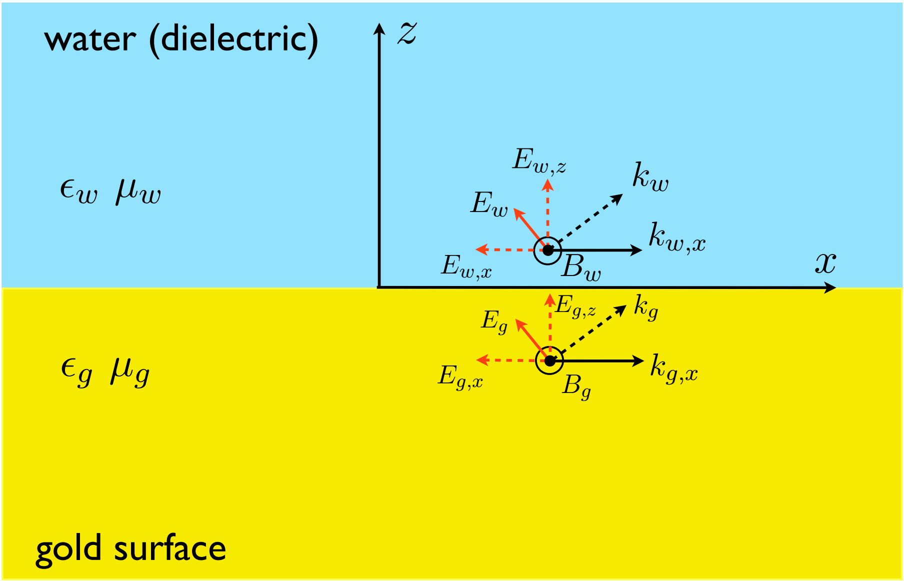

Figure 4.2: The interface between an Au surface and a dielectric (water). The propagating EM wave is shown in both media, where the magnetic field is directed out of the plane of the image.

The dispersion relation for EM waves in a medium is given by

$$k^2 = \epsilon\mu\frac{\omega^2}{c^2} \tag{4.2}$$

, where ϵ is the permittivity of the medium, μ is the magnetic permeability of the medium and c is the speed of light in vacuum. As ϵ_m is negative for visible light in gold, there are no propagating EM wave modes for visible light in gold.

However, when there is an interface between a dielectric and a gold surface, k can be a complex vector, imaginary in one direction, but real in another. There can be a travelling wave in the real direction of k and an exponential decay of fields in the imaginary direction of k. Let's look in to this in more detail.

Fig. 4.2 shows the geometry of the problem. Lets assume a plane wave in the x-z plane, incident with a wave vector $\vec{k}$ ($\vec{k} = k_x\hat{i} + k_z\hat{k}$) at the boundary. The magnetic field is in the y direction and the E field is perpendicular to both the wave vector and the magnetic field. Assume the wave vector k_x along x direction to be real (propagation along x direction). The dispersion relation is given by

$$k_x^2 + k_z^2 = \epsilon\mu\frac{\omega^2}{c^2} \tag{4.3}$$

$$k_z^2 = \epsilon\mu\frac{\omega^2}{c^2} - k_x^2 \tag{4.4}$$

The wave vector k_z can be shown to be imaginary in both media by the substitution of solution for k_x (equation 4.17) in equation 4.4. The boundary conditions for EM fields between the two media can be written as

$$E_{g,||} = E_{w,||} \tag{4.5}$$

$$\epsilon_g E_{g,\perp} = \epsilon_w E_{w,\perp} \tag{4.6}$$

$$B_{g,||}/\mu_g = B_{w,||}/\mu_w \tag{4.7}$$

$$B_{g,\perp} = B_{w,\perp} \tag{4.8}$$

Since the wave propagates along the x direction at the surface, the presence of the longitudinal E field implies that this is a TM wave. A relation between E and B can be found by solving for E from the Maxwells equation $\nabla \times \vec{B} = \epsilon\mu\big(\partial E/\partial t\big) = -i\epsilon\mu\omega E$ by using $\vec{B} = B_0\hat{j}e^{i(k_x x + k_z z - \omega t)}$. This procedure yields

$$\vec{E} = \frac{c^2 k_z}{\mu\epsilon\omega}B_0\hat{i} - \frac{c^2 k_x}{\mu\epsilon\omega}B_0\hat{k} \tag{4.9}$$

Application of the boundary conditions in equations 4.5 - 4.8 for the B field in figure 4.2 and the E field in equation 4.9 results in the following set of equations (Eq. 4.10 - 4.12).

$$\frac{c^2 k_{g,z}}{\mu_g\epsilon_g\omega}B_{0,g} = \frac{c^2 k_{w,z}}{\mu_w\epsilon_w\omega}B_{0,w} \tag{4.10}$$

$$\frac{c^2 k_{g,x}}{\mu_g\omega}B_{0,g} = \frac{c^2 k_{w,x}}{\mu_w\omega}B_{0,w} \tag{4.11}$$

$$B_{0,g}/\mu_g = B_{0,w}/\mu_w \tag{4.12}$$

Cancelling common factors in equation 4.10 and substituting for B_0 from equation 4.12 gives

$$\frac{k_{g,z}}{\epsilon_g} = \frac{k_{w,z}}{\epsilon_w} \tag{4.13}$$

Now we can use equation 4.4 for k_z to obtain the following expressions for $k_{g,z}$ and $k_{w,z}$.

$$k_{g,z} = \pm\big(\epsilon_g \mu_g \frac{\omega^2}{c^2} - k_{g,x}^2\big)^{1/2} \tag{4.14}$$

$$k_{w,z} = \pm\big(\epsilon_w \mu_w \frac{\omega^2}{c^2} - k_{w,x}^2\big)^{1/2} \tag{4.15}$$

Plugin in expressions 4.14 and 4.15 in equation 4.13 and solving for the wave vector of the propagating mode ($k_x = k_{w,x} = k_{g,x}$) gives

$$k_x^2 = \frac{\epsilon_g \epsilon_w \big(\epsilon_g \mu_w - \epsilon_w \mu_g\big)}{\epsilon_w^2 - \epsilon_g^2} \frac{\omega^2}{c^2} \tag{4.16}$$

The magnetic permeability μ can be approximated as 1 for most dielectrics and metals and this gives the dispersion relation for the surface plasmons as

$$k_x^2 = \frac{\epsilon_g \epsilon_w}{\epsilon_w + \epsilon_g} \frac{\omega^2}{c^2} \tag{4.17}$$

This solution for k_x can be used to calculate the electric field distribution around the interface by using equation 4.9. Figure 4.3 shows a sketch of the E field distribution about the interface. The gold surface shows clusters of positively and negatively charged regions. The electric field decays exponentially in each side with the metal side having a smaller skin depth than the dielectric side.

4.1.2 Surface plasmon resonance

Surface plasmon resonance is the excitation of these surface plasmons by pumping energy (usually laser light). There are two main techniques for achieving SPR,

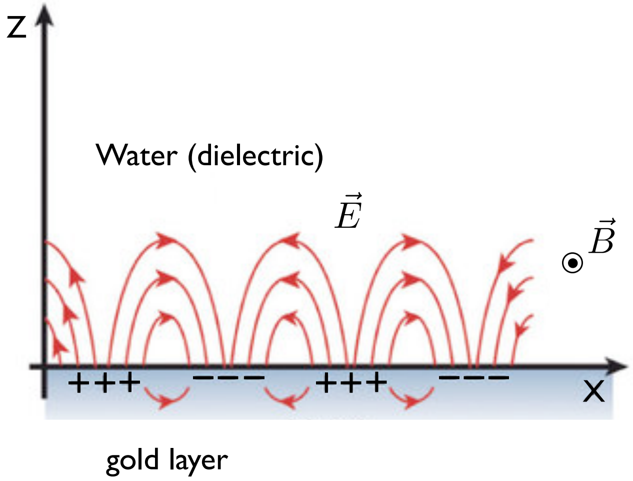

Figure 4.3: The distribution of the electric field about the interface. The field decays exponentially in either side of the boundary, the decay length in to gold being shorter than towards the dielectric side.

one of them being the prism-coupled method and the other being the grating-coupled method. In our work, we use a prism-coupled technique [62, 63] which is the most commonly used SPR technique. In this technique, an evanescent wave is generated at the face of a prism that is coated with a thin gold layer ($\sim$ 30 nm). This evanescent wave travels parallel to the prism face and the wave vector of the evanescent wave can be adjusted by changing the incident angle of the laser beam. At a certain incident angle, the wave vector of the evanescent wave can be exactly matched to the wave vector of the surface plasmons, establishing the resonance condition (SPR).

Fig. 4.4 shows the prism coupled configuration. The wave vector of the evanescent wave is given by equation 4.19. In the expression for the wave vector of the evanescent wave k_{EW}, θ_c is the critical angle for total internal reflection.

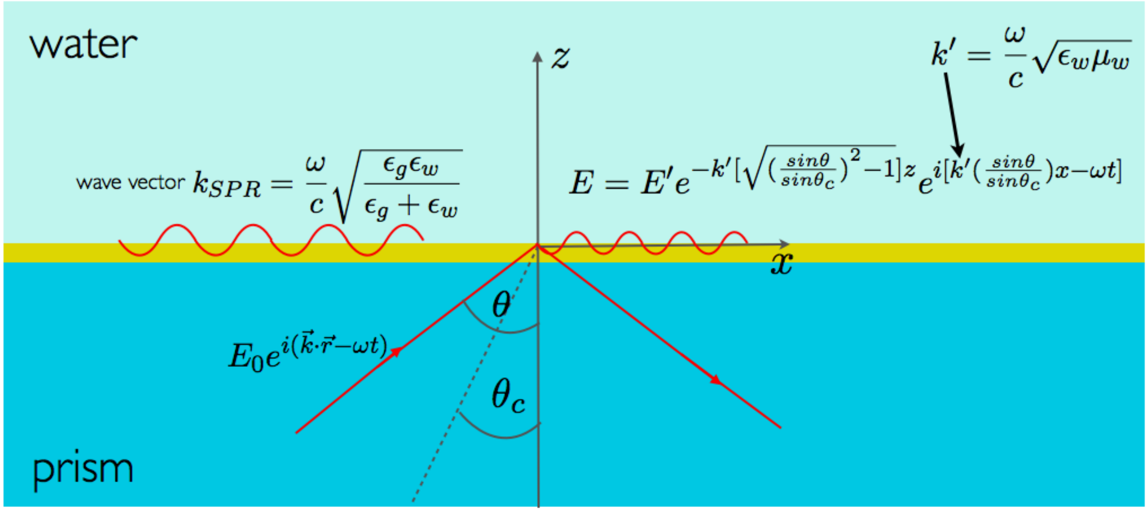
water
z
$k' = \frac{\omega}{c}\sqrt{\epsilon_w \mu_w}$
wave vector $k_{SPR} = \frac{\omega}{c}\sqrt{\frac{\epsilon_g \epsilon_w}{\epsilon_g + \epsilon_w}}$
$E = E' e^{-k'[\sqrt{(\frac{sin\theta}{sin\theta_c})^2 - 1}]z} e^{i[k'(\frac{sin\theta}{sin\theta_c})x - \omega t]}$
x
θ
$E_0 e^{i(\vec{k}\cdot\vec{r} - \omega t)}$
θ_c
prism

Figure 4.4: Surface plasmon resonance by prism coupled configuration. A laser beam is incident at an angle θ which is higher than the critical angle θ_c. The evanescent wave travels parallel to the gold surface with a wave vector dependent among many other things, the incident angle. At a certain incident angle, the wave vector of the evanescent wave and the surface plasmon wave vector match, giving rise to SPR.

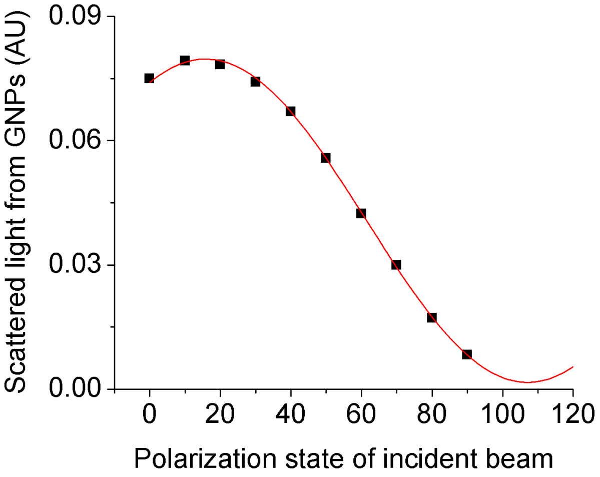

Figure 4.5: Variation of the scattered light intensity (SPR mode) with the direction of polarization of the incident laser beam with respect to the gold surface. As the polarization of the incident beam approaches 90° (s-polarized: electric field parallel to the gold surface), the intensity of the scattered beam vanishes. In the measurements, zero angle (p-polarized) was offset by about 15°. The line is a fit to a cosine function.

$$k_{EW} = \frac{\omega}{c}\sqrt{\epsilon_w \mu_w}\frac{\sin\theta}{\sin\theta_c} \tag{4.18}$$

Surface plasmon resonance occurs when the two wave vectors k_{SPR} and k_{EW} are equal:

$$\frac{\omega}{c}\sqrt{\frac{\epsilon_g \epsilon_w}{\epsilon_g + \epsilon_w}} = \frac{\omega}{c}\sqrt{\epsilon_w \mu_w}\frac{\sin\theta_{SPR}}{\sin\theta_c} \tag{4.19}$$

, where θ_{SPR} is the angle at which surface plasmon resonance occurs. In practice, the incident angle θ is varied while measuring the intensity of the reflected light from the interface. At surface plasmon resonance, part of the energy from the incident beam goes to excite the plasmons and results in a reduction of the reflected light intensity.

4.1.3 Detection of biomolecules with SPR

Fig. 4.6 shows the variation of the intensity of reflected light with incident angle. The dip in the intensity occurs due to resonant absorption of energy from the laser for excitation of surface plasmons. As shown in the figure, the reflected intensity plateaus after the critical angle θ_c but it drops sharply upon further increase in the incident angle.

As evident from equation 4.19, the solution of θ_{SPR} depends on the dielectric constant of the medium above the gold layer (which is the buffer solution). When proteins bind on the gold surface, the effective dielectric constant gets modified which in turn changes θ_{SPR}. This effect is depicted in Fig. 4.6, the black circles are obtained from a bare gold surface exposed to buffer solution while the red circles correspond to the same gold surface absorbed with a protein. This is the principle of operation of many SPR based biomolecule detection platforms [55].

However, the detection of binding of small molecules to protein substrates is a considerable challenge in SPR detection schemes. The usual technique is to first cover the gold surface with a densely packed layer (or many layers) of the protein and then observe the shift in the SPR angle with the binding of the target molecule on to the protein. Typically the target molecule can be 0.1% to 1% of the molecular weight of the protein. In such a scenario, the change in the SPR angle is very small as the change in local dielectric constant due to binding of the target molecule on the protein is roughly proportional to $M_{target}/M_{protein}$, where M_{target} is the molecular weight of the target molecule and $M_{protein}$ is the molecular weight of the protein on to which the target binds.

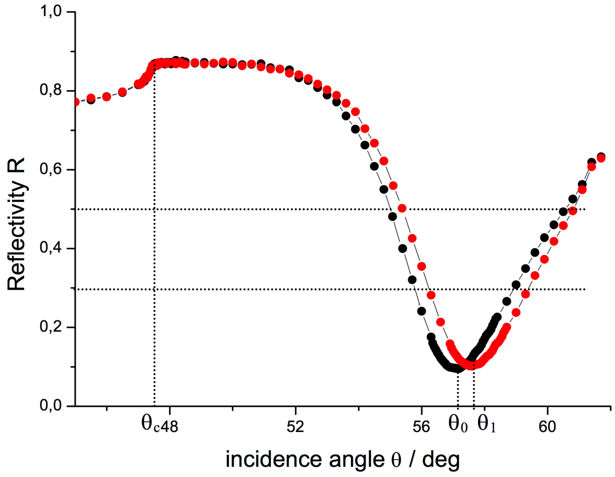

Figure 4.6: Variation of the reflected intensity with the incident angle. Near complete reflection occurs when the incident angle is above the critical angle. But, as the incident angle is increased further, a sharp resonant dip occurs due to the absorbance of the excitation beam (to excite surface plasmons). The angle at which the dip occurs change with the effective refractive index of the medium above the gold layer.

4.2 Combining SPR and nano rheology

As described in the previous section, the traditional SPR based biomolecule detection scheme is not suitable for the detection of small molecules binding on to a substrate protein. The reason being that proteins are much larger molecules compared to the target molecules and hence binding of the target molecule has a very small effect in the local dielectric constant. As an alternative, we propose a technique in which the change in stiffness of the protein is measured instead of the modification of the dielectric constant when the target molecule binds. The SPR technique is used to probe the stiffness of the protein while the nano rheology setup discussed earlier is used for applying an oscillatory force on the protein.

4.2.1 Improved signal from LSPR in the nano rheology setup

Fig. 4.7 shows the intensity of light scattered from the gold nano particles tethered via the protein as shown in the setup of Fig. 4.1. The excitation source here is the 632 nm laser that excites the surface plasmons. The dashed sinusoidal curve shown in Fig. 4.7 is the voltage applied across the fluid cell and it is of amplitude ~ 375 mV. The solid sinusoidal curve is the AC component of the output voltage of the photomultiplier tube (proportional to the intensity of scattered light from GNPs). This AC component was obtained by recording the output voltage of the PMT with a data acquisition interface and by subtracting the dc component numerically. The amplitude of this solid curve (~ 70 mV) is proportional to the fluctuating component of the intensity of light scattered from the gold nano particles.

Fig. 4.8 shows a graph similar to the one shown in Fig. 4.7 but with the excitation source being the 488 nm laser. The same sample used to obtain the data in Fig. 4.7 is used to obtain this data set with the 488 nm laser excitation. In this case, gold nano particles scatter the evanescent wave to the far field. The dashed curve shows that the applied voltage on the cell is ~ 680 mV and the solid curve shows that the intensity of the fluctuating component of the scattered light from the gold nano particles is around 20 mV (amplitude of solid curve).

This experiment tells that in the SPR mode (with 632 nm excitation), there is a much higher signal to detect when compared to the evanescent wave excitation with the 488 nm laser. If Fig. 4.8 was measured with the same applied voltage as in Fig. 4.7 (375 mV), the fluctuation of the intensity is not measurable unless a lock-in detection is used.

Fig. 4.9 shows a comparison of a frequency response of the enzyme GK performed with the SPR mode and the evanescent wave scattering (EWS) mode. Fig. 4.9 (a) shows the frequency response of GK measured with an applied voltage of 175 mV while Fig. 4.9 (b) shows the frequency response with an applied voltage of 250 mV. All measurements were performed with the same sample. Initially the data for the EWS mode was taken using the 488 nm laser and these are the blue circles in the figure. Then the optics was changed to the SPR mode and the response was measured again (shown in red squares). The y-axis of the graphs show the ratio of the intensity fluctuation, δI, to the overall intensity measured, I_0, and this ratio is independent of the power of the laser. Therefore, the SPR mode has much more dynamic range of the signal when compared with the EWS mode. The black triangles were obtained by multiplying the EWS data in blue circles by a factor ~ 6.

In addition to the improved dynamic range, the overall intensity of the scattered light from the SPR mode is much higher than the EWS with the 488 nm laser. Even though both lasers were roughly operated at the same power, the overall intensity from the SPR mode was about a factor 4 to 5 times higher than the EWS mode. This intensity of scattered light was measured with a photo multiplier tube that had an efficiency factor of about 80 between the two wavelengths. Thus, factoring all considerations, the scattered light from the SPR mode was

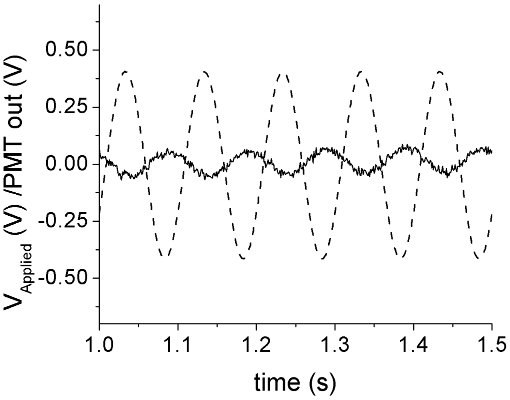

Figure 4.7: Output voltage from the PMT detector with excitation from a He-Ne laser at 632 nm (SPR mode). The dashed line shows the voltage applied across the sample chamber. This electric field drives the negatively charged GNPs into a collective oscillation that modulates the amount of light scattered depending on the distance of the GNPs from the surface. The solid line shows the light detected by the PMT.

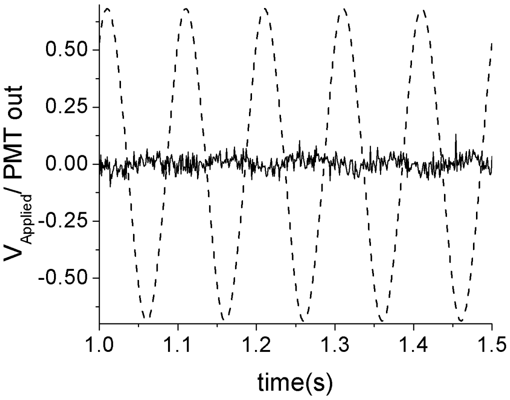

Figure 4.8: Output voltage from the PMT detector with excitation from a 488 nm laser (EWS mode). The dashed line shows the voltage applied across the sample chamber while the solid line shows the light detected by the PMT.

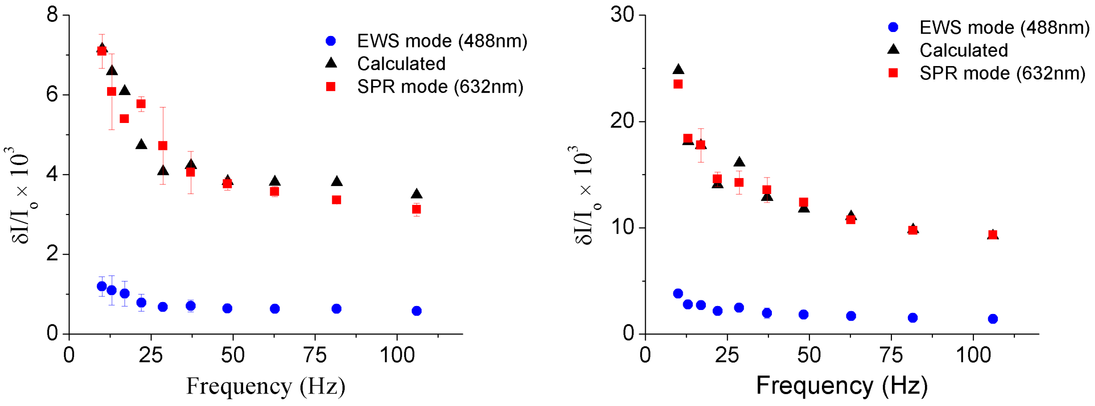

(a) (b)

Figure 4.9: Mechanical response of the enzyme GK for an applied oscillatory force, measured in SPR and EWS modes. Plotted is the amplitude of oscillation δI of the light intensity radiated by the GNPs (normalized by the total light intensity I), which is proportional to the amplitude of the collective oscillation of the GNPs. The frequency dependence of this mechanical susceptibility is characteristic of viscoelasticity [36, 37]. For the same sample, we show measurements obtained in SPR mode (squares; $\lambda = 632\,nm$) and EWS mode (circles; $\lambda = 488\,nm$). The triangles are the same data as the circles, multiplied by the factor $\chi = 6$, showing that SPR mode has a $6\times$ larger dynamic range compared to EWS mode. The amplitude of the applied voltage (proportional to the applied force [36]) is $175\,mV$ for sample (a) and $250\,mV$ for sample (b); the factor $\chi = 6$ is the same in both cases.

about 400 times higher than the EWS mode. The fact that there is a high light intensity is beneficial when designing a commercial biosensor platform.

4.2.2 Detection of small molecules binding to GK

The enzyme Guanylate kinase catalyzes the conversion of GMP to GDP by transferring a phosphate group from ATP. Thus, ATP and GMP are specific substrates for this enzyme. The molecular weight of GK is around 22 KDa while its substrates have a molecular weight of around 0.4 KDa. Thus, the binding of these substrates does not result in a significant change in the dielectric constant, rendering the traditional SPR technique inadequate for the detection of small molecules binding to substrate proteins. However, ATP and GMP bind inside a binding pocket of GK that is thought to perturb the stresses in the molecule significantly. For example, it is known from molecular dynamic simulations that the binding of GMP in this binding pocket causes the enzyme to undergo a conformational change towards a more compact state [64]. Therefore, we used the new SPR enhanced nano rheology scheme to detect the binding of ATP, GMP etc. to GK and to gauge the performance of the new method.

The detection experiments were performed with the setup shown in Fig. 4.1. The 632 nm laser was used at an incident angle close to the θ_{SPR} to excite surface plasmons. Mechanical oscillation of the protein was achieved with a 12 Hz AC signal at an amplitude of around 200 mV. The resulting fluctuation of intensity δI was measured with a lock-in detection while the overall intensity I_0 of the scattered light from the gold nano particles were measured by using a mechanical chopper at 200 Hz. As pointed out earlier, the ratio of $\delta I/I_0$ gives a measure of the displacement of the gold nano particle.

Binding curves for GMP, ATP and CMP (Fig. 4.10) were produced by measuring the response of the protein at 12 Hz for 30 seconds at each concentration of the corresponding nucleotide. A binding isotherm was produced by exchanging the buffer in the fluid chamber with new buffer at different nucleotide concentrations.

Fig. 4.10 (a) shows the binding of GMP to Guanylate kinase. The maximum signal based on the existing SPR based measurement would be $M_{GMP}/M_{GK} \sim 1.5\%$. But as evident from Fig. 4.10 (a), a signal of about $\sim 15\%$ can be observed in the new nano rheology based detection scheme. In addition, we can extract more information about the process when compared with the existing SPR method. The reduction in the deformation amplitude of the protein with increasing GMP concentration implies that the protein stiffens with the binding of GMP.

The binding curves in Fig. 4.10 could be understood in terms of a two state binding isotherm given by

$$\frac{\delta I}{I_0} = \alpha - \frac{\beta}{1 + K_d/[\text{nucleotide}]} \tag{4.20}$$

which is used for fitting the data in all three graphs of Fig. 4.10. In equation 4.20, α and β are normalization constants, K_d is the dissociation constant for the binding and [nucleotide] is the concentration of the nucleotide. The GMP binding curve in Fig. 4.10 (a) can be fitted with $K_d = 4.7\ \mu$M. There are no previously measured values for K_d of GMP binding to Guanylate kinase from *Mycobacterium tuberculosis* (tbGK), but [65] gives a measurement of K_d of GMP binding to yeast Guanylate kinase. This measurements was performed using an NMR based method and the value obtained for $K_{d,GMP}$ is around 30 μM. A direct comparison between the two values is impossible as the catalysis speed of the yeast GK is about 10 times faster than that of tbGK.

Fig. 4.10 (b) shows the binding of Cytidine mono phosphate (CMP) to GK. CMP is not a substrate for GK at low concentrations, but binds to GK at concentrations which are about 1000 times higher than that of $K_{d,GMP}$. The extracted value for $K_{d,CMP}$ is around 2.4 mM. Since CMP was known not to be a substrate of GK, a control experiment was performed using sucrose to test the binding of sucrose to GK (Fig. 4.11). This negative control experiment indeed verified that sucrose does not bind to GK as expected. Fig. 4.10 (c) shows the binding of ATP to GK, and unlike the binding of GMP, the binding of ATP to Guanylate kinase leads to a softening of the enzyme. Measured $K_{d,ATP}$ of ATP binding to GK was 1.2 mM.

4.2.3 Comparison with a fluorescence based detection scheme

As there was no data available to compare the binding constants of the nucleotides to tbGK, an experiment was performed to measure these quantities using a spectroscopic method. This spectroscopic method relied on the tryptophan amino acid residues present in GK. The fluorescence of tryptophan residues change due to the chemical environment around the residues [66] and leads to either changes in fluorescence efficiency or changes in the emission spectrum. The tryptophan fluorescence in tbGK is excited with an absorption maximum at 280 nm while the emission maximum is 340 nm. Experiments showed a spectroscopic signature for both GMP and ATP binding to GK.

Fluorescence of the GK-nucleotide samples were measured with a Hitachi F-2500 fluorescence spectrometer with a quartz cuvette of 3 mm path length. Fluorescence of GK-nucleotide samples were measured with similar buffer conditions to that used in the SPR-nano rheology detection experiment (3 times diluted SSC buffer) with 0.21 μM enzyme concentration.

Fig. 4.12 shows the change in fluorescence intensity of the GK sample with increasing GMP concentration. The initial rise in fluorescence can be attributed to an effect from GMP binding. This effect could either be due to the conformational change of GK or due to an interaction of the tryptophan residue with GMP.

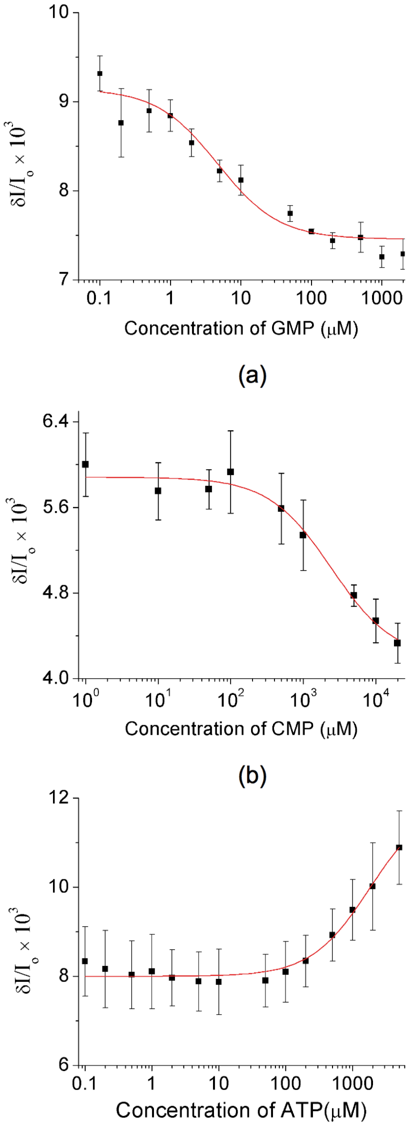

(a)

(b)

(c)

Figure 4.10: Binding isotherms measured by SPR enhanced nano-rheology. The signal is the amplitude of oscillation of the light intensity plotted vs. ligand concentration for a fixed forcing frequency (12 Hz). The lines are fits using the equation 4.20. (a) Binding of the substrate GMP is detected through the stiffening of the enzyme, with a dynamic range of the signal of $\sim 15\%$. The fit gives $K_d = 4.7\mu M$ for the dissociation constant. (b) CMP (not a substrate) also binds at sufficiently high concentration ($K_d \approx 2.4mM$). (c) Binding of the substrate ATP ($K_d = 1.2mM$) leads to a softening of the enzyme, in contrast to (a).

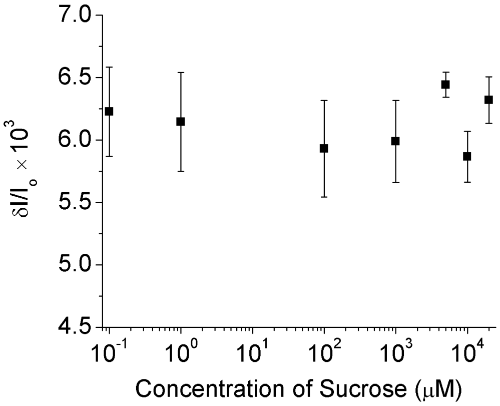

Figure 4.11: Titration curve for sucrose binding to Guanylate Kinase, using SPR enhanced mechanical detection. The signal is constant within experimental error up to sucrose concentrations $\sim$ 10 mM, i.e. no signature of binding is detected in this concentration range, as expected.

Beyond 10 μM GMP concentration, there seems to be a decrease in the fluorescence intensity. This effect is due to the absorption of 280 nm excitation light by the nucleotide GMP. As discussed later, a correction can be done to account for the absorption by the nucleotide.

Fig. 4.13 shows the fluorescence intensity of GK against the concentration of ATP. The fluorescence intensity remains flat till about 100 μM and drops beyond that. This drop can be either due to an actual signal of ATP binding or could be the result of absorption of excitation light by ATP or a combination of both. Both fluorescence measurements suffer from the absorption of excitation light from the nucleotide. Therefore a correction must be introduced to extract information about the binding process. The first step is to measure the actual abortion by each nucleotide in a separate experiment.

Absorbance measurements were performed with a Beckman DU640 spectrometer using a quartz cuvette with an optical path length of 1 cm. Nucleotides were dissolved in 3 times diluted SSC buffer. Fig. 4.14 shows the measured absorbance

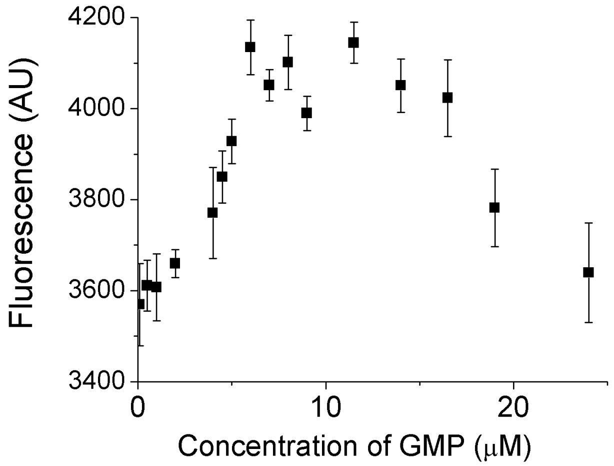

Figure 4.12: Spectroscopic detection of GMP binding to Guanylate Kinase in solution using tryptophan fluorescence. The initial increase in fluorescence is the signature of binding. The drop in fluorescence intensity beyond 10 μM GMP is due to the absorption of the UV excitation light by GMP.

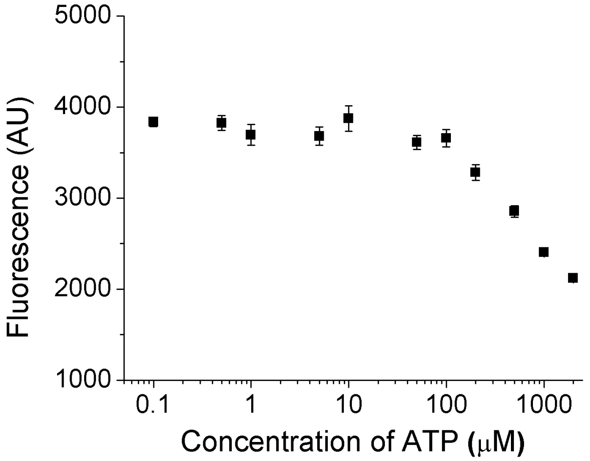

Figure 4.13: Fluorescence measurements for ATP binding to GK. Measurements were performed in SSC/3 with 5 mM Mg^{+2} added (same buffer conditions as for the nano-rheology measurements). The decrease in the signal beyond 100 μM ATP concentration is due to the absorption of the excitation light by ATP.

against concentration of GMP. A clear increase in absorbance is seen after 10 μM and this can explain the decrease in fluorescence beyond 10 μM in Fig. 4.12. The fit in the absorbance curve is produced by a linear regression.

Fig. 4.15 shows the absorbance of 280 nm light by ATP. The absorbance measurement from the spectrometer is $-\log_{10}$ of the relative intensity. The absorbance can be seen to increase rapidly after about 100 μM and the absorbance increases by about 1000 fold at an ATP concentration of about 1 mM. Therefore a correction must be introduced to counter the effect of absorption of the excitation light. The experimentally measured florescence intensity F of an enzyme sample is given by equation 4.21.

$$F = \int_0^l \alpha I(x) dx \tag{4.21}$$

In the equation for the intensity F, α is a factor with dimensions of inverse length, l is the optical path length of the cuvette (3 mm) and $I(x)$ is the intensity of the excitation light (280 nm) at position x. Due to the homogeneity of the solution inside the cuvette, the UV light is uniformly absorbed. This leads to an exponential decay of the excitation light intensity inside the cuvette.

$$I(x) = I_0 e^{-\frac{x}{\delta(c)}} \tag{4.22}$$

Equation 4.22 gives the exponential decay of intensity inside the cuvette, where I_0 is the intensity of 280 nm light at the beginning of the optical path and $\delta(c)$ is the attenuation length scale of 280 nm light which is a function of the nucleotide concentration. Substituting for I_x in equation 4.21 from equation 4.22 and evaluating the integral gives the equation

$$F = \alpha I_0 \delta(c)[1 - e^{-\frac{l}{\delta(c)}}] \tag{4.23}$$

for the measured fluorescence intensity of a sample. A separate absorbance measurement can be used to determine $\delta(c)$. The absorbance measured from an absorbance spectrometer, $\epsilon(c)$, is related to the incident light intensity and the transmitted light intensity with the relation

$$\epsilon(c) = \log_{10} \frac{I_0}{I(L)} \tag{4.24}$$

, where L is the optical path length of the cuvette used to perform the absorbance measurement. $I(L)$ can be eliminated from equation 4.24 by using $I(x)$ with $x = L$ from equation 4.22. This procedure gives $\epsilon(c)$ as

$$\epsilon(c) = \frac{L \log_{10}(e)}{\delta(c)}. \tag{4.25}$$

Thus, by performing an absorbance measurement at each concentration, its possible to find $\delta(c)$ experimentally. This value for $\delta(c)$ can be used to calculate the correction factor $\delta(c) \cdot [1 - e^{-\frac{l}{\delta(c)}}]$. Dividing equation 4.23 with this correction factor removes the effect of absorbance and will yield the change in fluorescence solely due to binding effects. The correction factor for the GMP titration varies from 3.3 to about 4.2 while the correction factor for the ATP titration varies from 3 to about 10.

Fig. 4.16 shows the absorbance corrected fluorescence of GK measured at different concentrations of GMP. The data in fig. 4.12 was used to generate this absorbance corrected plot. The decrease in fluorescence seen in figure 4.12 due to absorbance by GMP is not present after the correction. The red line is a fit produced from the single site binding equation 4.20 and the value for the dissociation constant K_d is ~ 5.1 μM. The value obtained from the nano-rheology method ($4.7\,\mu M$) is very close to the value determined from the fluorescence-based technique.

Fig. 4.17 shows the absorbance corrected fluorescence of the ATP titration. The decrease in fluorescence in figure 4.13 around 100 μM has been lifted after the correction. The measured value for K_d is 1.6 mM from the single site binding isotherm fitted in figure 4.17, which shows good agreement with the measured value from the nano rheology technique (1.2 mM).

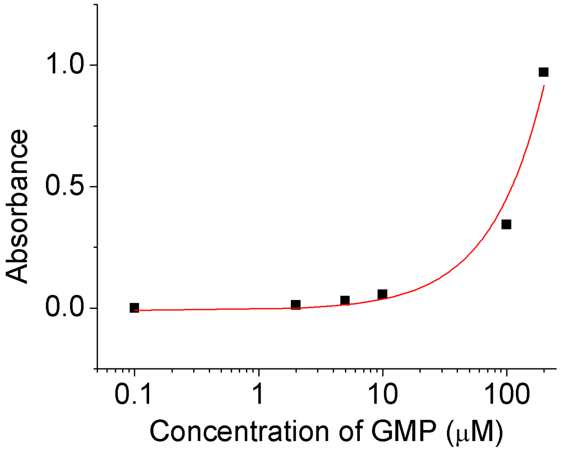

Figure 4.14: Absorbance of 280 nm light by GMP. In the geometry of the spectrometer, the absorbance becomes significant beyond GMP concentrations of 10 μM (the absorbance scale is logarithmic). The red line is a linear regression between concentration and absorbance.

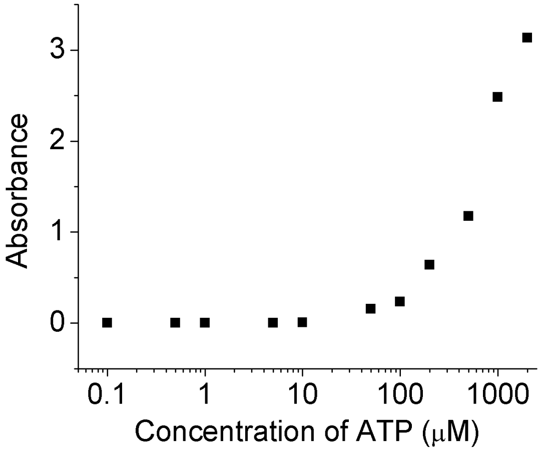

Figure 4.15: Absorbance of 280 nm light by ATP. The absorbance is prominent beyond $\sim$ 100 μM ATP concentration.

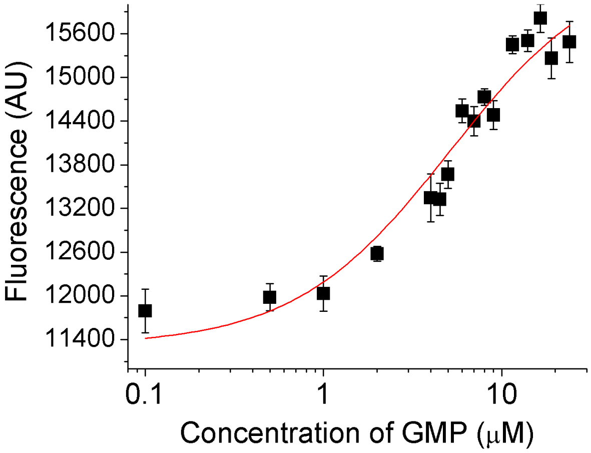

Figure 4.16: Fluorescence measurements of GMP binding to GK (same data as Fig. 4.12), corrected for absorbance of the excitation light, using the measurements of Fig. 4.14 as explained in the text. The line is a fit to the single site binding isotherm giving the value $K_d \approx 5.1\,\mu$M for the dissociation constant.

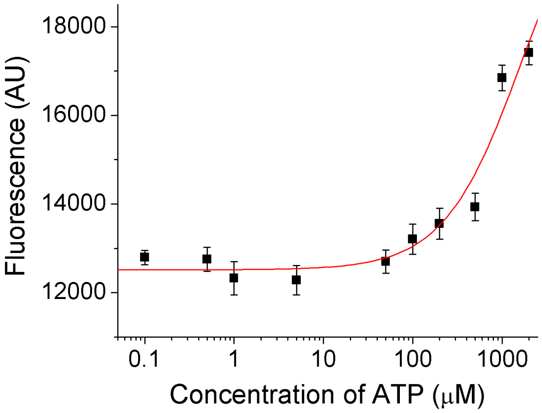

Figure 4.17: Fluorescence signature of ATP binding to GK (same data as Fig. 4.13), corrected for ATP absorbance using the measurements of Fig. 4.15. The line is a fit to the binding isotherm and returns the value $K_d \approx 1.6$ mM, in good agreement with the value from the nano-rheology method (1.2 mM).

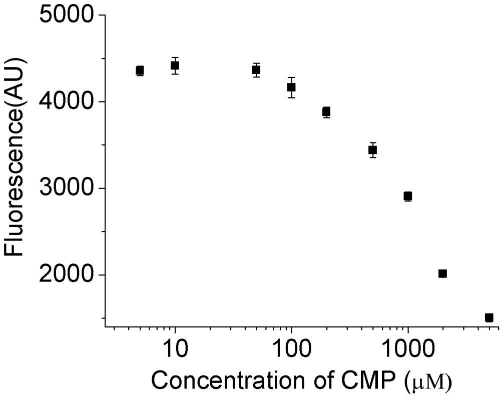

Figure 4.18: Titration curve of CMP binding to GK. The large decrease in fluorescence is due to the absorption of UV light by CMP making it difficult to extract information about binding of CMP to GK from these fluorescence measurements.

A similar titration curve was obtained for CMP (Fig. 4.18), where a monotonic decrease in fluorescence can be seen due to the absorption of 280 nm light by CMP. In this case, the correction factor is so large that it is difficult to extract a reliable value for the binding constant of CMP to GK.

4.3 Future work

The biosensor described here can have many clinical advantages, however, more work is required to have a system that is of practical interest. One area of improvement is to use DNA aptamers [67]. DNA aptamers can bind to very specific target molecules and form secondary structures. Currently there are many aptamers specifically designed to bind many molecules of interest such as cocaine, dopamine etc. [68]. Many research groups have been working in this area and there are different promising technologies for aptamer-based sensors [69, 70, 71, 72].

DNA aptamers can be used in conjunction with the nano rheology based technique that we propose. Usually the aptamer is in a random coil configuration before the target-binding event. After the target molecule binds on the aptamer, the DNA forms secondary structures such as hair pins. This effect can change the stiffness of the DNA molecule by a large amount. Thus, by probing the stiffness of the aptamer with the nano rheology setup, a large signal can be obtained corresponding to target molecule binding.

Another direction in which this technique can be advanced is by including the ability to detect many bio molecules simultaneously. A chip can be fabricated with small pixels containing different substrate molecules. The light intensity from each pixel can be used to calculate the change in stiffness of each substrate. A small sample volume in the order of a few micro liters corresponding to a drop can cover an array of pixels, giving the ability to detect many molecules with a very small sample volume.

CHAPTER 5

An artificial axon

In this chapter I will outline the design of a setup to realize an artificial axon. Analogous to the actual axon, the artificial axon is composed of voltage gated ion channels in a lipid bilayer. Such a system can have many advantages over the actual system in a research or demonstration environment. The artificial axon can be more robust for different environmental conditions such as temperature or can be customized with genetically modified ion channels. By using techniques from micro/nano fabrication, its possible to pattern a scaffolding on which an artificial axon can be realized, and this allows the possibility of complex systems.

I will give a brief introduction to the action potential and signal propagation in neurons before elaborating on the actual experiment.

5.1 Basics of neural signal propagation

The action potential is an all or none response. If the axon is excited below a certain threshold voltage, no action potential is generated whereas for excitations above the threshold voltage, an action potential is generated which travels along the axon. Signal propagation in a neuron is a relaxation wave in which the membrane potential suddenly switches from the resting potential of ~ -70 mV to a voltage of ~ 40 mV and returns back to the resting potential. The time scale of this process is of the order of a few milliseconds. An important concept when talking about the action potential is the concept of the Nernst potential. The following section gives an account of the Nernst potential.

5.1.1 The Nernst potential

The Nernst potential is the potential difference created across the lipid membrane due to a charge imbalance. There are two requirements to create the charge imbalance. One of them is that there should be a gradient of salt concentration on either side of the membrane. For example one side of the membrane can have 150 mM KCl whereas the other side could be 20 mM KCl. The other requirement is a semi-permeable ion channel which only allows either K^+ ions or Cl^- ions to pass through (selective permeability).

Due to diffusion, the ionic species will migrate from the higher concentration side to the lower concentration side. But, since only K^+ (or Cl^-) ions are allowed to cross the membrane; there will be a net charge build up on either side of the membrane. This charge build up will create an electric field that opposes the diffusion of ions and the system reaches a steady state. Nernst potential is the potential difference across the membrane in this steady state.

An expression for the Nernst potential can be derived by considering the chemical potential of potassium ions on each side. Consider a lipid bilayer (with potassium selective ion channels) separating two KCl solutions. The chemical potential of potassium ions on side 1 is $\mu_1 = \mu_0 + k_B T \ln(c_1) + eV_1$ while that of side 2 is $\mu_2 = \mu_0 + k_B T \ln(c_2) + eV_2$. μ_0 is the standard chemical potential for potassium ions, k_B is the Boltzmann constant ($k_B = \mathrm{R}/\mathrm{N_A}$ where $\mathrm{N_A}$ is the Avogadro number and R is the universal gas constant), T is the absolute temperature, c_i is the concentration of KCl in i^{th} side and e is the electronic charge. Assume that side 2 is grounded ($V_2 = 0$ V) and V_1 is the potential of side 1 with respect to side 2.

Due to the permeability of potassium ions through the ion channels, an equilibrium is reached with respect to the potassium ions. At equilibrium, the chemical potential on either side is equal, $\mu_1 = \mu_2$. This gives the expression for the Nernst potential as,

$$V_1 = V_{Nernst} = \frac{k_B T}{e} \ln\left(\frac{c_2}{c_1}\right) \tag{5.1}$$

Since Cl^- ions cannot permeate the membrane, they are out of equilibrium and does not contribute to the Nernst potential.

In the presence of another ionic species, sodium for example, equation 5.1 takes a different form where the Nernst potential of each species is weighted by its relative permeability.

5.1.2 Propagating signals in the axon

A sketch of a model axon is shown in Fig. 5.1. The real axon has a lipid bilayer in the shape of a tube with embedded ion channels. The bilayer is impermeable (almost) to the sodium and potassium ions that are the current carriers in this cable. In the figure 5.1, only a cross-sectional view of the tube shaped bilayer is depicted. The gradient of sodium and potassium ions cross the membrane can form a Nernst potential as discussed in previous section.

In this simplified model, let us model the ion channels to be ohmic, which implies that the net current through these channels is simply the net voltage across them times the conductance. The effective resistance of all the channels is modeled as r_{ch} per unit area. V_N is the effective Nernst potential across the bilayer due to the concentration gradient of ions. The interior of the axon is a hollow tube filled with solution with a small radius (even the giant axons are $\sim$ 0.5 mm). Due to this small radius, the interior represents a significant electrical resistance for currents compared with the extracellular environment. Therefore, the exterior solution is modeled as having a zero resistance for ionic currents whereas the interior of the axon is modeled to have a conductivity k. c_m is the capacitance of the membrane per unit area. The radius of the model axon is a.

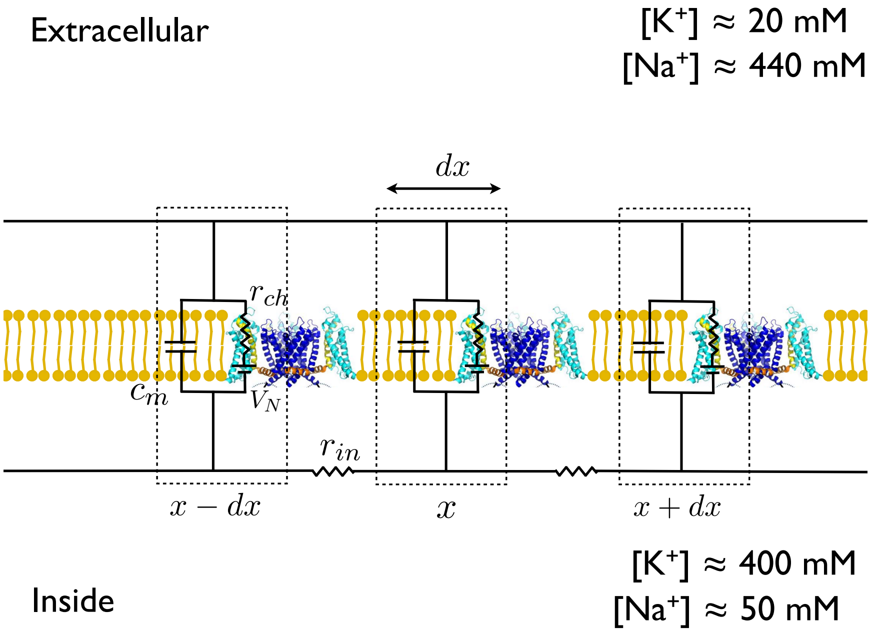
Extracellular
[K⁺] ≈ 20 mM
[Na⁺] ≈ 440 mM
dx
r_{ch}
c_m
V_N
r_{in}
$x - dx$
x
$x + dx$
Inside
[K⁺] ≈ 400 mM
[Na⁺] ≈ 50 mM

Figure 5.1: A simplified axon model. The figure shows the extracellular medium and the intracellular medium separated by the lipid bilayer (containing ion channels). The equivalent electrical circuit is shown on the same diagram. c_m is the capacitance of the lipid bilayer per unit area, r_{ch} is the resistance of the ion channels per unit area and V_N is the Nernst potential across the membrane. The real axon can be considered a hollow tube, thus the area of the dx element is $dx \cdot 2\pi a$ where a is the radius of the axon.

Let $I(x)$ be the current entering the element at position x in the intracellular side. The current that flows outward to the extracellular fluid is given by $I(x) - I(x + dx)$. This outward current has two components, a capacitive current and an ionic current through the channels. The capacitive current is simply $c_m \cdot A \cdot dV/dt$ where A is the area of the element $(A = dx \cdot 2\pi a)$ and V is the voltage inside the axon at point x. The ionic current through the channels is assumed to be ohmic in this simplified model and is given by $(V(x) - V_N)A/r_{ch}$.

This gives the relation

$$I(x) - I(x + dx) = c_m \cdot A \cdot \frac{dV}{dt} + \frac{A \cdot (V(x) - V_N)}{r_{ch}} \tag{5.2}$$

for the conservation of current in the axon. The current in the axon can be related to the resistance inside the axon (r_{in}) by

$$I(x) = -\frac{V(x + dx) - V(x - dx)}{r_{in}} \tag{5.3}$$

and the resistance r_{in} is related to the conductance of the solution by $r_{in} = (\pi a^2 k)/dx$. Combining all this gives the cable equation for this simplified model as

$$\pi a^2 k \frac{d^2V}{dx^2} = 2\pi a \left(\frac{(V(x) - V_N)}{r_{ch}} + c_m \frac{dV}{dt} \right) \tag{5.4}$$

This equation can be solved to obtain the solution to the voltage at point x and time t as

$$V(x,t) = \frac{B \cdot e^{-t/\tau} e^{-x^2 \tau/(4t\lambda_{axon})^2}}{\sqrt{t}} + V_N \tag{5.5}$$

, where $\lambda_{axon} = \sqrt{akr_{ch}/2}$ and $\tau = cr_{ch}$.

Equation 5.5 does not represent traveling wave solutions. In fact, this solution represents a diffusive spread. When the neuron described by the above model is excited at a point, the voltage pulse decays as it spreads in a length scale given by λ_{axon}. By using standard values for a squid axon, $a \approx 0.5$ mm, $k \approx 3\ \Omega^{-1}\text{m}^{-1}$

and $r_{ch} \approx 0.2\ \Omega\text{m}^2$, the value for λ_{axon} can be approximated as 12 mm. The reason behind the failure of the model is the assumption that the ion channels behave as ohmic devices. In fact, it is well known that these show gating behavior as discussed in previous chapters, channels remain closed below certain voltages while remain open above depolarizing potentials.

A qualitative understanding of signal propagation can be gained by considering the gating of channels. In the resting state, potassium channels have a higher conductance than the sodium channels, forcing the Nernst potential closer to that of potassium, around -70 mV. When the axon is depolarized, the conductance of both channels increases, but the sodium channels respond on a much faster time scale than the potassium channels. Thus, the result is that, after depolarization, the conductance of sodium channels dominates, pulling the Nernst potential close to that of sodium ($\sim +40$ mV). The eventual inactivation of sodium channels and opening of potassium channels brings the voltage again close to the Nernst potential of potassium. This process is essentially the action potential.

The model axon discussed earlier showed that a voltage spike can travel a distance λ_{axon} (12 mm for squid axon) before its amplitude has fallen to $1/e$ of the original value. Thus, the voltage spike generated by momentarily switching the Nernst potential can travel a certain distance to excite neighboring regions along the axon. Even though the excitation at the second point (due to the action potential at the initial site) will have a lower voltage than at the initial site, the opening of the channels at the second site guarantees that the membrane potential will reach the Nernst potential of sodium, regenerating the amplitude of the action potential.

This behavior can be realized qualitatively by using the exact form of the voltage gating for the ionic current through the channels. [73] gives an account of the travelling wave solutions using an approximate form of gating where the conductance is quadratic in the applied voltage while the original treatment done by Hodgkin and Huxley with the actual form of the gating is given in [74].

5.2 Experimental approach for the artificial axon

The real axon has two types of ions to initiate the action potential spike. One can regard the role of potassium channels in the real axon as to bring the Nernst potential back to the resting value. This hints that in order to realize an artificial axon, it is not required to have both potassium and sodium channels. However, both channels are required in order to have the same pulse shape and behavior as the real action potential. This experiments used only potassium channels to develop an artificial signal propagation system. The following sections outline different experiments performed to understand how to realize an artificial axon.

5.2.1 Single well system to control Nernst potential

This experiment was designed to test whether having a concentration gradient across the lipid bilayer can generate a measurable Nernst potential. The specific questions that we wanted to address was (1) whether it is possible to generated a measurable Nernst potential by simply having a concentration gradient? (2) how to effectively create a concentration gradient across the bilayer considering that any osmotic stress on the bilayer can result in unstable bilayers? (3) how many ion channels are required to see a Nernst potential? and (4) how to measure the Nernst potential?

To answer these questions, an experimental setup was built as shown in Fig. 5.2, similar to the setup used in chapter 2. The setup consisted of electronics to perform a voltage clamp experiment and electronics to measure voltage of the buffer. Ag/AgCl electrodes were used as working electrodes. In addition, the voltage-clamping electrode was allowed to float with a solid-state relay that was controlled via software. The voltage measurement was performed with an op-amp with sub-pico-ampere input bias current and it was used in the high impedance, non-inverting amplifier configuration.

The experimental approach to setup a concentration gradient of potassium ions across a lipid bilayer with KvAP ion channels is as follows. Two buffers were used in the electrophysiology experiment, one was 150 mM KCl (with 10 mM HEPES and pH 7.4) and the other was at a lower potassium concentration of 30 mM (10 mM HEPES, 240 mM Sucrose at pH 7.4). The concentration of the small chamber (intracellular) was lowered keeping the extracellular compartment at 150 mM. Initially both chambers were filled with 150 mM buffer. After successful incorporation of ion channels (which is verified by applying depolarizing pulses at 60 mV and observing the ionic current) the buffer in the intracellular chamber was gradually exchanged in steps of about $\sim 100\ \mu$L with the 30 mM KCl buffer using a pipette. It was found that sudden flows can lead to the bursting of the bilayer and this can be partially rectified by applying the new buffer solution along the walls of the inner tube instead of directly positioning the pipette tip inside the solution.

As shown in Fig. 5.3, when the switch S1 is closed, i.e. the setup is in the voltage clamp mode, the recorded potential of the 2^{nd} electrode is always equal to the clamping voltage (in the presence of a lipid bilayer between the two chambers). This is true even when there are channels and when there is a concentration gradient of potassium ions. But an interesting phenomenon occurs when the switch S1 is opened suddenly. The measured voltage from the 2^{nd} electrode suddenly jumps to the Nernst potential of the system and remains roughly close to the Nernst potential. This effect is depicted in Fig. 5.4 and it shows that we can indeed measure the Nernst potential in this model setup.

The number of channels reflected on how fast the measured voltage in the intracellular chamber rose from the holding voltage (~ -120 mV) to the Nernst potential upon releasing S1. The rise time decreased with increasing number of

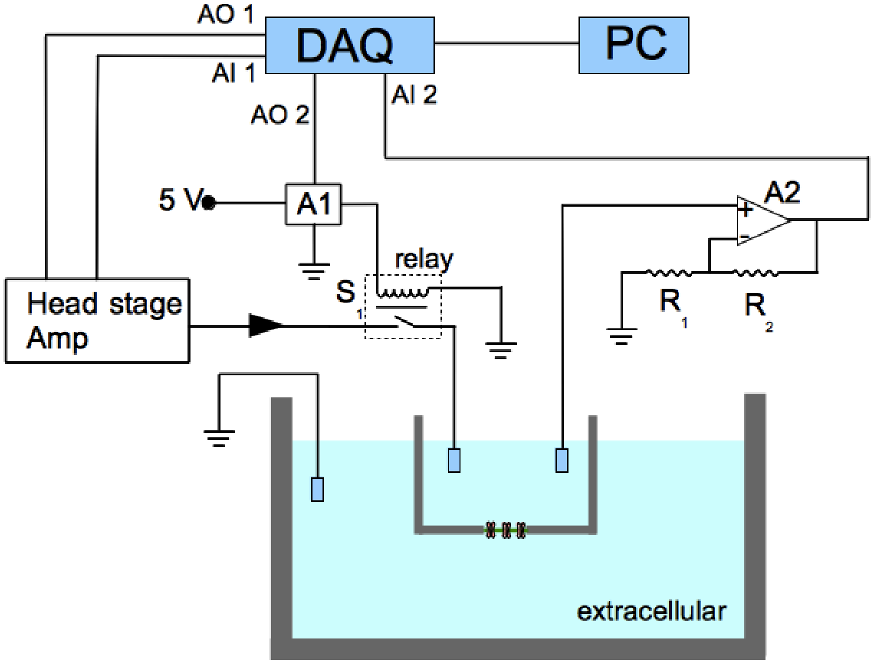

Figure 5.2: The one well system to study Nernst potential. The head stage amplifier is connected to the Ag/AgCl electrode via a solid-state relay S_1. This relay is driven by the driver IC A1 (BSP 75N) and analog output channel 2 (AO 2) of the DAQ controls the relay. The voltage in the top chamber is recorded with a separate Ag/AgCl electrode using a high input impedance amplifier. The amplifier is constructed with the op-amp A2 (AD795) in the non-inverting configuration. R_1 and R_2 were set at 10 KΩ and 100 KΩ to have a gain of 11. The data acquisition system (DAQ) was connected to the computer (PC) and runs custom software to control the solid-state relays and record signals.

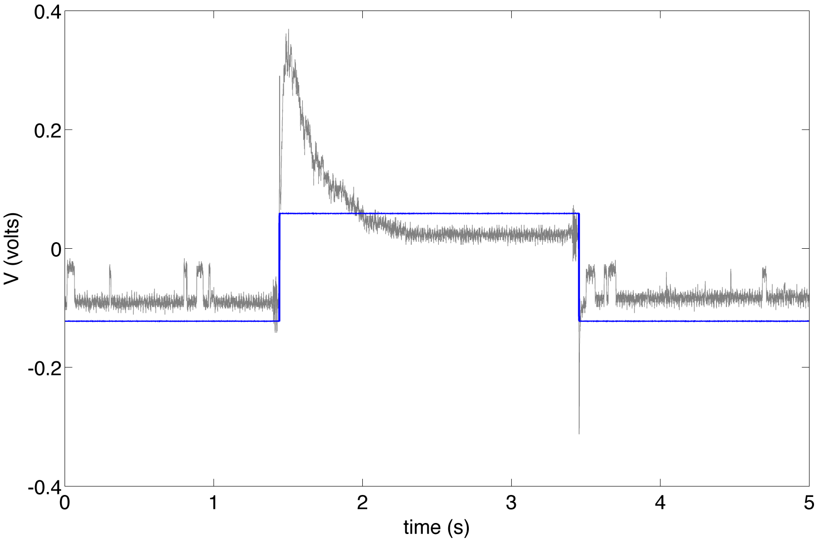

Figure 5.3: The voltage measured in the buffer using an independent electrode under voltage clamping conditions. The blue curve is the experimentally measured voltage with the high input impedance voltage amplifier shown in Fig. 5.2 while the grey curve is proportional to the current delivered to the system with the head stage amplifier. Initially the voltage is clamped at -120 mV where the channels are mostly closed. Stepping the potential to 60 mV at ~ 1.5 s opens the channels stochastically which is seen in the current trace.

channels. In addition, Fig. 5.5 shows the measured voltage when there are no channels in the lipid bilayer. The voltage essentially stays at the holding potential even after floating the clamping electrode. This can be understood as a measurement of voltage of a charged capacitor, the capacitor being the lipid bilayer.

In order to use this voltage spike from the Nernst potential in a model axon, it must be able to drive a certain load. The voltage spike measured in Fig. 5.4 is an open circuit measurement. An experiment was performed to test whether the ion channels can produce the same voltage spike in the presence of a load. The load was chosen to be a series RC circuit as this simulates a lipid bilayer that is

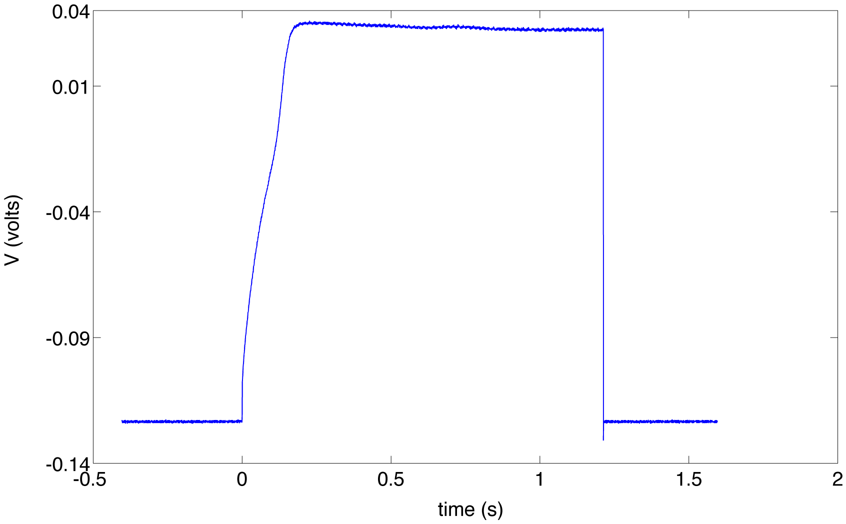

Figure 5.4: The voltage measured in the buffer upon releasing the voltage clamp. The measurement was taken with the setup shown in Fig. 5.2. Initially, the membrane voltage is clamped at -120 mV and the clamping is released at 0 s. After that, the membrane voltage rises rapidly to the Nernst potential of the system (~ 35 mV).

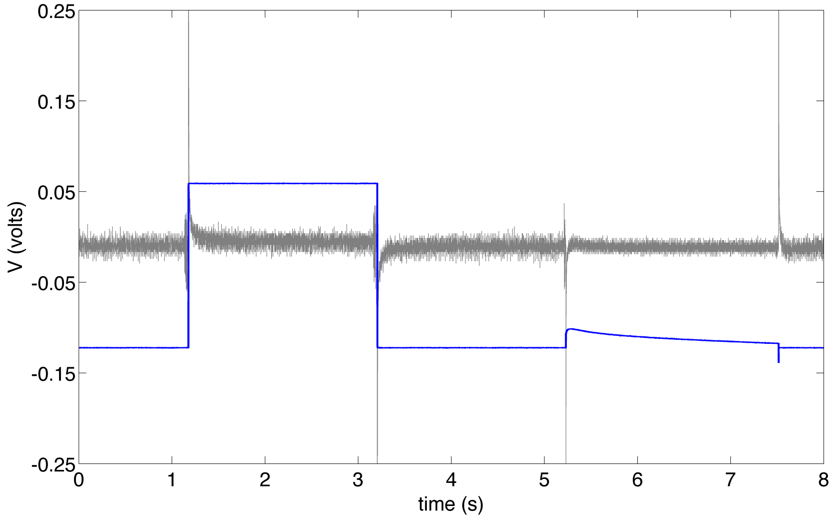

Figure 5.5: The voltage measured in the buffer upon releasing the voltage clamp when there are no channels in the lipid bilayer. The blue curve is the experimentally measured voltage in the upper chamber using the high impedance voltage amplifier and the grey curve is the output from the head stage amplifier (proportional to the current delivered to the top chamber by the head stage amplifier). The membrane potential is initially held at the holding voltage of -120 mV and stepped to 60 mV for 1.2 s. During this time, there is almost no current (except for a capacitive transient and a very small leakage current). This shows us that there are no channels in the bilayer. At around 5.25 s, the clamping electrode is released. The membrane potential rises by a small amount and decays back to -120 mV exponentially. This is in contrast to the behavior in Fig. 5.4.

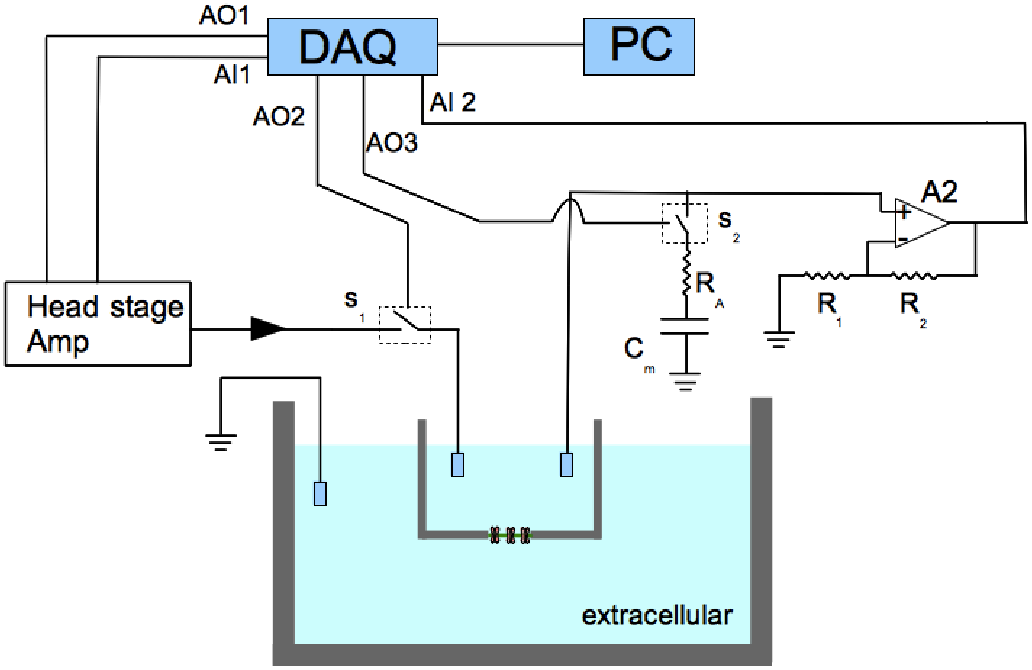
AO1
DAQ
PC
AI1
AO2
AI 2
AO3
A2
+
-
S
2
R
A
R
1
R
2
C
m
Head stage
Amp
S
1
extracellular

Figure 5.6: One-well system to study the Nernst potential with an added impedance. A capacitive load, C_m, corresponds to the lipid bilayer of the 2^{nd} well and R_A is the access resistance for the electrodes in the 2^{nd} well. S_2 is a solid-state relay to enable measurements with and without the load from the same system. The load capacitor $C_m = 60$ pF and $R_A = 10$ KΩ. R_2 and R_1 were set at 100 KΩ and 10 KΩ to have a gain of 11.

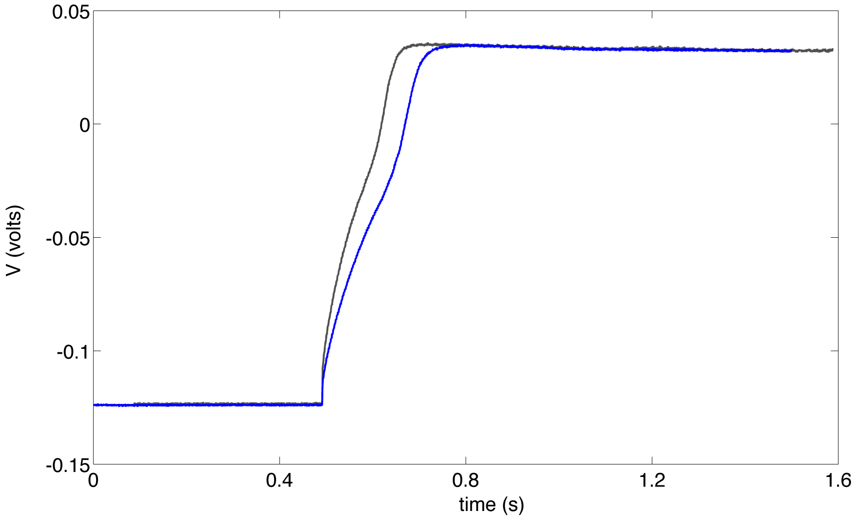

Figure 5.7: Influence of an external RC load to the Nernst potential spike. These curves were generated with the setup shown in Fig. 5.6 where a capacitive load was connected to represent the effect of a cascaded 2^{nd} well. The voltage clamp was released at around 0.5 s and this results in the membrane potential spiking to the Nernst potential of the system ($\sim$ 40 mV). The effect of the load is to delay the rise time of the potential.

electrically connected to the first lipid bilayer.

Fig. 5.6 shows the experimental setup to record the Nernst potential with the presence of a load. In the figure, $\mathrm{R_A}$ is a resistor to represent the access resistance in the buffer solution and $\mathrm{C_m}$ is the capacitance of a lipid bilayer. The experiment was performed with $\mathrm{R_A}$ = 10 KΩ and $\mathrm{C_m}$ = 60 pF. Switch S2 was controlled with the computer and voltage measurements were performed with and without the impedance. Fig. 5.7 shows the effect from the added load, and it is clear that the ion channels can produce the voltage spike even with an added impedance. However, the added impedance delays the voltage spike by about 100 ms.

5.2.2 The two-well system

By using a single-well system, it was demonstrated that a voltage spike can be generated from a holding potential to the Nernst potential. The next step in the experiment to construct the model axon is to develop a two-well system, which can show the propagation of the Nernst potential spike from the 1^{st} well to the 2^{nd} well. Fig. 5.8 shows the experimental setup for a 2-well system. Each well is bathed in the same extracellular fluid but from the intracellular side, they are connected by a RC circuit to represent the resistance in the fluid inside the axon(R_{in}) and the capacitance of the lipid bilayer (c_{in}). Each well can be voltage clamped separately to measure the ion channel activity. In addition, the potential of each well is measured via a high impedance voltage amplifier.

5.3 Micro-machined approach

In order to realize complicated systems that can be used for studying new phenomena, a better system is required. Adding more than 3 wells in the previously discussed system is prohibitively complicated. As a way around this problem, I developed the foundation for a system that is constructed from micro fabrication techniques. The advantage of this approach is that the geometry of the device can be reduced to the micron scale. In the previous model system, the lipid bilayer was painted on an aperture of around $\sim 200\ \mu$m in diameter. In the micro machined approach, the lipid bilayer is painted over micro machined apertures on a thin silicon nitride membrane. These apertures can be fabricated as small as 1 μm using UV photolithography. Silicon nitride was used as the membrane to fabricate the apertures due to its inert properties and its mechanical stability.

Fig. 5.9 shows a cross-sectional diagram of the micro-machined approach for realizing an artificial axon. The device is constructed on a glass slide. Polydimethy siloxane (PDMS) is used to create the buffer chambers and fluid channels. As

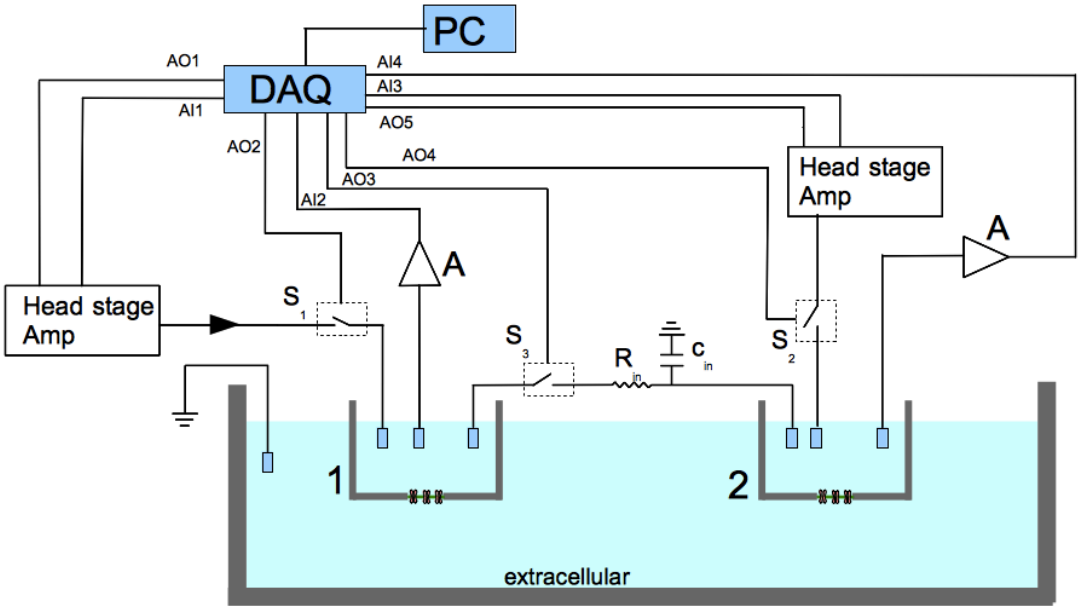
PC
DAQ
AO1
AI1
AI4
AI3
AO5
AO4
AO2
AO3
AI2
A
Head stage Amp
S 1
S 3
R in
c in
S 2
Head stage Amp
A
1
2
extracellular

Figure 5.8: A two-well system to demonstrate the propagation of the Nernst potential spike. S_1 and S_2 are two solid state relays controlled by software. They are used to float the voltage clamping when required. A is a high-impedance voltage amplifier built with an operational amplifier. S_3 is a solid-state relay to isolate well 1 and 2 initially. c_{in} represents the capacitance of the axon between the two wells and R_{in} is the resistance of the intracellular medium between the two wells. The head stage amplifiers are used initially to verify the presence of ion channels in each well. Once channels have been incorporated successfully in each well, S_2 is left open and S_3 is closed. A pulse is initiated by releasing S_1 momentarily.

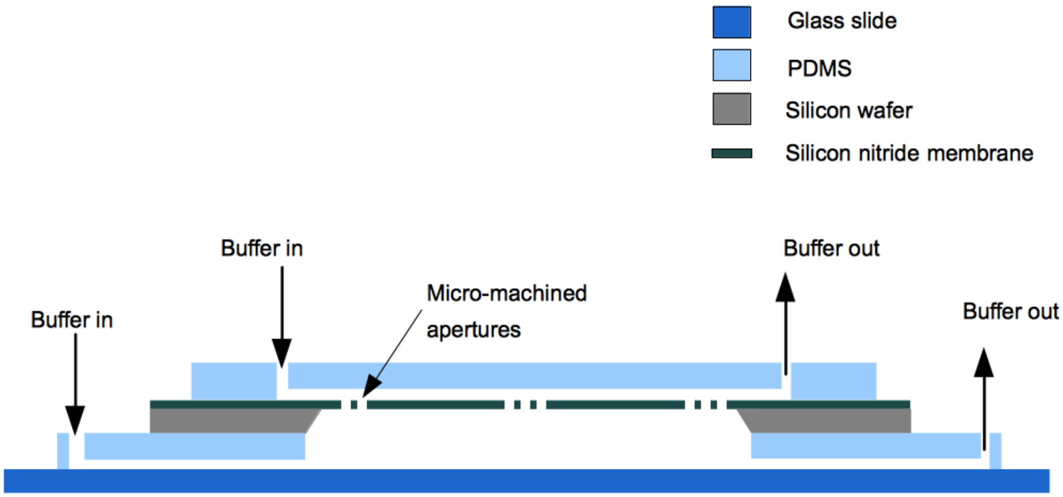
Glass slide
PDMS
Silicon wafer
Silicon nitride membrane
Buffer in
Buffer out
Micro-machined apertures
Buffer in
Buffer out

Figure 5.9: Schematic diagram of the micro-machined system to realize a synthetic axon. Two fluid compartments (fluid channels) are separated by a thin silicon nitride membrane. The top channel corresponds to the interior of the axon. The thin membrane has small apertures to support a lipid bilayer. Ion channels are incorporated in these lipid bilayers to establish the Nernst potential and propagate signals. Fluid channels are fabricated with the elastomer Polydimethy siloxane and the silicon nitride membrane is fabricated on a silicon chip.

shown in the figure, a PDMS layer is bonded on the glass slide. This PDMS layer has channels for buffer exchange. The silicon wafer containing the thin silicon nitride membrane is then bonded on the PDMS layer. Finally another PDMS layer is bonded on top of the silicon nitride layer to form the top chamber with fluid exchange channels. Ag/AgCl electrodes can be patterned on the silicon nitride membrane and micro machining techniques allow for fabrication of electrodes as small as $\sim 1\ \mu$m. The lipid bilayer is painted by passing a droplet of lipid in the upper channel. The following sections outline the fabrication process in detail.

5.3.1 Fabricating the thin silicon nitride membrane with micron scale apertures

Double side polished, [100] test grade silicon wafers of 3-inch diameter and 400 μm thick were used as carrier wafer for the silicon nitride membranes. Fig. 5.10 shows the process I used to fabricate a free standing silicon nitride membrane [75]. This process is based on the well established anisotropic etching of silicon by KOH [76]. The anisotropy is due to the difference in reaction rates for different crystallographic planes. Therefore, using [100] oriented Si wafers is important for the producing these freestanding silicon nitride membranes.

A Si wafer was cleaned thoroughly with hot piranha (1:5 H_2O_2:H_2SO_4 at 80 °C) for 30 minutes followed by acetone sonication and DI water rinsing. The wafer was then dried and coated with a 400 nm thick low stress silicon nitride layer on both sides using a Plasma Enhanced Chemical Vapor Deposition tool (Unaxis PECVD). The deposition rate was set at 12 nm/minute. This is illustrated in Fig. 5.10 (b). Fig. 5.10 (c) shows the next step of depositing a protective gold coating. Au is deposited with an e-beam deposition system (CHA Mark 40). An adhesion layer of 30 nm Cr was deposited prior to the 50 nm protective Au layer. Fig. 5.10 (d) shows the subsequent pattering of the Au layer (and the underlying Cr) with UV photolithography. AZ 4620 photoresist was used for patterning of

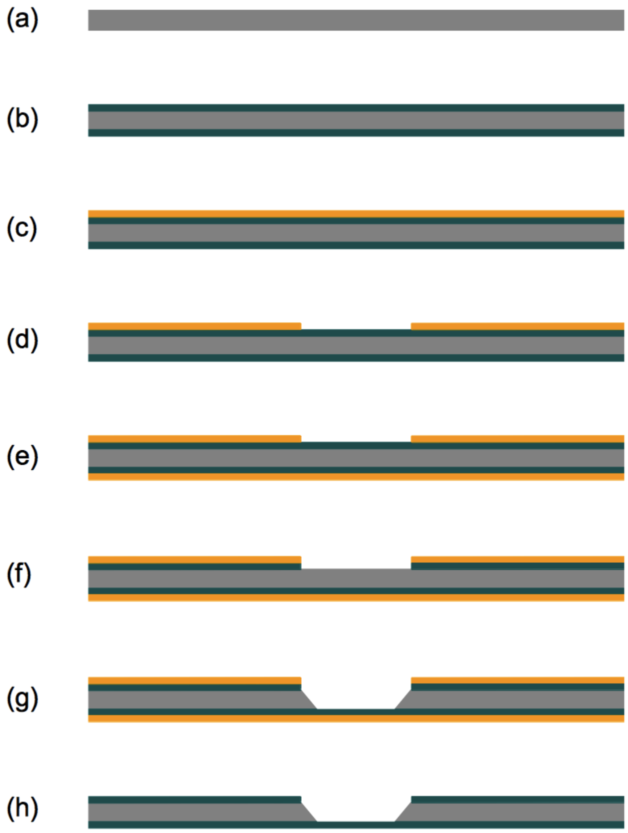

Figure 5.10: Process flow to fabricate a free standing silicon nitride membrane. (a) Ultra clean Si wafers must be used with no organic contaminants. Piranha clean can be utilized to remove organics from the wafer. (b) Silicon nitride is deposited on both sides of the wafer using a plasma enhanced chemical vapor deposition system. The film is about 400 nm thick and the residual stress must be a minimum to fabricate freestanding membranes. (c) E-beam deposition of Au. An adhesion layer of 20 nm Cr followed by 50 nm Au was applied. (d) Pattern the Au layer to expose the underlying silicon nitride layer. (e) Deposit Au on the other side of the wafer as a protectant (f) Etch the silicon nitride layer using Reaction Ion Etching to expose the bare Si wafer. (g) Etch the Si wafer anisotropically using hot KOH till a freestanding silicon nitride membrane is obtained. (h) Remove the protective Au and Cr layers with corresponding chemical etchants.

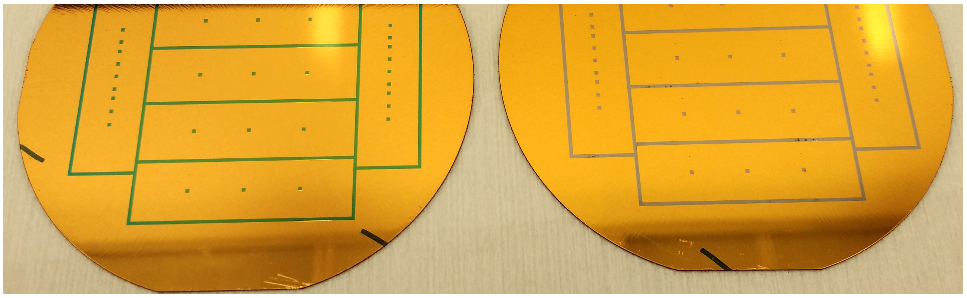

Figure 5.11: Etching of silicon nitride with Reactive Ion Etching (RIE). The patterned wafer on the left shows the appearance after removing the gold selectively. This is the process shown in Fig. 5.10 (d) The exposed silicon nitride is green in color. The wafer on the right shows a similar wafer to that on left, but after etching the silicon nitride layer with RIE. This exposes the underlying silicon wafer (similar to the process shown in Fig. 5.10 (f))

the Au layer and the exposed metal were etched with gold etchant (Sigma) and CR7 chrome etchant. Following the metal etching process, the other side of the wafer was deposited with Cr and Au to protect during the KOH etch.

Next, the exposed area of silicon nitride (from the metal etching step) was etched with reactive ion etching (Fig. 5.10 (f)). Etching of the silicon nitride was achieved with a gas mixture of O_2 and CF_4 with O_2:CF_4 being 5:1 and with a total pressure of 200 mTorr [77]. Fig. 5.11 shows an image of the patterned silicon wafer. The wafer on the left shows the exposed silicon nitride (green in color) after etching away the gold while the wafer on the right shows the exposed bare silicon after etching of the silicon nitride layer.

After etching away the exposed silicon nitride, the exposed silicon was etched in hot KOH (20 grams KOH in 100 mL water) to form the freestanding silicon nitride membrane. Finally, the Au and Cr protective coatings were removed via corresponding etchants. Fig 5.12 shows an image of the free standing silicon nitride membrane. The green area is the silicon nitride layer on the silicon wafer while the square in the middle is the freestanding membrane. The membrane in

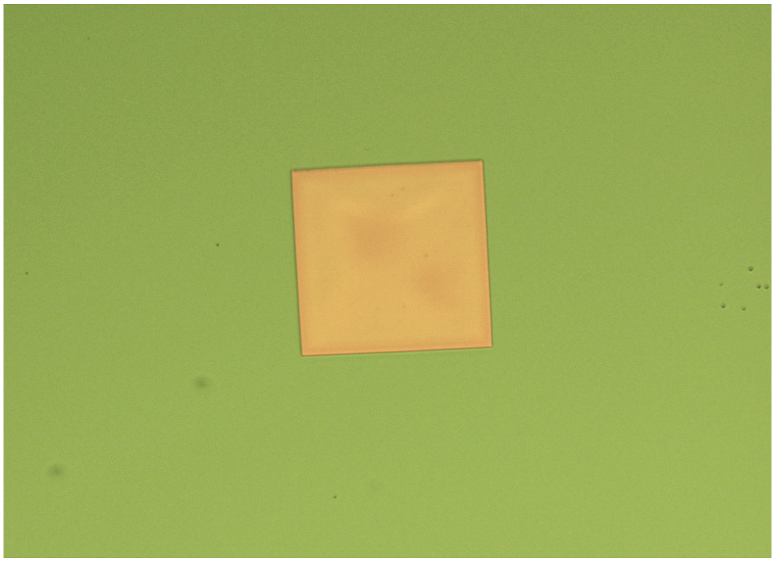

Figure 5.12: Silicon chip containing the free standing membrane. The green area is the silicon nitride layer on the Si wafer while the square in the center is the freestanding silicon nitride membrane. The membrane is about 90 μm × 90 μm and 400 nm thick. Image was acquired with a microscope using the light reflected off the surface.

the image is about 90 μm (side of the square) and about 400 nm thick.

The next step in the fabrication is to etch apertures in the freestanding silicon nitride membrane. The apertures were fabricated by UV photolithographic patterning followed by reactive ion etching of silicon nitride. A thin ($\sim 1\mu$m) layer of photoresist (AZ 5215 IR) was used to pattern the apertures on the silicon nitride membrane. After developing the photoresist, exposed area of the silicon nitride was etched to form the holes in the membrane. Reactive ion etching was used to etch the silicon nitride membrane with the conditions described earlier.

Fig. 5.13 shows a silicon nitride membrane after etching a hole in the middle. The image was taken with reflected light, and the aperture was ~ 25 μm.

Fig. 5.14 shows an array of 10 μm holes fabricated on the free standing silicon nitride membrane. The image was taken with an SEM. It is experimentally known

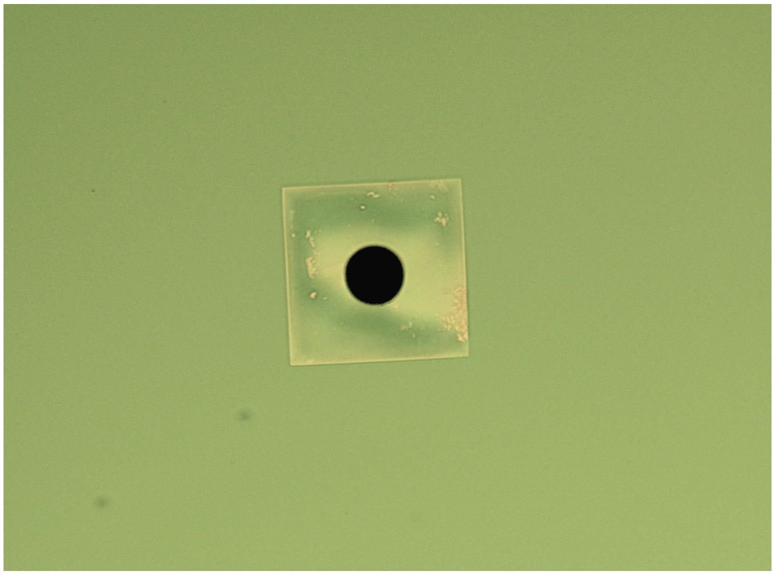

Figure 5.13: Silicon chip containing the free standing membrane with a $\sim 25\ \mu$m aperture. The aperture was fabricated with photolithographic patterning followed by reactive ion etching.

that small lipid bilayers are more stable than large bilayers. Thus, producing an array of small apertures is of interest to realize an artificial axon that is robust.

Fig. 5.15 shows the back side of two silicon chips with free standing membranes (the membranes are facing down). The upper chip has three membranes which are separated by about ~ 1 cm while the lower chip has 9 freestanding membranes which are separated by ~ 2.5 mm. Each silicon nitride membrane has an aperture fabricated to support a bilayer and all of these sites will be connected with a single fluid channel.

5.3.2 Fabrication of electrodes

After fabricating the freestanding silicon nitride membrane with the apertures, the working electrodes must be deposited on the device. The patterning of the electrodes is done via a liftoff technique [78] which is illustrated in figure 5.16. First, photoresist (AZ5214 IR) was patterned on the device as shown in Fig. 5.16

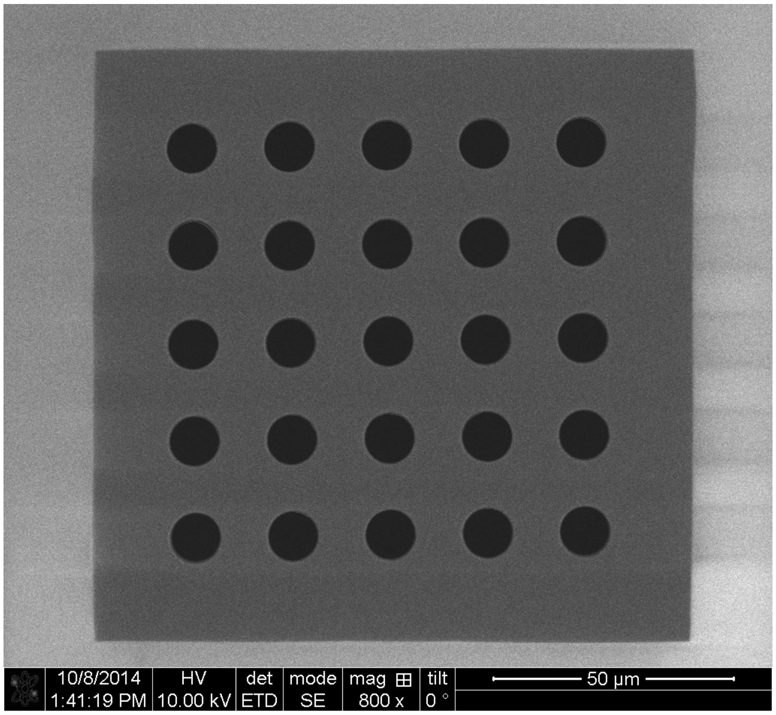
10/8/2014
1:41:19 PM
HV
10.00 kV
det
ETD
mode
SE
mag ⊞
800 x
tilt
0 °
50 μm

Figure 5.14: A free standing silicon nitride membrane with an array of 10 μm holes. Separation between the holes is 10 μm. The image was acquired with an SEM by focusing the e-beam on the top surface of a chip.

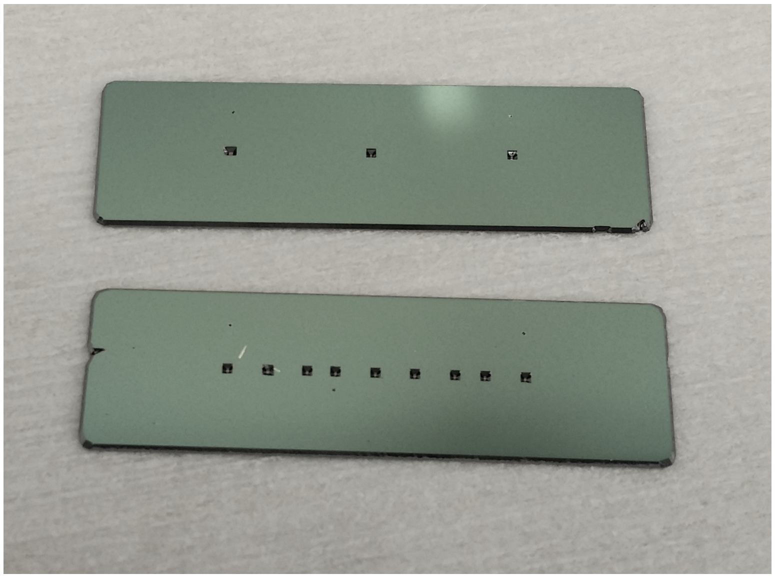

Figure 5.15: Back side of a silicon chip containing the free standing membrane. The small square pits correspond to the locations where the KOH etched the Si wafer till it met the silicon nitride membrane on the other side of the wafer.

(a) and (b). The thickness of the photoresist film was $\sim 1\ \mu$m and the photoresist must be processed in the image reversal mode to obtain negative sidewalls. After the patterning of the photoresist, metals were deposited on the devise with an e-beam deposition system (Cr followed by Au, Au thickness is 50 nm). The final step is to liftoff the photoresist along with the metal deposited on the photoresist by using acetone. The final device after Au electrode fabrication is shown in Fig. 5.16 (d).

The electrodes were patterned in two steps; the first step was to pattern the electrode as well as the connection to the outside via Au pads. In the next step, Ag was deposited on the gold electrode to cover the region exposed to the buffer (500 nm thick Ag) to form the working Ag/AgCl electrode. Fig. 5.17 shows an image of a fabricated electrode taken with reflected light under a microscope. A 500 nm thick Ag electrode is on top of an Au pad that provides electrical access. The silver electrode has dimensions of $200\ \mu\text{m} \times 100\ \mu\text{m} \times 500$ nm (L × W ×

H) while the aperture is of diameter $\sim 60\ \mu$m.

Fig. 5.18 shows the top side of two chips with free standing silicon nitride membranes with integrated electrodes. A free standing silicon nitride membrane with an aperture is present in proximity to each electrode (similar to figure 5.17).

5.3.3 Making PDMS support layers

The silicon chip containing the freestanding silicon nitride membrane with the micron scale apertures and electrodes must be bonded to form fluid compartments. These fluid compartments will serve as intracellular and extracellular buffer chambers. The most suitable material to form these buffer chambers is the elastomer Polydimethylsiloxane (PDMS). PDMS has been widely used in research for many applications in microfluidics [79]. The material can be casted on a mold and a negative imprint of the mold can be transferred to PDMS. This is the basic technique to produce microfluidic channels. PDMS is a clear material with excellent biocompatibility. It can be bonded to materials such as silicon, silicon nitride after a short oxygen plasma treatment procedure and this bond forms a tight seal [80].

The first step is to produce the mold wafer and this is achieved by patterning photoresist on a silicon wafer. Fluid channels of the extracellular side must of low resistance compared to the intracellular fluid chamber. This is due to the fact that the interior of an axon is much smaller when compared with the buffer outside the neuron. Therefore the fluid channels of the PDMS layer corresponding to the extracellular side must be more deeper than the fluid channels in the PDMS layer corresponding to the intracellular side. The photoresist mold for deeper channels was fabricated with the photoresist SU8 2100 whereas the mold corresponding to shallow channels were fabricated with the photoresist AZ 4620.

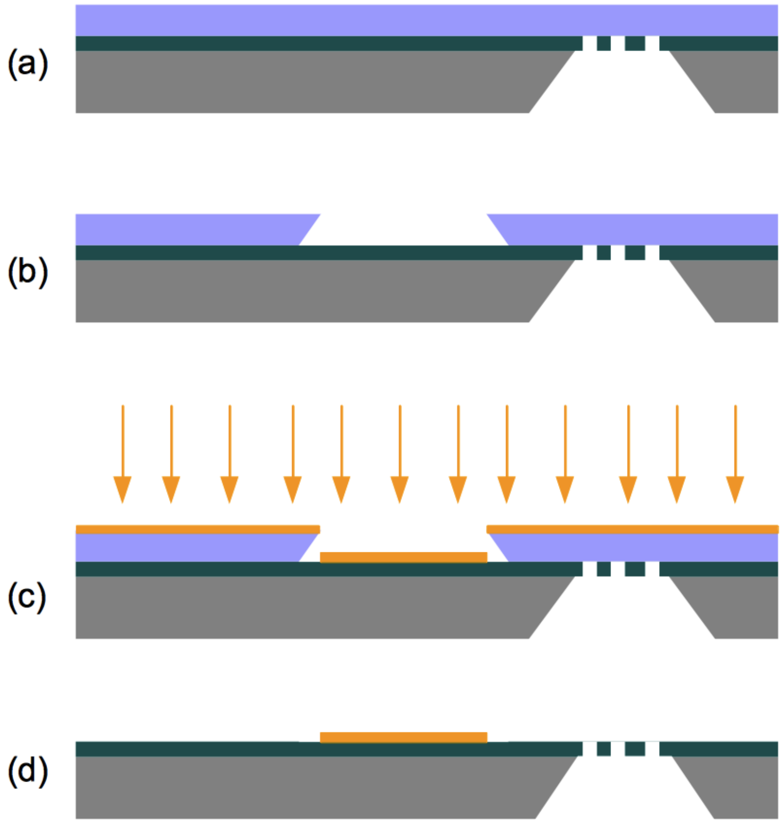

Figure 5.16: The liftoff process for the fabrication of electrodes on the silicon nitride membrane. This process is done after fabricating freestanding silicon nitride membrane with the apertures. (a) The silicon chip with the silicon nitride membrane is coated with a thin layer of photoresist AZ5214 IR. (b) An aligner is used to position the electrode pattern at the appropriate position relative to the apertures and the photoresist is patterned according to manufacturers guidelines (c) Metal deposition using an e-beam evaporator (d) a brief acetone dip dissolves the photoresist leaving only the metal directly deposited on the silicon chip.

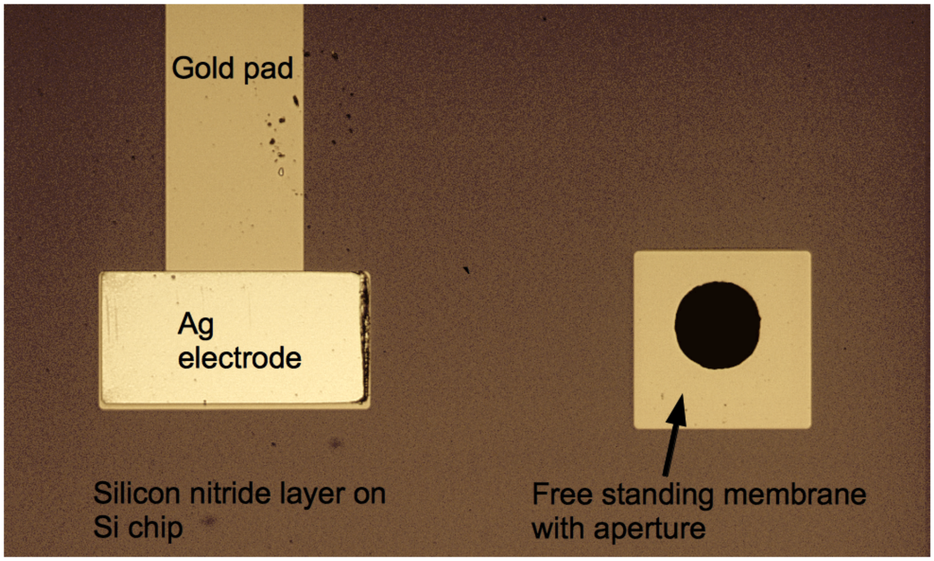
Gold pad
Ag
electrode
Silicon nitride layer on
Si chip
Free standing membrane
with aperture

Figure 5.17: Image of an electrode fabricated adjacent to a free standing silicon nitride membrane with an aperture. The gold pad connects the Ag electrode to the outside instrumentation. The gold pas was fabricated first using the liftoff technique described here. 20 nm of Cr followed by 50 nm of Au was deposited to produce the gold pad. A separate liftoff process was performed to fabricate the Ag electrode on the gold pad. The thickness of the silver electrode is 500 nm.

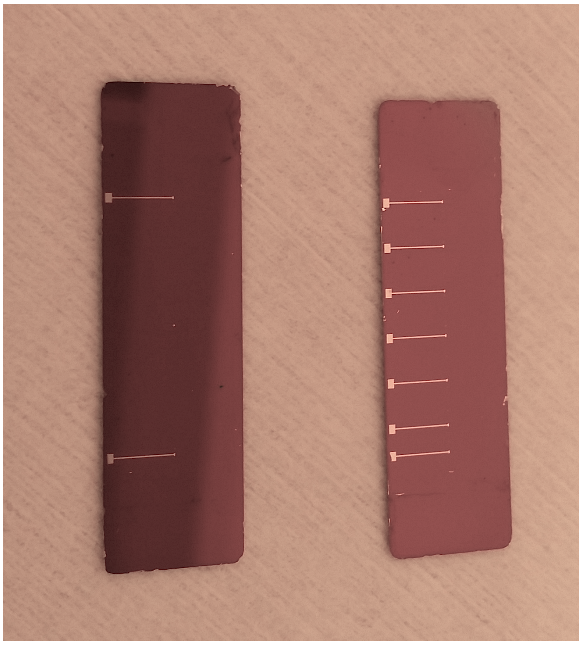

Figure 5.18: Silicon chips patterned with electrodes. A free standing membrane with an aperture exists next to each end of an electrode as shown in Fig. 5.17. The multi electrode Si chip on the right can also be used to record the voltage along the channel.

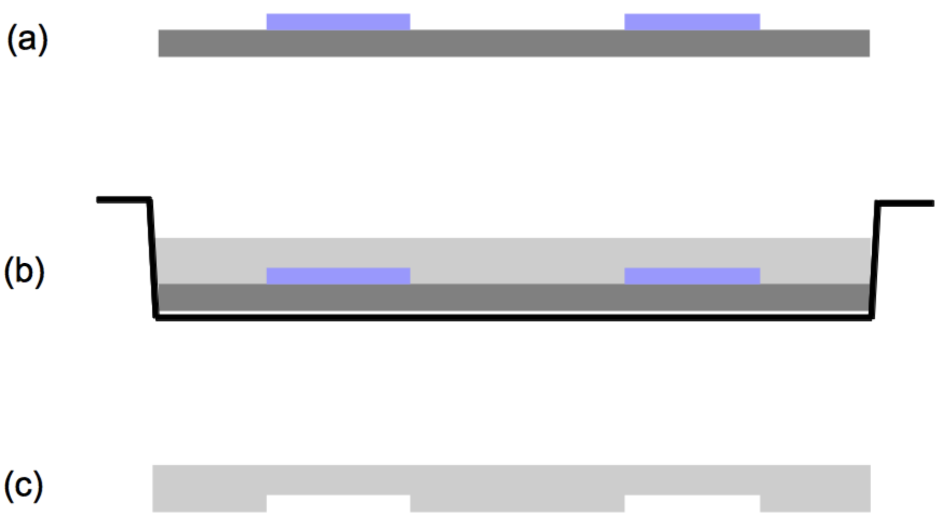

Figure 5.19: Fabrication of the PDMS fluid channels. (a) The initial step is to produce the mold on a Si wafer. The Si wafer must undergo a passivation with Sigmacote before applying PDMS. (b) The mold was fixed to the bottom of a petri dish and PDMS solution was poured on to the mold. PDMS was baked in a 65 °C oven after degassing to remove air bubbles. (c) Peel off the PDMS layer from the wafer.

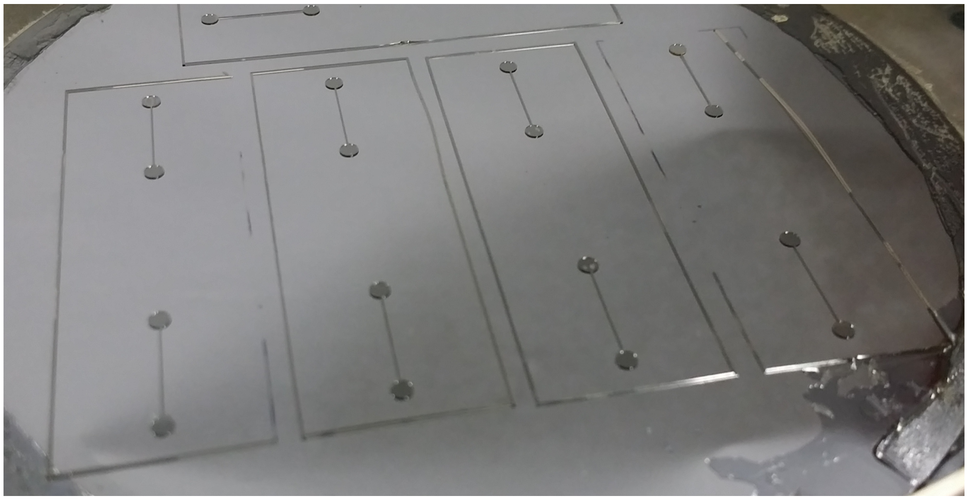

Figure 5.20: An image of a PDMS mold created by pattering photoresist on a silicon wafer. The mold shown in the image corresponds to the bottom PDMS layer. 100 μm thick SU-8 2100 photoresist was used for patterning the mold.

Fig. 5.19 (a) shows the mold fabricated with photoresist on a silicon wafer. Before casting the PDMS on the mold, the surface of the silicon wafer must undergo a passivation step with a hydrophobic coating. The reason behind the passivation is to ease the separation of the mold wafer and the PDMS cast. The surface passivation is achieved by applying Sigmacote (Sigma Aldrich) on the mold wafer for a few minutes. Fig. 5.20 shows a close-up image of the mold wafer used for fabrication of the bottom PDMS layer. The photoresist tracks which defined fluid channels were around 100 μm, producing 100 μm deep fluid channels in PDMS.

The next step is to mix the polymerization initiator with PDMS and pour the PDMS on the mold wafer (Fig. 5.19 (b)). After degassing to remove any air bubbles, the PDMS was left in a 65 °C oven overnight to harden the elastomer. The final step is to peel off of the PDMS layer from the mold wafer, wash the PDMS piece with acetone and store it in a dust free environment.

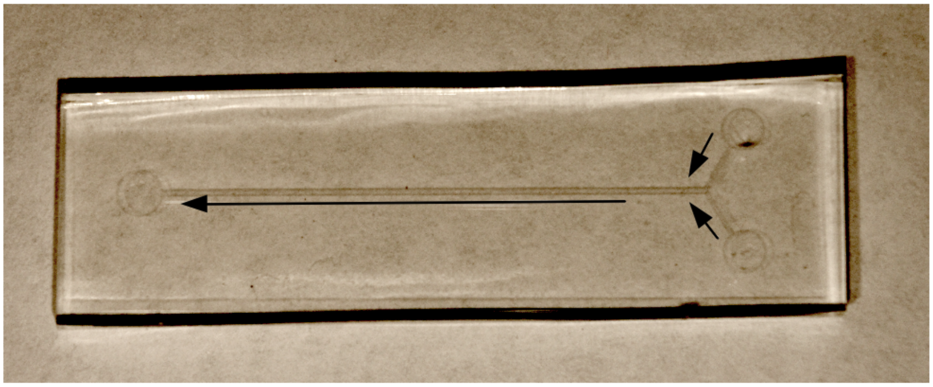

Figure 5.21: The top PDMS layer with the fluid channels. The arrows indicate the intended direction of flow of buffer. The channel is 10 μm deep and the two circular inlet ports on the right side was designed to aid in pumping two different fluids.

5.3.4 Bonding the device

The top and bottom PDMS layers must be bonded to the silicon chip with the free standing membrane and the bottom PDMS layer must be bonded to a glass slide (as shown in Fig. 5.9). The bonding is achieved by plasma treatment of PDMS. The plasma used here is oxygen plasma and the exact duration of treatment is instrument dependent. In this work, we used the Technics RIE tool at the UCLA NRF, which was used with an O_2 pressure of 500 mTorr with an RF power of 80 W. Under these conditions, a 30 second exposure was required for successful bonding of PDMS to glass or silicon.

Fig. 5.22 shows an image of the top PDMS layer bonded to a glass slide for testing. A dye was sent from the fluid port on the right side, which went through the channel and came out from the ports on the left. Fig 5.23 shows the final assembled device. Buffer can be independently exchanged in the top fluid chamber and the bottom fluid chamber.

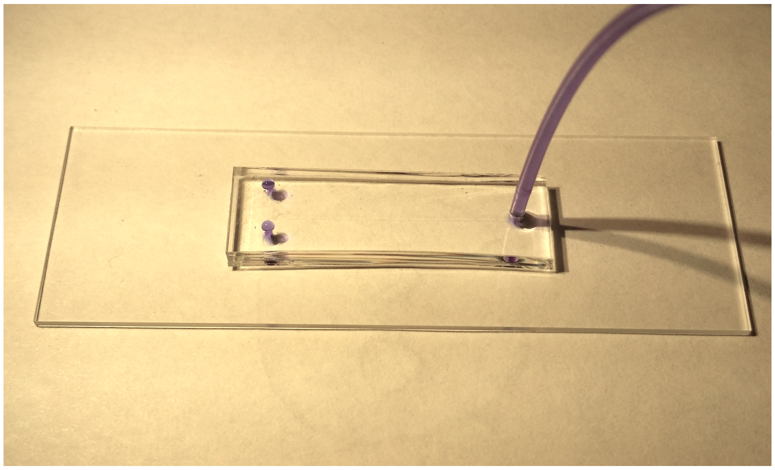

Figure 5.22: PDMS microfluidic layer bonded on to a glass slide. This device was fabricated for testing the fluid flow in a 10 μm deep fluid channels. The tube pumps colored water from the left inlet and the solution comes out from the other side.

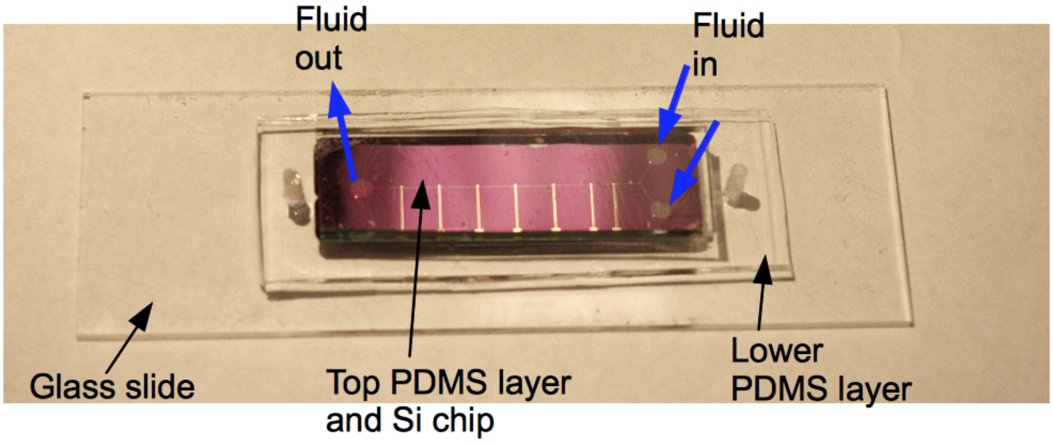
Fluid
out
Fluid
in
Glass slide
Top PDMS layer
and Si chip
Lower
PDMS layer

Figure 5.23: An assembled axon device. The image shows a multi well axon device where a 60 μm aperture is present next to each electrode. A straight fluid channel of 10 μm height and 100 μm wide runs across the apertures from the topside and a 100 μm deep channel runs underneath the apertures.

5.3.5 Future work

In my work, I designed and fabricated the platform to form the artificial axon. However, there are still technical challenges that must be addressed before studying signal propagation. The first and foremost challenge is to form lipid bilayers across the aperture. There were previous experiments where lipid bilayers were formed in microfluidic channels by passing droplets [81] and the same technique can be adapted here. Another technique is to fuse giant vesicles on the aperture. Giant vesicles can be produced with a size of around $\sim 10\ \mu$m and these can be fused on apertures with a smaller diameter to form a seal. The technique is advantageous since giant vesicles have been produced with ion channels incorporated [82].

The stability of these artificial membranes might be a concern, especially when exchanging buffer with different concentrations. One possible remedy for this problem is to grow a protein skeleton on the lipid bilayer. For example, the S layer protein of certain bacterial species form well ordered structures on artificial lipid bilayers increasing their stability [83, 84, 85]. On the other hand, instead of using artificial lipid bilayers, one can fuse a cell or a cell body fragment containing the required ion channels on an aperture to form a seal. A pressure difference can plug an aperture with a cell (or with a fragment of cell wall) forming a giga ohm seal. The use of naturally existing cell scaffolds has the advantage of stability. For example, these cell bodies must be stable than synthetic lipid membranes for osmotic stresses up to a certain degree (due to the cytoskeleton, peptidoglycans).

REFERENCES

[1] Alan E. Senior, Sashi Nadanaciva and Joachim Weber, The molecular mechanism of ATP synthesis by F_1F_0-ATP synthase. *Biochimica et Biophysica Acta (BBA) Bioenergetics*, 1553(3):188-211, 2002.

[2] Arne Gennerich and Ronald D Vale, Walking the walk: how kinesin and dynein coordinate their steps. *Current Opinion in Cell Biology*, 21(1):59-67, 2009.

[3] K. Ravi Acharya and Matthew D. Lloyd, The advantages and limitations of protein crystal structures. *Trends in Pharmacological Sciences*, 26(1):10-14, 2005.

[4] Thomas E Fisher, Andres F. Oberhauser, Mariano Carrion-Vazquez, Piotr E. Marszalek, Julio M. Fernandez, The study of protein mechanics with the atomic force microscope. *Trends in Biochemical Sciences*, 24(10):379384, 1999.

[5] Moritz Mickler, Ruxandra I. Dima, Hendrik Dietz, Changbong Hyeon, D. Thirumalai, and Matthias Rief, Revealing the bifurcation in the unfolding pathways of GFP by using single-molecule experiments and simulations. *Proceedings of the National Academy of Sciences*, 104(51):2026820273, 2007.

[6] Keir C. Neuman and Attila Nagy, Single-molecule force spectroscopy: optical tweezers, magnetic tweezers and atomic force microscopy. *Nature Methods*, 5(6):491-505, 2008.

[7] A. Ashkin, Acceleration and trapping of particles by radiation pressure. *Physical Review Letters*, 24(4):156, 1970.

[8] A. Ashkin and J. M. Dziedzic, Optical trapping and manipulation of viruses and bacteria. *Science*, 235(4795):1517-1520, 1987.

[9] S. Forth, M.Y. Sheinin, J. Inman, and M.D. Wang, Torque measurement at the single-molecule level. *Annual Review of Biophysics*, 42:583-604, 2013.

[10] Piston D. W. and G. J. Kremers, Fluorescent protein FRET: the good, the bad and the ugly. *Trends in Biochemical Sciences*, 32(9):407-414, 2007.

[11] Kajihara D., Abe R., Iijima I., Komiyama C., Sisido M. and T. Hohsaka, FRET analysis of protein conformational change through position-specific incorporation of fluorescent amino acids. *Nature Methods*, 3(11):923-929, 2006.

[12] Choudhary, S. Sloan, S. Fok, A. Neckar, E. Trautmann, P. Gao, T. Stewart, C. Eliasmith, and K. Boahen, Silicon Neurons that Compute. *International Conference on Artificial Neural Networks, LNCS*, 7552:121-128, 2012.

[13] Emre Neftci, Elisabetta Chicca, Giacomo Indiveri, Rodney Douglas. A Systematic Method for Configuring VLSI Networks of Spiking Neurons. *Neural Computation*, 23(10):2457-2497, 2011.

[14] Youxing Jiang, Alice Lee, Jiayun Chen, Vanessa Ruta, Martine Cadene, Brian T. Chait and Roderick MacKinnon, X-ray structure of a voltage-dependent K^+ channel. *Nature*, 423:33-41, 2003.

[15] Vanessa Ruta, Youxing Jiang, Alice Lee, Jiayun Chen and Roderick MacKinnon, Functional analysis of an archaebacterial voltage-dependent K^+ channel. *Nature*, 422:180-185, 2003.

[16] Heginbotham L, LeMasurier M, Kolmakova-Partensky L and C. Miller, Single Streptomyces lividans k^+ channels. *The Journal of General Physiology*, 114:551-560, 1999.

[17] M. LeMasurier, L. Heginbotham and C. Miller KcsA: its a potassium channel. *The Journal of General Physiology*, 118:303-313, 2001.

[18] Zhou, Y., J. H. Morais-Cabral, A. Kaufman, and R. MacKinnon Chemistry of ion coordination and hydration revealed by a K^+ channel Fab complex at 2.0 Å resolution. *Nature*, 414:43-48, 2001.

[19] J. Aqvist, Ion-water interaction potentials derived from free energy perturbation simulations. *The Journal of Physical Chemistry*, 94:8021-8024, 1990.

[20] Prasanna K. Devaraneni, Alexander G. Komarov, Corey A. Costantino, Jordan J. Devereaux, Kimberly Matulef, and Francis I. Valiyaveetil, Semisynthetic K^+ channels show that the constricted conformation of the selectivity filter is not the C-type inactivated state *Proceedings of the National Academy of Sciences*, 110(39):15698-15703, 2013.

[21] Hongxia Bao, Atiya Hakeem, Mark Henteleff, John G. Starkus, and Martin D. Rayner, Voltage-insensitive Gating after Charge-neutralizing Mutations in the S4 Segment of Shaker Channels. *The Journal of General Physiology*, 113(1):139-151, 1999.

[22] Youxing Jiang, Vanessa Ruta, Jiayun Chen, Alice Lee and Roderick MacKinnon, The principle of gating charge movement in a voltage-dependent K^+ channel. *Nature*, 423:42-48, 2003.

[23] Francisco Bezanilla, Voltage-Gated Ion Channels. *IEEE TRANSACTIONS ON NANOBIOSCIENCE*, 4(1):34-48, 2005.

[24] Baron Chanda, Osei Kwame Asamoah, Rikard Blunck, Benoit Roux and Francisco Bezanilla, Gating charge displacement in voltage-gated ion channels involves limited transmembrane movement. *Nature*, 436:852-856, 2005.

[25] David J. Posson, Pinghua Ge, Christopher Miller, Francisco Bezanilla and Paul R. Selvin, Small vertical movement of a K^+ channel voltage sensor measured with luminescence energy transfer. *Nature*, 436:848-851, 2005.

[26] Ruta V., Chen J., R. MacKinnon, Calibrated measurement of gating-charge arginine displacement in the KvAP voltage-dependent K^+ channel. *Cell*, 123(3):463-475, 2005.

[27] Long, S. B., E. B. Campbell, and R. MacKinnon, Voltage sensor of Kv1.2: Structural basis of electromechanical coupling. *Science*, 309:903-908, 2005.

[28] Yarov-Yarovoy, V., D. Baker, and W. A. Catterall, Voltage sensor conformations in the open and closed states in rosetta structural models of K^+ channels. *Proceedings of the National Academy of Sciences* , 103:7292-7297, 2006.

[29] Pathak, M. M., V. Yarov-Yarovoy, G. Agarwal, B. Roux, P. Barth, S. Kohout, F. Tombola, and E. Y. Isaco, Closing in on the resting state of the Shaker K^+ channel. *Neuron*, 56:124-140, 2007.

[30] J. Porath, Immobilized metal ion affinity chromatography. *Protein Expression and Purification*, 3:263-281, 1992.

[31] P. Hengen, Purification of his-tag fusion proteins from *Escherichia coli.*, *Trends in Biochemical Sciences*, 20:285-286, 1995.

[32] Wonderlin W., Finkel A. and R. French, Optimizing planar lipid bilayer single-channel recordings for high resolution with rapid voltage steps., *Biophysical Journal*, 58:289-297, 1990.

[33] John David Jackson, Classical Electrodynamics, 3rd edition, *John Wiley and Sons, Inc.* 1998.

[34] Hible G., Christova P., Renault L., Seclaman E., Thompson A., Girard E., Munier-Lehmann H. and J. Cherfils, Unique GMP-binding site in Mycobacterium tuberculosis guanosine monophosphate kinase, *Proteins*, 62(2):489-500, 2006.

[35] Y. Wang and G. Zocchi, Elasticity of globular proteins measured from the AC susceptibility. *Physical Review Letters*, 105:238104, 2010.

[36] Y. Wang and G. Zocchi, The folded protein as a visco-elastic solid. *Europhysics Letters*, 96:18003, 2011.

[37] Y. Wang and G. Zocchi, Viscoelastic transition and yield strain of the folded protein. *PLoS ONE*, 6(12):e28097, 2011.

[38] Hao Qu, Jonathan Landy and Giovanni Zocchi, Cracking phase diagram for the dynamics of an enzyme. *Physical Review E*, 86:041915, 2012.

[39] Chiao-Yu Tseng, Andrew Wang, Giovanni Zocchi, Biljana Rolih and Alex J. Levine, Elastic energy of protein-DNA chimeras. *Physical Review E*, 80:061912, 2009.

[40] R. M. Daniel, M. Dines and H. H. Petach, The denaturation and degradation of stable enzymes at high temperatures. *Biochemical Journal*, 317:1-11, 1996.

[41] P. L. Privalov, Cold denaturation of proteins. *Critical Reviews in Biochemistry and Molecular Biology*, 25(4):281-305, 1990.

[42] Statistical mechanics of warm and cold unfolding in proteins. *The European Physical Journal B*, 6:157, 1998.

[43] A. Hansen, M. Jensen, K. Sneppen and G. Zocchi, Hot and cold denaturation of proteins: critical aspects. *The European Physical Journal B*, 10:193, 1999.

[44] A. Hansen, M. Jensen, K. Sneppen and G. Zocchi A model for the thermodynamics of globular proteins. *Physica A*, 25(4):281-305, 1990.

[45] Schlierf, M. and M. Rief, Temperature softening of a protein in single-molecule experiments. *Journal of Molecular Biology*, 354:497-503, 2005.

[46] M. Menzinger and R. Wolfgang, The Meaning and Use of the Arrhenius Activation Energy. *Angewandte Chemie*, 8(6):438, 1969.

[47] Luzar, A. and D. Chandler, Structure and hydrogen bond dynamics of water-dimethyl sulfoxide mixtures by computer simulations. *Journal of Chemical Physics*, 98:8160-8173, 1993.

[48] Daniela Russo, The impact of kosmotropes and chaotropes on bulk and hydration shell water dynamics in a model peptide solution. *Journal of Chemical Physics*, 345:200-211, 2008.

[49] Iosif I. Vaismant and L. Max Berkowitz, Local Structural Order and Molecular Associations in Water-DMSO Mixtures. Molecular Dynamics Study. *Journal of American Chemical Society*, 114:7889-7896, 1992.

[50] Jean-Marc Zanotti, Marie-Claire Bellissent-Funel and Joseph Parello Hydration-Coupled Dynamics in Proteins Studied by Neutron Scattering and NMR: The Case of the Typical EF-Hand Calcium-Binding Parvalbumin. *Biophysical Journal*, 76(5):2390-2411, 1999.

[51] F. Temple Burling, William I. Weis, Kevin M. Flaherty and Axel T. Brünger Direct Observation of Protein Solvation and Discrete Disorder with Experimental Crystallographic Phases. *Science*, 5:72-77, 1996.

[52] Simon Ebbinghaus, Seung Joong Kim, Matthias Heyden, Xin Yu, Udo Heugen, Martin Gruebele, David M. Leitner and Martina Havenith, An extended dynamical hydration shell around proteins. *Proceedings of the National Academy of Sciences*, 104(52):20749-20752, 2007.

[53] Aoife C. Fogarty and Damien Laage, Water Dynamics in Protein Hydration Shells: The Molecular Origins of the Dynamical Perturbation. *The Journal of Physical Chemistry*, 118:7715-7729, 2014.

[54] T. A. Taton, edited by M. Egli, P. Herdewijn, A. Matsuda, and Y. S. Sangvhi Preparation of Gold Nanoparticle-DNA Conjugates *John Wiley and sons, Inc.,Malden, MA, 2002*, pages 12.2.1-12.2.12.

[55] Cheryl, L. B. and David G. Myszka, Current and emerging commercial optical biosensors, *Journal of Molecular Recognition* 14:261-268, 2001.

[56] Mitsui, Keita and Handa, Yoichiro and Kajikawa, Kotaro *Optical fiber affinity biosensor based on localized surface plasmon resonance* (Appl. Phys. Lett.) volume 85, pages 4231-4233, 2004.

[57] Naik, A.K and Hanay, M.S. and Hiebert, W. K. and Feng, X. L. and Roukes, M.L. *Towards single-molecule nanomechanical mass spectrometry* (Towards single-molecule nanomechanical mass spectrometry) volume 4, pages 445-450, 2009.

[58] Ekinci, K. L. and Huang, X. M. H. and Roukes, M.L. *Ultrasensitive nanoelectromechanical mass detection* (Ultrasensitive nanoelectromechanical mass detection) volume 84, pages 4469-4471, 2004.

[59] Hema Chandra Kotamarthi, Anju Yadav, Sri Rama Koti Ainavarapu. Small Peptide Binding Stiffens the Ubiquitin-like Protein SUMO1.*Biophysical Journal*, 108(2):360-367,2015.

[60] Xiaotang Hu and Hongbin Li. Force spectroscopy studies on protein-ligand interactions: a single protein mechanics perspective.*FEBS Letter*, 588:3613-3620,2014.

[61] Sri Rama Koti Ainavarapu, Lewyn Li, Carmen L. Badilla, Julio M. Fernandez. Ligand binding modulates the mechanical stability of dihydrofolate reductase.*Biophysical Journal*, 89(5):3337-3344,2005.

[62] Kretschmann, E. and Reather, H. Radiative decay of nonradiative surface plasmon excited by light. *Z. Naturf.*, 23a:2135-2136, 1968.

[63] A. Otto, Exitation of nonradiative surface plasma waves in silver by the method of frustrated total reflection. *Z. Naturf.*, 241:313-324, 1971.

[64] Olivier Delalande, Sophie Sacquin-Mora and Marc Baaden. Enzyme Closure and Nucleotide Binding Structurally Lock Guanylate Kinase.*Biophysical Journal*, 101(6):1440-1449,2011.

[65] Yue Li, Yanling Zhang and Honggao Yan. Kinetic and Thermodynamic Characterizations of Yeast Guanylate Kinase.*The Journal of Biological Chemistry*, 271(45):28038-28044,1996.

[66] J T. Vivian and P. R. Callis. Mechanisms of tryptophan fluorescence shifts in proteins.*Biophysical Journal*, 80(5):2093-2109,2001.

[67] Hongguang Sun, Xun Zhu, Patrick Y Lu, Roberto R Rosato, Wen Tan and Youli Zu. Oligonucleotide Aptamers: New Tools for Targeted Cancer Therapy.*Molecular Therapy Nucleic Acids*, 3:e182,2014.

[68] Jennifer F. Lee, Jay R. Hesselberth, Lauren Ancel Meyers and Andrew D. Ellington. Aptamer Database.*Nucleic Acids Research*, 32(Database issue):D95-D100,2004.

[69] Tai-Chia Chiu and Chih-Ching Huang. Aptamer-Functionalized Nano-Biosensors.*Sensors*, 9:10356-10388,2009.

[70] Ryuji Kawano, Toshihisa Osaki, Hirotaka Sasaki, Masahiro Takinoue, Satoko Yoshizawa, and Shoji Takeuchi. Rapid Detection of a Cocaine-Binding Aptamer Using Biological Nanopores on a Chip.*The Journal of the Americal Chemical Society*, 133:8474-8477,2011.

[71] James S. Swensen, Yi Xiao, Brian S. Ferguson, Arica A. Lubin, Rebecca Y. Lai, Alan J. Heeger, Kevin W. Plaxco and H. Tom. Soh. Continuous, Real-Time Monitoring of Cocaine in Undiluted Blood Serum via a Microfluidic, Electrochemical Aptamer-Based Sensor.*The Journal of the Americal Chemical Society*, 131:4262-4266,2009.

[72] Milan N. Stojanovic and Donald W. Landry. Aptamer-Based Colorimetric Probe for Cocaine.*The Journal of the Americal Chemical Society*, 124:9678-9679,2002.

[73] Philip Nelson Biological Physics.*W. H. Freeman and Company*, 2004.

[74] A. L. Hodgkin and A. F. Huxley. A quantitative description of membrane current and its application to conduction and excitation in nerve.*The Journal of Physiology*, 117(4):500-544,1952.

[75] Hai Ni, Hoo-Jeong Lee, Ainissa G. Ramirez. A robust two-step etching process for large-scale microfabricated SiO_2 and Si_3N_4 MEMS membranes.*Sensors and Actuators A*, 119:553-558,2005.

[76] H. Seidel, L. Csepregi, A. Heuberger and H. Baumgärtel. Anisotropic etching of crystalline silicon in alkaline solutions.*Journal of The Electrochemical Society*, 13(11):3612-3626,1990.

[77] B. E. E. Kastenmeier, P. J. Matsuo, J. J. Beulens and G. S. Oehrlein.Chemical dry etching of silicon nitride and silicon dioxide using $CF_4/O_2/N_2$ gas mixtures.*Journal of Vacuum Science and Technology A*, 14(5):2802-2813,1996.

[78] Park B.Y., Zaouk R. and Madou M.J.. Fabrication of microelectrodes using the lift-off technique. *Methods in Molecular Biology*, 321:23-26,2006.

[79] Samuel K. Sia and George M. Whitesides. Microfluidic devices fabricated in poly(dimethylsiloxane) for biological studies. *Electrophoresis*, 24:3563-3576,2003.

[80] Say Hwa Tan, Nam-Trung Nguyen, Yong Chin Chua and Tae Goo Kang. Oxygen plasma treatment for reducing hydrophobicity of a sealed polydimethylsiloxane microchannel. *Biomicrofluidics*, 4(3):032204,2010.

[81] Joon S. Shim, Jia Geng, Chong H. Ahn and Peixuan Guo. Formation of lipid bilayers inside microfluidic channel array for monitoring membrane−embedded nanopores of phi29 DNA packaging nanomotor. *Biomedical Microdevices*, 14(5):921−928,2012.

[82] Sophie Aimon, John Manzi, Daniel Schmidt, Jose Antonio Poveda Larrosa, Patricia Bassereau and Gilman E. S. Toombes. Functional Reconstitution of a Voltage-Gated Potassium Channel in Giant Unilamellar Vesicles. *PLoS ONE*, 6(10):e25529,2011.

[83] Bernhard Schuster, Uwe B. Sleytr, Anke Diederich Günther Bähr and Mathias Winterhalter. Probing the stability of S-layer-supported planar lipid membranes. *European Biophysics Journal*, 28:583-590,1999.

[84] Dietmar Pum, Jose Luis Toca-Herrera and Uwe B. Sleytr.S-Layer Protein Self-Assembly. *International Journal of Molecular Sciences*, 14:2484-2501,2013.

[85] Bernhard Schuster, Dietmar Pum and Uwe B. Sleytr. S-layer stabilized lipid membranes (Review). *Biointerphases*, 3(2),2008.